Design, modelling and control of a brachiating power line inspection robot

Javaad Patel

Department of Electrical Engineering
University of Cape Town
Rondebosch, Cape Town
South Africa

June 2016

Submitted to the Department of Electrical Engineering at the University of Cape Town in fulfilment of the academic requirements for a Masters of Science degree in Electrical Engineering.

Keywords: Power line inspection; Brachiating robot; Feedback control; Trajectory generation

Declaration

I know the meaning of plagiarism and declare that all the work in the document, save for that which is properly acknowledged, is my own.

Signed by candidate

Signature removed

Javaad Patel

Department of Electrical Engineering
University of Cape Town

Friday 3 June, 2016

Abstract

Design, modelling and control of a brachiating power line inspection robot

Javaad Patel

The inspection of power lines and associated hardware is vital to ensuring the reliability of the transmission and distribution network. The repetitive nature of the inspection tasks present a unique opportunity for the introduction of robotic platforms, which offer the ability to perform more systematic and detailed inspection than traditional methods. This lends itself to improved asset management automation, cost-effectiveness and safety for the operating crew.

This dissertation presents the development of a prototype industrial brachiating robot. The robot is mechanically simple and capable of dynamically negotiating obstacles by brachiating. This is an improvement over current robotic platforms, which employ slow, high power static schemes for obstacle negotiation.

Mathematical models of the robot were derived to understand the underlying dynamics of the system. These models were then used in the generation of optimal trajectories, using nonlinear optimisation techniques, for brachiating past line hardware.

A physical robot was designed and manufactured to validate the brachiation manoeuvre. The robot was designed following classic mechanical design principles, with emphasis on functional design and robustness.

System identification was used to capture the plant uncertainty and a feedback controller was designed to track the reference trajectory allowing for energy optimal brachiation swings.

Finally, the robot was tested, starting with sub-system testing and ending with testing of a brachiation manoeuvre proving the prospective viability of the robot in an industrial environment.

Friday 3 June, 2016

Acknowledgements

Firstly, I would like to thank my parents for their unwavering support and belief in me. I am truly grateful for everything you have done for me. Your endless encouragement gave me strength when I needed it most.

To my supervisor, Prof. Edward Boje, your seemingly endless knowledge was a true inspiration for me and the guidance you provided was invaluable. The success of this project would not have been possible without your insight and input. I was truly able to develop and challenge myself during this project and for that, I am forever grateful.

I would like to thank my cousin, Dr Amir Patel, for always taking the time to help. Your comments and ideas always opened up new ways of tackling problems.

To my friend, Arnold. You have taught me more than I can remember and your friendship and the good times we shared have made these some of the best years at university.

To my friend, Callen. Thank you for teaching me all I know about electronics and software. From flashing lights and exploding LED's to proper software design, it has been quite a journey.

I would also like to thank Dr Reuben Govender for lending his expertise and providing insight on the mechanical design of the robot.

To the person who put up with the bulk of my complaining and worries, my girlfriend, Munawwar. Thank you for being so supportive and for always keeping me focused.

Lastly, I would like to thank the National Research Foundation (NRF) and the Eskom Tertiary Education Support Programme (TESP) for providing financial assistance towards this research.

Contents

List of Figures

List of Tables

Abbreviations and symbols

Abbreviations

COM	Centre of Mass
DC	Direct current
EKF	Extended Kalman Filter
emf	Electromotive force
FEA	Finite Element Analysis
IMU	Inertial Measurement Unit
PFL	Partial Feedback Linearisation
RMS	Root Mean Square
SD	Secure Digital

Symbols

a	Acceleration amplitude
a_{req}	Required acceleration
b	Width of gear
d	Displacement
dt	Sampling time
f_c	Coulomb friction
f_v	Viscous friction coefficient
g	Gravity vector
h_v	Vibration damper height
k_m	Motor torque constant
l	Length
l_c	Position of COM of link
l_v	Vibration damper length
m	Mass; Number of constraints
m_{gear}	Gear tooth module
n	Number of rigid bodies
q	State vector
r	Position of COM
$\dot{r}$	Velocity of COM
r_p	Radius of pulley
$r_{effective}$	Effective radius of pulley
s	Laplacian variable
t	Time
u	Control input
x, y	Constraint variables
A	Constraint Matrix

B	Actuation matrix
B_m	Magnetic flux density
C	Coriolis matrix
E	Energy
F_A	Applied force
F_c	Coulomb friction
F_F	Friction force
F_{G_N}, F_{G_P}	Normal and parallel component of gravitational force
F_N	Normal reaction force
F_t	Tangential force
F_x	Horizontal component of orthogonal reaction force
F_y	Vertical component of orthogonal reaction force
G	Gravitational matrix
I	Inertia
$I_{conductor}$	Conductor current
$I_{controller}$	Controller output current
J	Jacobian
K_d, K_p	Controller derivative and proportional gain
L	Lagrangian
M	Mass matrix
N	Gearbox ratio
T	Kinetic energy
V	Potential energy
V_m	Motor Voltage
P	Power
Q	Generalised force vector
R	Motor terminal resistance
Y	Lewis form factor
Z_{gear}	Number of gear teeth
η	Gearbox efficiency
$\theta_1, \theta_2, \theta_3$	Robot angles
θ_p	Pulley angle
λ	Constraint force
μ_0	Permeability
μ_s	Static friction coefficient
σ	Stall torque
σ_a	Allowable bending stress
σ_b	Bending stress
τ	Actuation torque
$\emptyset$	Slope angle
φ	Back-emf constant
ω	Angular velocity
ω_f	Frequency
ω_{th}	Threshold angular velocity

Chapter 1

Introduction

1.1 Research Motivation

The power industry is a critical component of every economy, with electricity demand increasing daily. The ageing assets of power utility companies require regular inspection and maintenance to ensure high reliability. Inspection tasks may include right of way for vegetation encroachment and illegal use, tower faults and, testing of insulators and conductors.

The most common method of inspecting power lines and associated line hardware is by a line inspection crew, as seen in **Figure 1.1**. This method is extremely labour-intensive, prone to oversight due to worker fatigue and reliance on human judgment. Further, direct access to servitudes may be inconvenient or altogether impossible in certain scenarios, such as mountainous regions.

Figure 1.1: Lineman inspecting insulator string at the top of strain tower [1]

An alternative or supplement, is the use of helicopters to perform aerial inspection of power lines, as seen in **Figure 1.2**. This method is faster but significantly more expensive and has limitations such as aircraft availability and distance to the line for inspection.

Figure 1.2: Aerial inspection by helicopter [2]

The introduction of a robot to perform semi-autonomous inspection has a number of advantages such as performing more systematic and detailed inspection, which lends itself to better asset management automation, cost-effectiveness and safety for the operating crew.

However, the operating conditions faced during power line inspection are extremely challenging and very few robotic platforms are capable of operating successfully.

1.2 Analysis of operating environment

1.2.1 Overview of environment

Electricity distribution occurs in a wide variety of environments and therefore an inspection robot will be exposed to extremely varied conditions, as seen in **Figure 1.3**.

Figure 1.3: Electricity distribution through different environments [3, 4]

Environmental factors such as high and low temperatures require a robot to be electrically and mechanically robust. Other environmental factors include, high wind forces and rain which require the robot to have a low drag coefficient and watertight electronics.

1.2.2 Line hardware

Power line inspection is challenging due to the number and variety of line hardware placed along the line which act as obstacles during inspection.

Spacer dampers

Spacer dampers are used to maintain a minimum separation distance between conductors in a bundle to prevent conductors from colliding and causing excess mechanical wear. They come in a variety of forms depending on the number of conductors in a bundle, ranging from two-conductor to six-conductor bundles. A secondary function of spacer dampers is to damp excessive line vibrations due to crosswinds. **Figure 1.4** shows an example of the different types of spacer dampers available.

Figure 1.4: Types of spacer dampers. The image on the left shows a two-bundle spacer damper [5] while the image on the right shows a six-bundle spacer [6].

Vibration dampers

Vibration dampers are usually located near the connection points between the power line and a tower, as seen in **Figure 1.5**. They are designed to dampen the vibration of the lines due to Aeolian vibrations thus preventing excessive mechanical wear of the connections between the line and the tower.

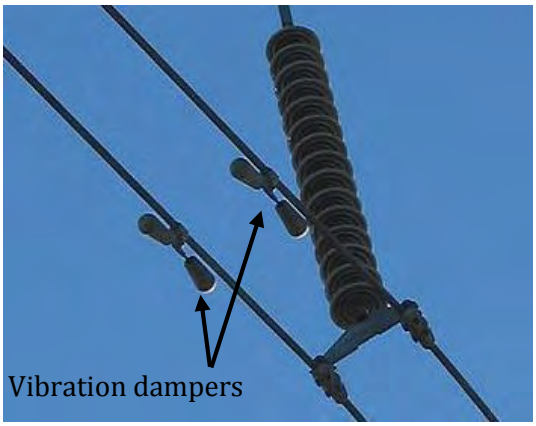

Figure 1.5: Vibration dampers appearing before suspension tower insulator string [7]

Suspension clamp

Suspension clamps are the connection point between insulator strings and the line at suspension towers, as seen in **Figure 1.6**. Their purpose is to support the weight of the line to prevent the line from sagging.

In addition, Corona rings are mounted at the suspension clamps in order to control the electric field at the connection point. Corona is suppressed by surrounding the conductor with a corona ring (at the line potential) to reduce the potential gradient.

Figure 1.6: Suspension clamps connected to insulator strings at suspension tower [8]

Compression dead-ends and jumper cables

Compression dead-ends are fittings at the end of the line which allow for connection of the line to insulator strings, which in turn connect to the tower. They provide a secure fitting which allows the line to be tensioned. An example of a compression dead-end can be seen in **Figure 1.7**.

Figure 1.7: Compression dead-end [9]

Jumper cables, shown in **Figure 1.8**, ensure electrical continuity between spans. They are fitted to compression dead-ends and are not tensioned and therefore more flexible than the main span. The slope at the cables connection points is significantly steeper than the main span and represent an extremely challenging obstacle for a robot. In addition, due to geographical constraints, the conductor path cannot always be straight and therefore the jumper cables often occur out-of-plane.

Figure 1.8: Jumper cable at strain tower showing steep slope

1.2.3 Summary of operating environment

The environmental conditions of line inspection require robust design, however line hardware is the most challenging for robots. The longest obstacle that a robot will have to navigate is a vibration damper, and the widest is a spacer damper. The most difficult obstacles are jumper cables, due to the steep slope and potentially out-of-plane nature.

1.3 Literature review

In order to understand the current state-of-art of power line inspection robotics, an investigation into underactuated robotics and control strategies was conducted. This was followed by an analysis of current power line inspection robotic solutions.

1.3.1 Underactuated robotics

An underactuated robot is one where the number of degrees-of-freedom (DOF) exceeds the number of actuators. This presents an interesting non-linear control problem, since arbitrary accelerations cannot be commanded, and has sparked a number of control solutions.

The most common underactuated robots are based on a double pendulum structure and are designed to achieve a swing up condition. A swing-up manoeuvre, shown in **Figure 1.9**, is one where the two links of the robot are vertical with zero velocity at the end of the manoeuvre.

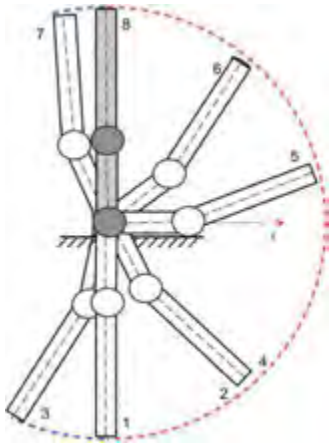

Figure 1.9: Swing-up manoeuvre sequence [10]

Another aim of underactuated robotics is the study of brachiation, the locomotion strategy employed by long-armed apes, seen in **Figure 1.10**.

Figure 1.10: Ape brachiation sequence [11]

Two types of brachiation manoeuvres exist:

- Slow brachiation, where constant contact with a handhold is maintained
- Fast brachiation (ricocheting), which is defined by an aerial phase where there is no contact with a handhold

A number of underactuated robots have been designed over the years with varying purposes, discussed below are a few examples.

Brachiator II

Brachiator II [12] is a 2-link planar robot, shown in **Figure 1.11**, designed to study brachiation. It is a development of an earlier robot, Brachiator I, which is fully actuated. The robot features a coupled actuator at the elbow (link 2). Grippers are attached to the end of each arm, allowing the robot to grab onto horizontal handholds during brachiation. Discussed in **Table 1.1** are some of the research contributions and shortfalls of Brachiator II.

Figure 1.11: Brachiator II [12]

Table 1.1: Analysis of Brachiator II

Research Contribution	Shortfalls
• Focus on control strategies for achieving brachiation manoeuvres such as swing-up, ladder and rope problem as well as fast brachiation (ricocheting) • Development of a coupled motor mechanism using harmonic gears allowing for twice the rotational speed. Additionally, the mechanical structure achieves a better balance due to symmetric motors.	• Relies on wired connection to base station computer for operation • Constant brachiation is not energy efficient over long distances and increases chances of robot failure • No intended industrial application

SkySweeper

The SkySweeper robot [13], shown in **Figure 1.12**, is a prototype cable inspection robot. The robot has a planar double pendulum structure, with each arm having a multi-function gripper. It uses brachiation as a means to negotiate around obstacles on the line. The elbow joint (link 2) is actuated by a series elastic actuator which minimises the energy required to brachiate.

Figure 1.12: SkySweeper robot on a cable. The top two images [14], show the SkySweeper traversing the line using an inch-worn manoeuvre. The bottom image [15], shows the brachiation sequence.

In addition, the gripper allows the robot to passively grip the line, through friction, or roll along the line through an inch-worm manoeuvre which is more energy efficient than constant brachiation. Discussed in **Table 1.2** are some of the research contributions and shortfalls of SkySweeper.

Table 1.2: Analysis of SkySweeper

Research Contribution	Shortfalls
• Development of a prototype platform for line inspection • Novel gripper design allowing both pivoting and rolling of robot for locomotion • Series elastic actuator for energy efficient brachiation	• Inch-worm manoeuvre for locomotion lacks energy efficiency for traversing long distances • Relies on friction between pulley wheels and line to prevent slipping during brachiation, unreliable when the friction coefficient is low such as on actual conductors • Designed for small diameter cables and brachiation across small obstacles • Not designed for industrial application

Other works

Pendubot [16] is a desk-mounted two-link planar robot, for the development of non-linear control theory. It features an actuator at the shoulder (link 1) and a second link attached through a low friction rotational joint.

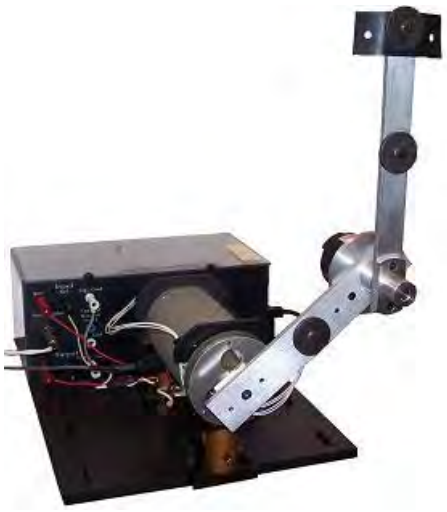

Figure 1.13: Pendubot robot [16]

Other two-link planar robots such as Acrobot [17] also exist. The key difference being the placement of the actuator. In Acrobot, the actuator is mounted on the second link instead of the first.

Control strategies implemented focus on stabilising the robot about its vertical equilibrium position.

1.3.2 Control strategies for underactuated robots

The control of underactuated systems is a research focus in control theory and thus a number of control strategies have been proposed. The solutions proposed vary considerably with a number of research papers written on each proposed solution.

Discussed below are three underactuated control strategies which aim to achieve brachiation and are therefore the most relevant to this work.

Target dynamics

In [18] a target dynamics control approach is introduced to solve the problems of continuous brachiation and swing-up. The two-link model used in the research can be seen in **Figure 1.14**.

The approach is based on the linearization of the standard dynamic model which is then forced to mimic a reference dynamic system. The robot generates and tracks this reference dynamic system, a harmonic oscillator in the case of [18], instead of tracking an external reference trajectory. Discussed in **Table 1.3** are some of the research contributions and shortfalls of the target dynamics approach.

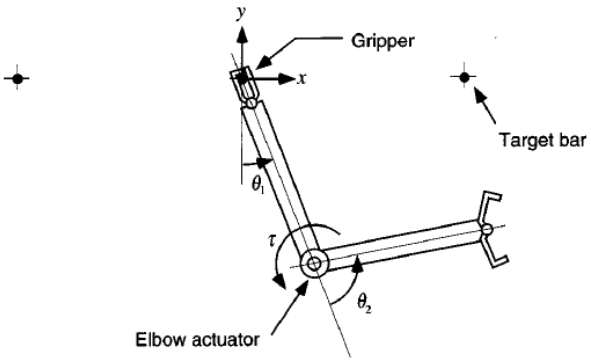

Figure 1.14: Target dynamics two-link planar model [18]

Table 1.3: Analysis of target dynamics control

Research Contribution	Shortfall
• Feedback reduces the complexity of the required model • An external reference trajectory is not required for brachiation manoeuvres • Successful brachiation and swing-up manoeuvres in both simulation and experiments	• Reference dynamic system requires careful tuning to best match actual system

Model predictive control

In [19, 20], a control strategy using MPC (Model predictive control) is proposed, which uses a model to determine the optimal control sequence by minimizing an objective function. At every control interval, the model is used to predict the behaviour of the system. These predications allow for the minimization of an objective function with respect to future control inputs.

Although the research focused on an MPC strategy for a 3-link planar robot, shown in **Figure 1.15**, the control strategy can be adapted for a 2-link robot and would be less computationally intensive due to a reduced DOF model. Discussed in **Table 1.4** below, are some of the research contributions and shortfalls of the MPC strategy proposed in the research.

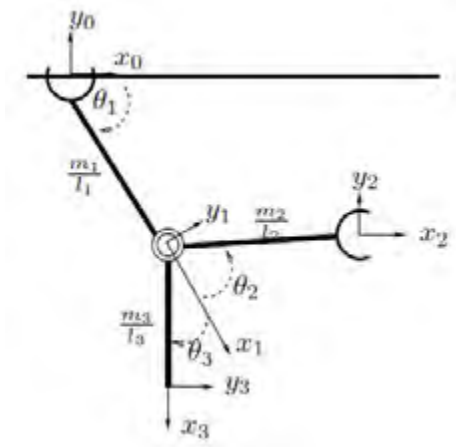

Figure 1.15: Three-link brachiation robot coordinate system [19]

Table 1.4: Analysis of model predictive control

Research Contribution	Shortfall
• An optimal control sequence, with respect to objective function, is derived allowing for the most efficient movement of the system • Ability to incorporate system constraints into control sequence generation • No reference trajectory required	• Highly accurate system model is required to predict system behaviour correctly • Computation time of online non-linear constrained optimisation is significant, thereby reducing control authority • Objective function is arbitrary, thereby making the 'optimal' control sequence somewhat relative

Other works

In [21] a heuristic control strategy is proposed which uses reinforced learning to achieve brachiation. The robot performs a number of trials, learning sub-optimal movements, without the use of a dynamic model. It then uses a neural model (Cerebellar Model Arithmetic Computer) to develop behaviours to react in unexperienced situations.

1.3.3 Power line inspection robots

The first power line robots appeared in the early 90's. Since then a number of robotic platforms have been developed, however the challenges faced when moving from a laboratory environment to the real world are significant. As such, only a few robots have been put into industrial use. Discussed below are three of the most successful line inspection robotic platforms.

LineScout

The LineScout [22] [23]is a mobile robot capable of semi-autonomous power line inspection and maintenance, developed by the Hydro-Québec Research Institute. It is an evolution of the LineROVer, seen in **Figure 1.16**, which was designed for the de-icing of power lines.

Figure 1.16: LineROVer robot on power line [24]

The LineScout, seen in **Figure 1.17**, has a unique design which incorporates three individual frames:

- Wheel frame, equipped with two motorised rubber wheels for driving along the line and two safety rollers
- Arm frame, equipped with two arms and two grippers, the latter being used during obstacle negotiation
- Centre frame, links the wheel and arm frame and allows for relative translation and rotation of the frames relative to one another.

Figure 1.17: LineScout performing obstacle negation of a suspension clamp [25]

The obstacle negotiation sequence, which takes approximately two minutes, is completed as follows:

- The robot is positioned as close to the obstacle as possible
- The arm and centre frames are rotated and extended such that the grippers are located on either side of the obstacle
- The grippers are then lifted until they clamp onto the conductor, this establishes a new support for the robot and the safety rollers are opened, releasing the wheel frame
- The wheel frame is then lowered, rotated and slid to the opposite side of the obstacle, it is then lifted onto the conductor and the safety rollers are closed once again
- Finally, the grippers are released and the arm and centre frame are lowered and slide back into position allowing the robot to continue inspection

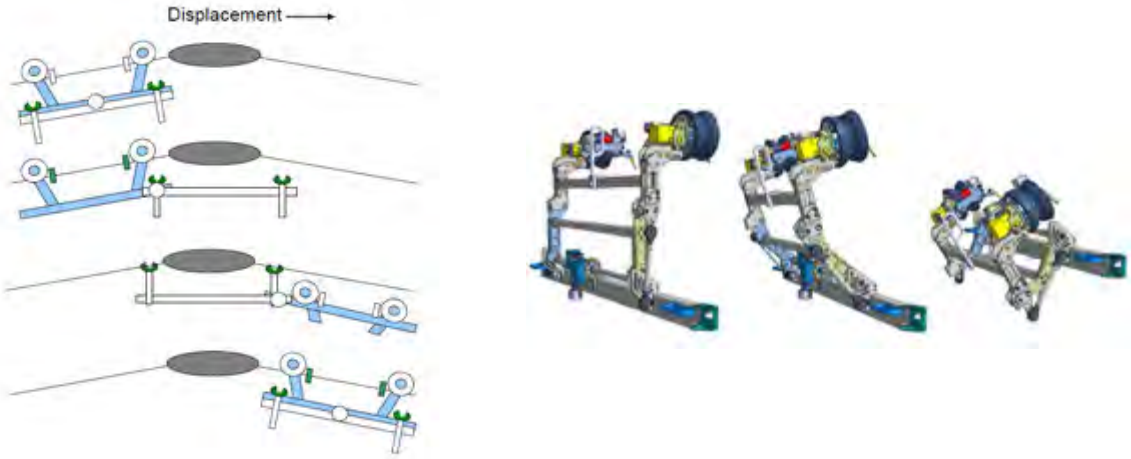

Figure 1.18: LineScout obstacle negation sequence. The image on the left [22]shows the obstacle negotiation sequence, with the image on the right [22] showing a 3D-CAD model of the movement of wheel frame during negotiation.

It has a number of strengths and weaknesses, which are discussed in **Table 1.5**.

Table 1.5: Analysis of LineScout robot

Strengths	Weaknesses
• Capable of crossing a large variety of line hardware • Capable of driving up a maximum slope of 25deg • Fast line traversal speed (1 m/s) • Robust to electromagnetic interference (735 kV – 1000 A) • Equipped with two LineArm's, capable of performing maintenance tasks such as applying temporary conductor clamps • Industrial application and operational experience	• Cannot negotiate jumper cables, multi-span inspection not possible • Kinematically complex design • Large number of actuators (11) • Relatively slow obstacle negotiation (2 minutes) • Heavy (100 kg), requiring high power actuators

Expliner

The Expliner [26] [27], is a semi-autonomous power line inspection robot developed by Hibot. The robot features two motion units for traversing the line. Each motion unit is comprised of two shafts, each with a pair of pulleys. A DC motor is fitted to one shaft and torque is transferred to the other by a timing belt. This design helps transmit the driving force across a greater surface area without using more actuators.

The motion units are mounted on a pole (labelled vertical pole in **Figure 1.19**) which is actuated and allows the wheels to rotate off the line during obstacle negotiation.

Figure 1.19: Expliner robot. The image on the left [28] shows Expliner approaching a spacer damper. The image [27] on the right shows the critical mechanical components of Expliner

The robot is equipped with a two-link, fully actuated manipulator. The manipulator controls the counter-weight position and consequently the robot is able to change the position of its COM which can be used for obstacle negotiation. The obstacle negotiation sequence is completed as follows

- The robot drives up to an obstacle as closely as possible
- The counter-weight position is manipulated such that the COM position shifts rearwards raising the from wheels
- The wheels are then rotated away from the line and the robot drives forward
- Once past the obstacle the front wheels are rotated back onto the line and the payload is shifted back to the neutral position
- The process is then repeated for getting the rear wheels past the obstacle

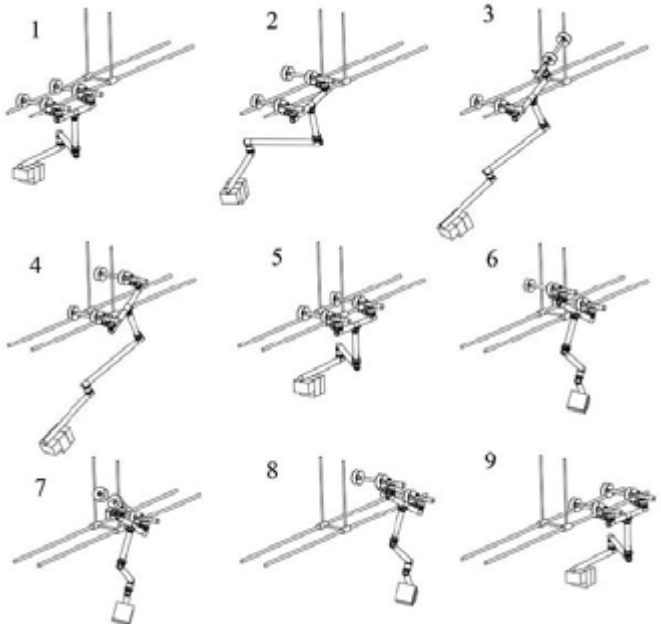

Figure 1.20: Expliner obstacle negotiation sequence [26]

The Expliner robot has a number of strengths and weaknesses, which are discussed in **Table 1.6**.

Table 1.6: Analysis of Expliner robot

Strengths	Weaknesses
• Capable of crossing a large variety of line hardware • Capable of driving up a maximum slope of 30deg • Controllability of position payload to shift COM advantageous in both obstacle negotiation and providing traction • Relatively low DOF and actuators (6) • Robust to electromagnetic interference	• Cannot negotiate jumper cables, multi-span inspection not possible • Slow line traversal speed (0.3 m/s) • Kinematically complex • Relatively slow obstacle negotiation (2 minutes) • Minimum distance between obstacles must be greater than the distance between two motion units • Heavy (approximately 80kg) therefore requires high power actuators

University of Kwa-Zula Natal Power Line Inspection Robot

The University of Kwa-Zulu Natal Power Line Inspection Robot (UKZN PLIR) [29, 30] is the most recently developed of the discussed robots. The robot employs the minimum number of DOF in order to negotiate obstacles, thus making it light-weight and relatively energy efficient. While performing obstacle negotiation, the robot can be represented as a serial manipulator with the detached gripper being the end-effector and the attached gripper, the base.

The robot has a gripper at the end of each arm which allows the robot to drive along the line. Each gripper has two wheels, a large drive wheel and a smaller wheel traction wheel. Additionally, the gripper can be rotated to increase the traction allowing the robot to traverse steep slopes.

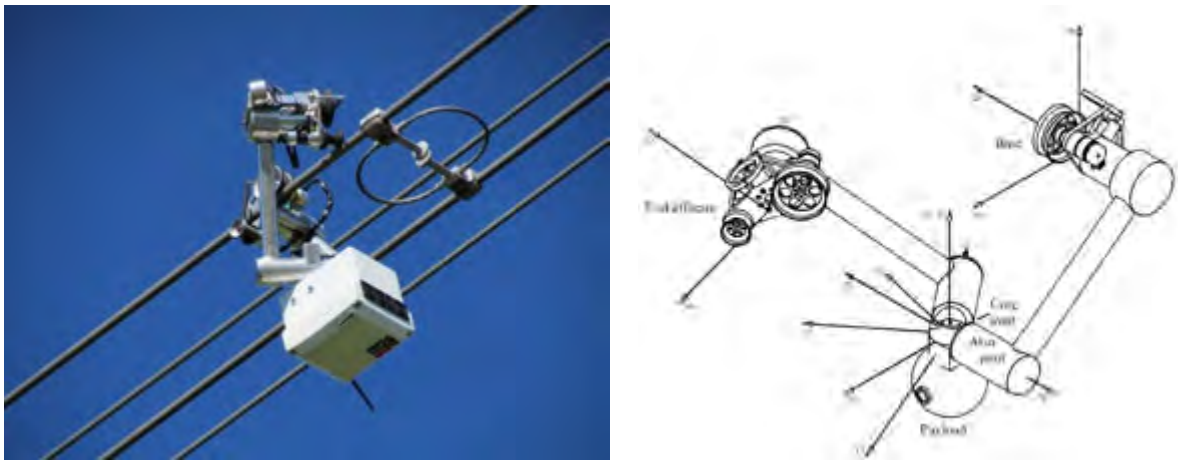

Figure 1.21: UKZN PLIR. Left [31], shows the robot performing obstacle negotiation of a spacer damper. Right [29], shows the kinematic layout of the robot.

The robot is capable of crossing all line hardware, including jumper cables. The obstacle negation sequence is as follows:

- The robot drives as close as possible to the obstacle
- The rear gripper is then rotated to lock onto the cable allowing for a secure anchor point
- The front gripper is then lifted off the and rotated away from the line
- The robot then drives forward and places the front gripper on the line
- Finally, the process is repeated for the rear gripper

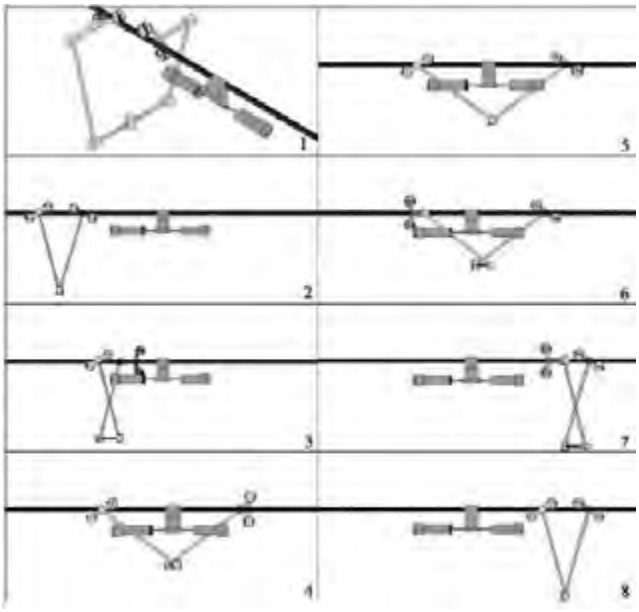

Figure 1.22: UKZN PLIR obstacle negotiation sequence [29]

The UKZN PLIR has a number of strengths and weaknesses, which are discussed in **Table 1.7**.

Table 1.7: Analysis of UKZN PLIR

Strengths	Weaknesses
• Capable of negotiating all line hardware including jumper cables, which allows multi-span inspection • Relatively light-weight (20 kg), allowing for lower power actuators • Low DOF (5) • Fast line traversal speed (1 m/s)	• Kinematically complex design • Relatively slow obstacle negotiation requiring high torque

1.4 Research objectives and dissertation outline

1.4.1 Research objectives

The research done on existing power line inspection robots reveal that even though successful, the mechanical design remains complex. Further, kinematically complex schemes, Expliner robot, or bulky static schemes, UKZN PLIR and LineScout, are employed for obstacle negotiation.

Therefore, in this project a robot that is mechanically simple while still being capable of handling the unpredictability of a real world environment, was sought.

The method of brachiation is selected for obstacle negotiation as it affords a simple obstacle negotiation sequence and favours a light-weight and compact design as fewer DOF are needed. In addition, the obstacle negotiation sequence is made highly energy efficient through the utilization, instead of compensation, of gravity.

A comparison of the obstacle negotiation sequence of the LineScout and the proposed robot design is shown in **Figure 1.23** for comparison.

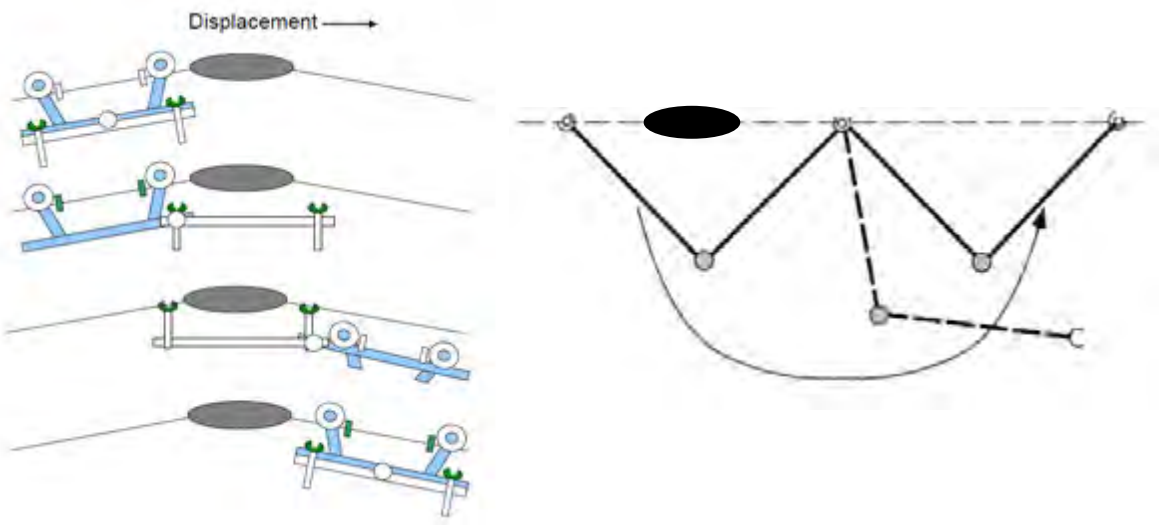

Figure 1.23: Comparison between LineScout [22] **and conceptual robot obstacle negation sequence** [32]

The detailed research objectives of this project are the design and development of a prototype line inspection robot, which shall be:

- Simple, robust, light-weight robotic platform capable of performing brachiation
- Capable of negotiating obstacles on the power line. Obstacles include:
  - Vibrational dampers
  - Compression dead-ends and planar jumper cables
  - Suspensions clamps
  - Spacers
- Capable of gripping onto and driving along power lines without damaging the conductor
- Capable of driving up an inclined conductor with a maximum slope of 30°
- Fail-safe to ensure robot failure does not result in robot falling from line
- Semi-autonomous, receiving high-level commands from operator, with pre-planned maneuvers for negotiating known obstacles
- Lightweight and compact for easy deployment by operators

Later requirements, which are essential for the industrialization of the robot, but are omitted from this dissertation, include the ability to:

- Operate on live conductors up to a voltage of 400kV
- Perform swing-up to recover from failed brachiation attempts
- Operate while carrying a payload of 5kg, this payload includes but is not limited to a multi-spectral camera for inspection
- Operate in the presence of Aeolian vibrations and cross-winds
- Operate for a minimum of 5 hours
- Store operational data for off-line analysis and maintenance logs

1.4.2 Scope and limitations

Since the focus of this research is the design of prototype line inspection robot, the robot will be operated in a controlled laboratory environment as this will allow the development of operational

robustness before moving into a real world environment. In addition, the robot will be isolated from environmental conditions such as wind and rain.

1.4.3 Dissertation outline

This dissertation is structured into five main themed sections as shown in **Figure 1.24**.

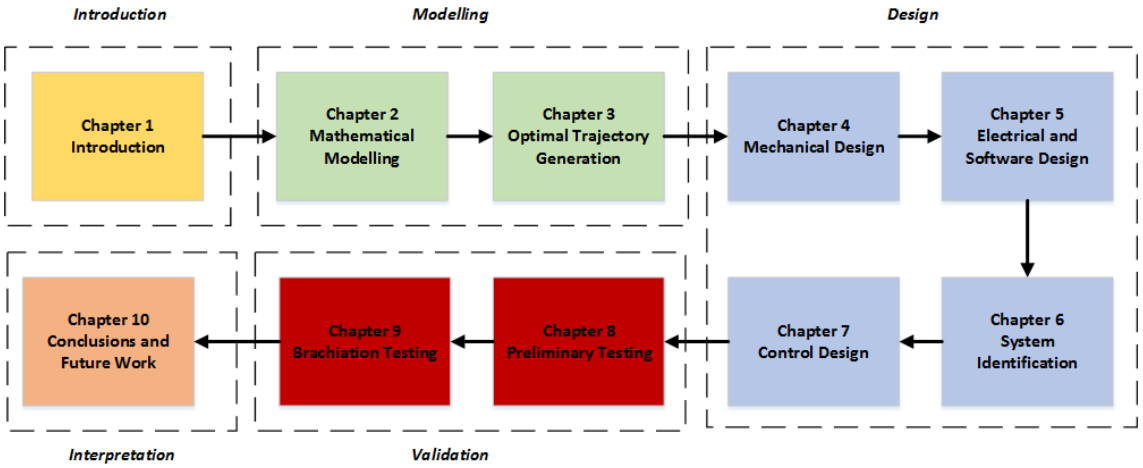

Figure 1.24: Dissertation layout

In **Chapter 2,** the mathematical modelling of the robot is derived. Modelling of friction and actuators is also discussed along with the four-bar mechanism used for the gripper.

In **Chapter 3,** the generation of an optimal trajectory using non-linear optimisation techniques is discussed. Additionally, a comparison between three proposed brachiating robot schemes is completed.

In **Chapter 4** and **Chapter 5** the mechanical and electrical design of the selected brachiation configuration is completed.

Chapter 6 focuses on validating the brachiation model through laboratory experiments as well as the identification of unknown parameters such as friction coefficients.

In **Chapter 7,** partial feedback linearization along with PID control is discussed. A static friction compensation technique critical in position control is also introduced.

In **Chapter 8,** the underlying sub-systems of the robot are tested, including gripper mechanical tests, vibrational noise, attitude estimation and position control. The brachiation manoeuvre is then tested in **Chapter 9**.

Finally, **Chapter 10** concludes the dissertation with a discussion of the work done, providing recommendations for future development of the prototype.

Chapter 2

Mathematical Modelling

The mathematical model of the system is crucial in correctly simulating the system's behaviour. This chapter will derive the mathematical models used for simulations in this dissertation.

An Euler-Lagrange modelling approach was used for obtaining the dynamics of the brachiating robot configurations and gripper linkage mechanism. The Euler-Lagrange approach [33, 34] can be described in brief as

1. First, a generalised coordinate vector is chosen, denoted by $q \in \mathbb{R}^n$. The size of q is defined by the number of degrees of freedom in the system, but can be made to include redundant degrees of freedom to model constraints [35]

2. The kinetic and potential energies of the bodies in the system are defined, where the kinetic energy is defined as

$$T = T_{translation} + T_{rotational} = \frac{1}{2}\left[\sum_{i=1}^{n} m_i \dot{r}_i^T \dot{r}_i + \omega_i^T I_i \omega_i\right] \tag{2.1}$$

   and, the potential energy as

$$V = \sum_{i=1}^{n} m_i g^T r_i \tag{2.2}$$

   where, n is the number of rigid bodies and i represents a property of the i_{th} body. m_i is the mass, $\dot{r}_i$ is the velocity of the COM, I_i is the inertia about the bodies COM,ω_i is the angular velocity, g is the gravitational vector and r_i is the position of the COM.

3. The Lagrangian is then defined as

$$L = T - V \tag{2.3}$$

4. The dynamics of the system can then be found by solving

$$\frac{d}{dt}\left(\frac{\partial L}{\partial \dot{q}_i}\right) - \frac{\partial L}{\partial q_i} = Q_i \tag{2.4}$$

where, Q_i represents the generalised forces acting on the rigid bodies of the system.

5. The Lagrange dynamics can then be expressed in terms of the standard manipulator equation in the following form:

$$M(q)\ddot{q} + C(q,\dot{q})\dot{q} + G(q) = B\tau + Q + A^T\lambda \tag{2.5}$$

where, $M \in \mathbb{R}^{nxn}$ is the non-singular mass matrix, $C \in \mathbb{R}^{nxn}$ is the Coriolis matrix, $G \in \mathbb{R}^n$ is the gravitational matrix, $B \in \mathbb{R}^n$ is the actuation matrix, τ is the actuation torque discussed in Chapter 2.4, $Q \in \mathbb{R}^n$ is the generalised force vector discussed in Chapter 2.5, $A \in \mathbb{R}^{nxm}$ is the constraint Jacobian and λ is the constraint force. Finally, n is the vector length of q and m is the number of constraints.

6. The equations of motion can then be calculated by manipulating (2.5)

$$\ddot{q} = M(q)^{-1}(-C(q,\dot{q})\dot{q} - G(q) + B\tau + Q + A^T\lambda) \tag{2.6}$$

The constraint force, which acts to constrain one or more of the system's degrees-of-freedom, can be found by solving (2.5), which results in

$$\lambda = -(AM(q)^{-1}A^T)^{-1}[AM(q)^{-1}(B\tau - C(q,\dot{q})\dot{q} - G(q) + Q) + A\ddot{q}] \tag{2.7}$$

2.1 Double pendulum

When attached to the line via a single gripper, the robot is modelled as a double pendulum with an actuator at the elbow joint (link 2), acting in a single plane. The planar assumption is valid since the obstacles on the power line can all be crossed while remaining in a single plane, except out-of-plane jumpers which require a rotation of the wrist and are outside the scope of this dissertation.

The generalised coordinates for the double pendulum modelling are shown in **Figure 2.1**, where the state vector, q, is chosen as

$$q = (\theta_1, \theta_2)^T \tag{2.8}$$

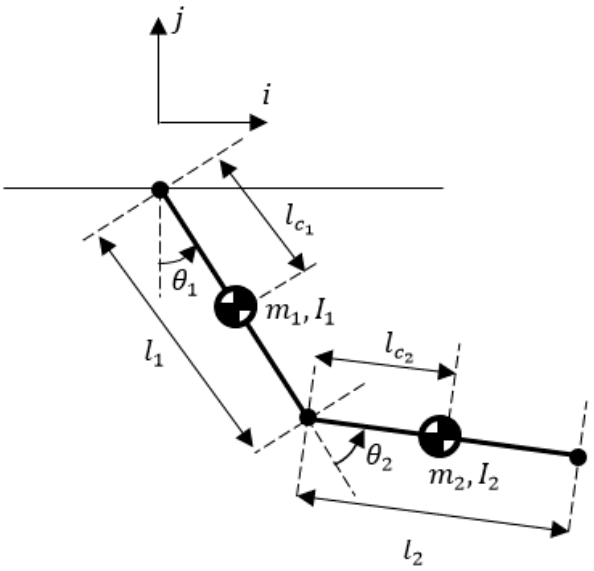

Figure 2.1: Generalised coordinates of double pendulum robot configuration

The coordinates of the COM of each rigid beam i_1, j_1, i_2 and j_2 can then be expressed as

$$i_1 = l_{c_1}\sin\theta_1 \tag{2.9}$$

$$j_1 = -l_{c_1}\cos\theta_1 \tag{2.10}$$

$$i_2 = i_1 + l_{c_2}\sin(\theta_1 + \theta_2) \tag{2.11}$$

$$j_2 = j_1 - l_{c_2}\cos(\theta_1 + \theta_2) \tag{2.12}$$

Using this, the kinetic and potential energy of the system is calculated, followed by forming the Lagrangian and subsequently, deriving the equations of motion.

The dynamics can be expressed in the standard manipulator form, as in (2.5). A detailed account of the matrix terms can be found in Appendix A.1.

Since the robot only has an actuator at the elbow, the actuation matrix B evaluates to

$$B = \begin{bmatrix} 0 \\ 1 \end{bmatrix} \tag{2.13}$$

Further, since no constraints are imposed on the model, the constraint Jacobian A evaluates to

$$A = 0 \tag{2.14}$$

The generalised force vector Q, is composed of two friction elements F_1 and F_2, where F_1 represents the friction between the attached gripper and the line and F_2 represents the joint friction. The friction terms are discussed in Chapter 2.5.

2.2 Double pendulum with constraints

The use of constraints allows for the analysis of the force at the point contact between the attached gripper and the power line. Knowing the reaction force caused during brachiation allows for the analysis of:

- The mechanical design using finite element analysis techniques and,
- The friction force as a function of the fluctuating normal force

The constraints are imposed on the system in the form of redundant variables. The generalised coordinates are shown in **Figure 2.2**, the state vector, q, is chosen as:

$$q = (x, y, \theta_1, \theta_2)^T \tag{2.15}$$

where x and y are the redundant variables used to impose the constraints.

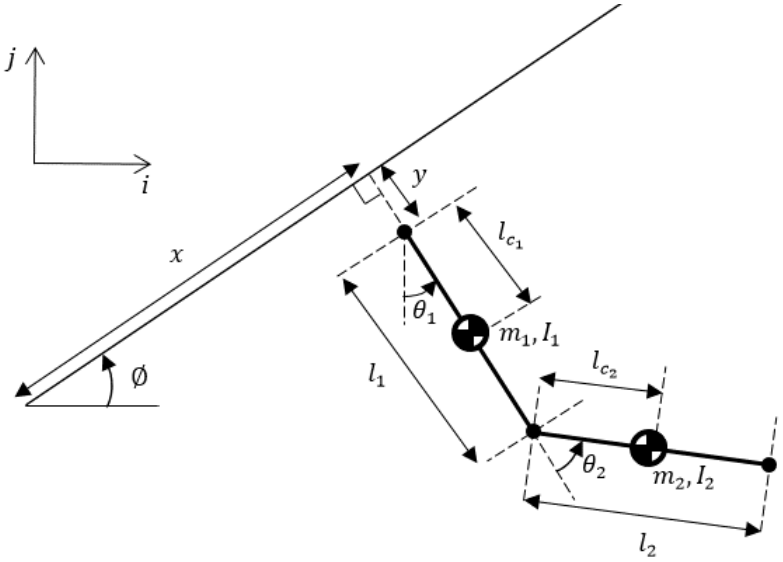

Figure 2.2: Generalised coordinates of double pendulum robot configuration with constraints

The coordinates of the COM of each rigid beam i_1, j_1, i_2 and j_2 can be expressed as:

$$i_1 = x\cos\emptyset + y\sin\emptyset + l_{c_1}\sin\theta_1 \tag{2.16}$$

$$j_1 = x\sin\emptyset - y\cos\emptyset - l_{c_1}\cos\theta_1 \tag{2.17}$$

$$i_2 = i_1 + l_{c_2}\sin(\theta_1 + \theta_2) \tag{2.18}$$

$$j_2 = j_1 - l_{c_2}\cos(\theta_1 + \theta_2) \tag{2.19}$$

In simulations, the redundant variables x and y are made to equal zero, thereby constraining the system.

The dynamics can be expressed in the standard manipulator form, as in (2.5). A detailed account of the matrix terms can be found in Appendix A.2.

The actuation matrix B is defined as

$$B = \begin{bmatrix} 0 \\ 0 \\ 0 \\ 1 \end{bmatrix} \tag{2.20}$$

Since constraints in the parallel and orthogonal direction, relative to the slope, are imposed. The constraint Jacobian A is defined as

$$A = \begin{bmatrix} 1 & 0 & 0 & 0 \\ 0 & 1 & 0 & 0 \end{bmatrix} \tag{2.21}$$

2.3 Triple pendulum

A triple pendulum model with actuators at the elbow (link 2) and wrist (link 3) is developed for the analysis of the optimal robot configuration for brachiation done in Chapter 3. The model forgoes constraints since the analysis is focused on the actuation torque required in different robot configurations. The generalised coordinates of the system are shown in **Figure 2.3**, the state vector, q, is chosen as

$$q = (\theta_1, \theta_2, \theta_3)^T \tag{2.22}$$

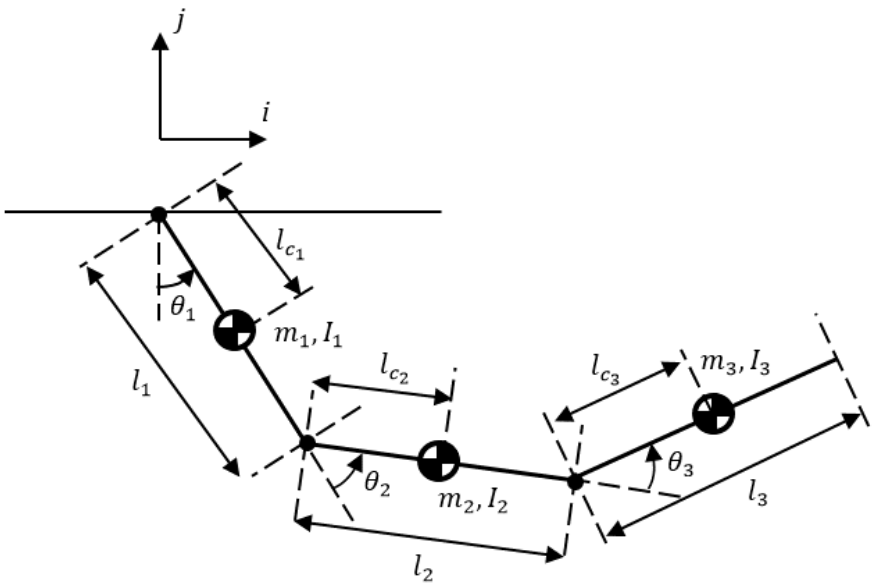

Figure 2.3: Generalised coordinates of triple pendulum robot configuration

The coordinates of the COM of each rigid beam i_1, j_1, i_2, j_2, i_3 and j_3 can be expressed as:

$$i_1 = l_{c_1} \sin\theta_1 \tag{2.23}$$

$$j_1 = -l_{c_1}\cos\theta_1 \tag{2.24}$$

$$i_2 = i_1 + l_{c_2}\sin(\theta_1 + \theta_2) \tag{2.25}$$

$$j_2 = j_1 - l_{c_2}\cos(\theta_1 + \theta_2) \tag{2.26}$$

$$i_3 = i_2 + l_{c_3}\cos\left(\theta_3 + \theta_1 + \theta_2 - \frac{\pi}{2}\right) \tag{2.27}$$

$$j_3 = j_2 - l_{c_3}\sin\left(\theta_3 + \theta_1 + \theta_2 - \frac{\pi}{2}\right) \tag{2.28}$$

The dynamics can be expressed in the standard manipulator form, as in (2.5). A detailed account of the matrix terms can be found in Appendix A.3.

Since the robot has two actuators, the actuation matrix B is defined as

$$B = \begin{bmatrix} 0 \\ 1 \\ 1 \end{bmatrix} \tag{2.29}$$

2.4 Motor model

A mathematical model of a DC motor is introduced [13] to simulate the actuator torque. The use of a motor model allows us to achieve a realistic simulation of the behaviour of the robot during brachiation. The actuation torque,τ, is modelled as

$$\tau = \eta(\sigma u - \varphi\omega) \tag{2.30}$$

$$\sigma = \frac{N k_m V_m}{R} \tag{2.31}$$

$$\varphi = \frac{N^2 {k_m}^2}{R} \tag{2.32}$$

where, σ is the stall torque, φ is the back EMF coefficient, η is the gearbox efficiency, N is the gearbox ratio, k_m is the motor constant, V_m is the motor voltage, R is the motor terminal resistance and $u \in [-1,1]$ is the control input.

2.5 Friction model

Friction is a highly complex phenomenon which a large number of research works have attempted to solve [36, 37]. The complexity of friction modelling stems partly from the fact that the model is highly material dependent, thus the friction model varies in different situations. However, since a friction model is necessary in order to properly simulate the dynamics of the robot, two simplistic friction models are considered in this dissertation.

Viscous friction model

In this model, the frictional force, denoted as $F_{friction}$, is purely a function of velocity with the friction model as

$$F_{friction} = f_v \omega \tag{2.33}$$

where, f_v is the viscous friction coefficient and ω is the rotational speed of the joint. **Figure 2.4** shows the relationship between frictional force and rotational speed.

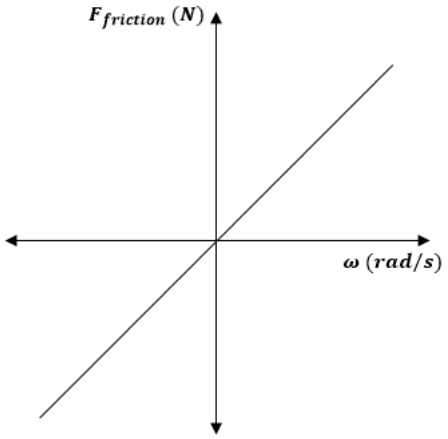

Figure 2.4: Friction model with only viscous friction

Coulomb and viscous friction model

A more complex friction model taking into account the effect of Coulomb friction is shown in **Figure 2.5**. This model is a more realistic representation of the friction in the system.

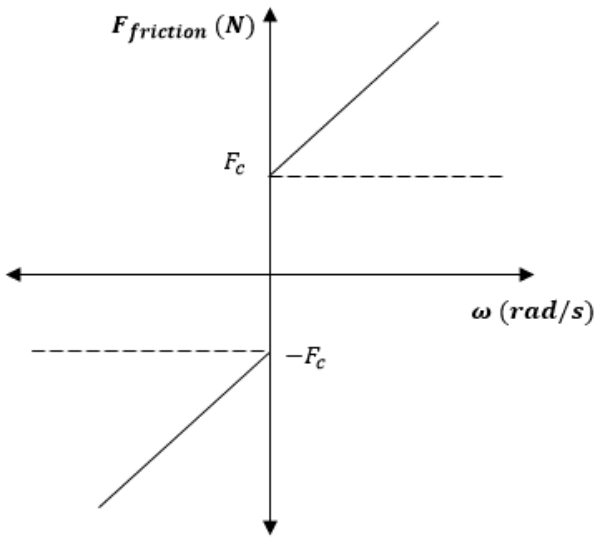

Figure 2.5: Friction model with coulomb and viscous friction

The model shown in **Figure 2.5** suffers from computational difficulties due to the non-linear nature of the frictional force at the origin, specifically as the friction does not obey the Lipschitz condition [38] at the origin. Therefore, a revised model, shown in **Figure 2.6** was introduced. In this model, a threshold velocity ω_{th} is introduced in order to smoothly transition from a zero velocity to non-zero velocity state.

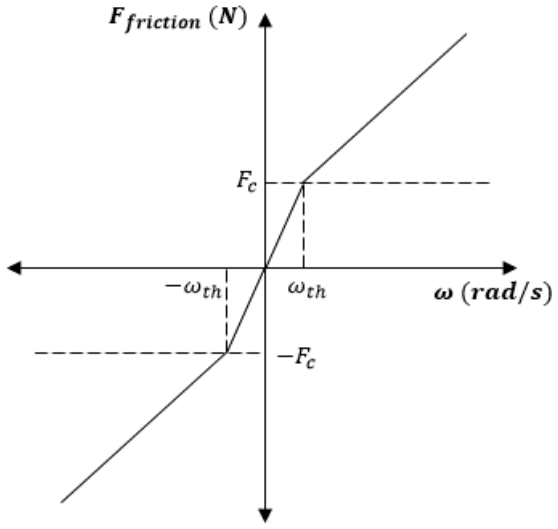

Figure 2.6: Friction model with coulomb and viscous friction

The friction can then be modelled as

$$F_{friction} = \begin{cases} \dfrac{F_c}{\omega_{th}}\omega \quad if\ |\omega| < \omega_{th} \\ F_c sign(\omega) + f_v\omega \quad if\ |\omega| \geq \omega_{th} \end{cases} \tag{2.34}$$

where F_c is the coulomb friction coefficient, ω_{th} is the threshold velocity, f_v is the viscous friction coefficient and ω is the angular velocity.

Despite being more realistic than the viscous friction only model, this model suffers from the fact that it is not Lipschitz continuous [38]. This introduces controller instability, discussed in Chapter 7. Therefore, the viscous friction only model is selected for the simulation of the frictional behaviour of the system.

2.6 Four-bar linkage mechanism

A four-bar mechanism model was developed to aid the design of the gripper, shown in Chapter 4.1. In conjunction with the four-bar synthesis discussed in Chapter 4.1.2, simulations of the mechanism aid in the selection of a number of critical design factors. These factors include

- Link lengths, which dictate the maximum opening and closing angles. Where the maximum opening angle affecting the opening distance to allow the power line to pass through.
- Link masses, which affect the opening and closing speed of the gripper
- Motor selection and gearbox ratio, which are crucial to the holding torque and speed of the gripper mechanism

The four-bar mechanism model is shown in **Figure 2.7** below. It consists of three moving rigid bodies labelled as crank, coupler and follower, which have associated lengths l_1, l_2 and l_3 respectively. The

fourth link is stationary and is labelled ground, with length l_0. The angles θ, α and $\emptyset$ are defined with respect to the horizontal and are non-constant, only angle μ is fixed.

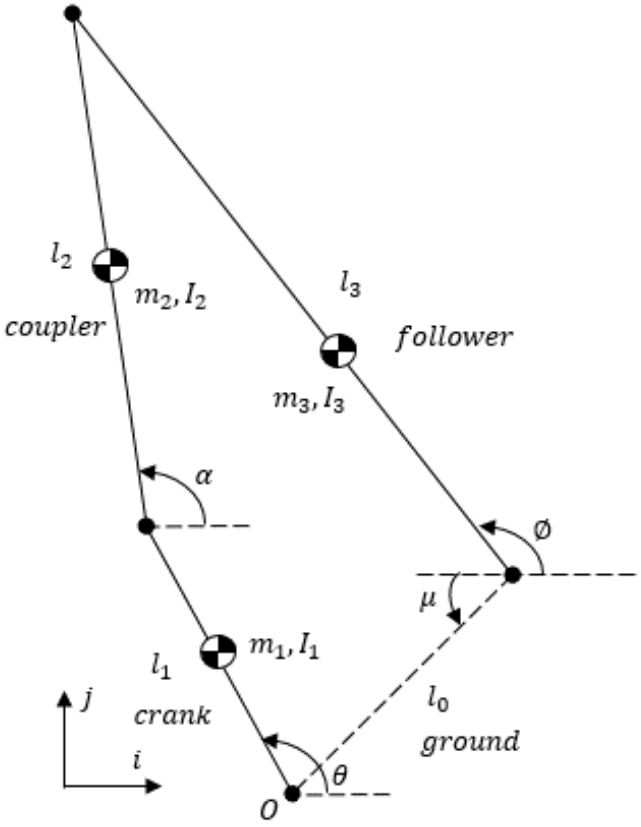

Figure 2.7: 4-bar mechanism coordinate system

The four-bar mechanism is modelled using the Lagrange modelling technique in [39]. This technique allows for the parametrization of the system by one coordinate, θ. The parametrization is done by eliminating the variables α and $\emptyset$ through position and velocity analysis as discussed below.

Position analysis

The four-bar mechanism is kinematically closed and therefore can be expressed in terms of two position loop-closure equations

$$i - constraint:\ l_0 \cos\mu - l_1 \cos\theta - l_2 \cos\alpha + l_3 \cos\emptyset = 0 \tag{2.35}$$

$$j - constriant:\ l_0 \sin\mu - l_1 \sin\theta - l_2 \sin\alpha + l_3 \sin\emptyset = 0 \tag{2.36}$$

The equations can then be written in terms of α as

$$i - constraint:\ l_2 \cos\alpha = l_0 \cos\mu - l_1 \cos\theta + l_3 \cos\emptyset \tag{2.37}$$

$$j - constriant:\ l_2 \sin\alpha = l_0 \sin\mu - l_1 \sin\theta + l_3 \sin\emptyset \tag{2.38}$$

By making use of the trigonometric identity

$$\sin^2 x + \cos^2 x = 1 \tag{2.39}$$

Equation (2.37) and (2.38) can be squared and summed together, which yields

$$k_1(\theta)\sin\emptyset + k_2(\theta)\cos\emptyset + k_3(\theta) = 0 \tag{2.40}$$

where,

$$k_1(\theta) = 2l_3(l_0\sin\mu - l_1\sin\theta) \tag{2.41}$$

$$k_2(\theta) = 2l_3(l_0\cos\mu - l_1\cos\theta) \tag{2.42}$$

$$k_3(\theta) = {l_0}^2 + {l_1}^2 - {l_2}^2 + {l_3}^2 - 2l_0l_1(cos\theta cos\mu + sin\theta sin\mu) \tag{2.43}$$

Equation (2.40) is a Freudenstein equation and can be solved in closed form. Through the method detailed in [39] the angles α and $\emptyset$ can then be written as:

$$\emptyset(\theta) = 2\arctan2(-k_1 \pm \sqrt{{k_1}^2 + {k_2}^2 - {k_3}^2}, k_3 - k_2) \tag{2.44}$$

$$\alpha(\theta, \emptyset) = \arctan2(-l_1\sin\theta + l_3\sin\emptyset, l_0\cos\mu - l_1\cos\theta + l_3\cos\emptyset) \tag{2.45}$$

Thus α and $\emptyset$ are now expressed in terms of θ and μ only.

Velocity analysis

The loop-closure equations, (2.37) and (2.38), can be differentiated with respect to time and expressed in matrix form as:

$$\begin{bmatrix} l_1\sin\theta & l_2\sin\alpha & -l_3\sin\emptyset \\ -l_1\cos\theta & -l_2\cos\alpha & l_3\cos\emptyset \end{bmatrix} \begin{bmatrix} \dot{\theta} \\ \dot{\alpha} \\ \dot{\emptyset} \end{bmatrix} = \begin{bmatrix} 0 \\ 0 \end{bmatrix} \tag{2.46}$$

Since we choose to parameterise the system using θ, the above equation can be rearranged as:

$$\begin{bmatrix} l_2\sin\alpha & -l_3\sin\emptyset \\ -l_2\cos\alpha & l_3\cos\emptyset \end{bmatrix} \begin{bmatrix} \dot{\alpha} \\ \dot{\emptyset} \end{bmatrix} = \begin{bmatrix} -l_1\sin\theta \\ l_1\cos\theta \end{bmatrix} \dot{\theta} \tag{2.47}$$

Following this,

$$\begin{bmatrix} \dot{\alpha} \\ \dot{\emptyset} \end{bmatrix} = \begin{bmatrix} S_1(\theta, \alpha, \emptyset) \\ S_2(\theta, \alpha, \emptyset) \end{bmatrix} \dot{\theta} \tag{2.48}$$

where,

$$S_1(\theta, \alpha, \emptyset) = \frac{\partial\alpha}{\partial\theta} = \frac{l_1\sin(\emptyset - \theta)}{l_2\sin(\alpha - \emptyset)} \tag{2.49}$$

$$S_2(\theta, \alpha, \emptyset) = \frac{\partial\emptyset}{\partial\theta} = \frac{l_1\sin(\alpha - \theta)}{l_2\sin(\alpha - \emptyset)} \tag{2.50}$$

The velocities $\dot{\alpha}$ and $\dot{\emptyset}$ can then be determined using (2.48).

Lagrange formulation

The Lagrangian can now be formulated where the kinetic energy is defined as

$$T = \frac{1}{2}\left(m_1|p_1|^2 + I_1\dot{\theta}^2\right) + \frac{1}{2}(m_2|p_2|^2 + I_2\dot{\alpha}^2) + \frac{1}{2}\left(m_3|p_3|^2 + I_3\dot{\emptyset}^2\right) \tag{2.51}$$

where,

$$|p_1|^2 = {l_{c_1}}^2\dot{\theta}^2 \tag{2.52}$$

$$|p_2|^2 = {l_1}^2\dot{\theta}^2 + 2l_1{l_{c_2}}^2\cos(\theta - \alpha)\dot{\theta}\dot{\alpha} + {l_{c_2}}^2\dot{\alpha}^2 \tag{2.53}$$

$$|p_3|^2 = {l_{c_3}}^2\dot{\emptyset}^2 \tag{2.54}$$

Where, p_i is the vector position of the COM, from the origin, of each rigid body. The potential energy of the system is defined as

$$V = m_1 g j_{c_1} + m_2 g j_{c_2} + m_3 g j_{c_3} \tag{2.55}$$

where,

$$j_{c_1} = l_{c_1}\sin\theta \tag{2.56}$$

$$j_{c_2} = l_1\sin\theta + l_{c_2}\sin\alpha \tag{2.57}$$

$$j_{c_3} = l_0\sin\mu + l_{c_3}\sin\emptyset \tag{2.58}$$

where, j_{c_i} is the position of the COM in the j-axis. Using this, the dynamics of the system can then be derived as described in [39].

Chapter 3

Optimal trajectory generation

The optimal trajectory for the robot when navigating around an obstacle, is framed as a trajectory optimisation problem, which is aimed at generating a trajectory for the robot under a set of constraints, while minimizing a cost function. An offline non-linear optimisation technique, as described in [40, 41], is used for the trajectory generation.

In general, non-linear optimisation techniques can be divided into two main classes: shooting methods and simultaneous methods. In shooting methods, a simulation is used to impose the system dynamics along the entire trajectory, whereas in simultaneous methods the system dynamics are only imposed at a set of points along the trajectory. Simultaneous methods are left out of this dissertation due to the complexity of their implementation.

Further, shooting methods can be sub-divided into single shooting and multiple shooting [41].

In single shooting a control input trajectory is approximated using a function which is usually a piecewise linear or piecewise cubic function, discretized into a variable number of segments. The optimiser then selects the control points, using a gradient-descent method, to generate a trajectory that satisfies the constraints while minimising a cost function. Single shooting is the simplest of the two to implement but has the disadvantage of having to use a single control input function to approximate the relationship between the decision variables and the objective and constraint functions along the entire trajectory. This may result in the optimiser not finding a feasible trajectory or finding ineffective solutions.

In multiple shooting, the trajectory is broken up into n segments and each segment is solved using a single shooting method. Increasing the number of segments creates an increasingly explicit relationship between decision variables and the objective and constraint functions. The end and start of adjacent segments may not line up and this results in what is known as a defect. These defects, shown in **Figure 3.1**, are then added to the system constraint vector which is made to be zero thereby aligning adjacent segments. This approach allows the optimiser to solve complex non-linear problems with a higher accuracy, albeit with increasing implementation complexity. **Figure 3.1** highlights the differences between single shooting and multiple shooting.

In this dissertation the optimal trajectories are computed using a single shooting method as opposed to multiple shooting since the models are simple enough to allow for accurate computation by single shooting methods. Additionally, the ease of implementation of a single shooting method allowed for rapid development of trajectories.

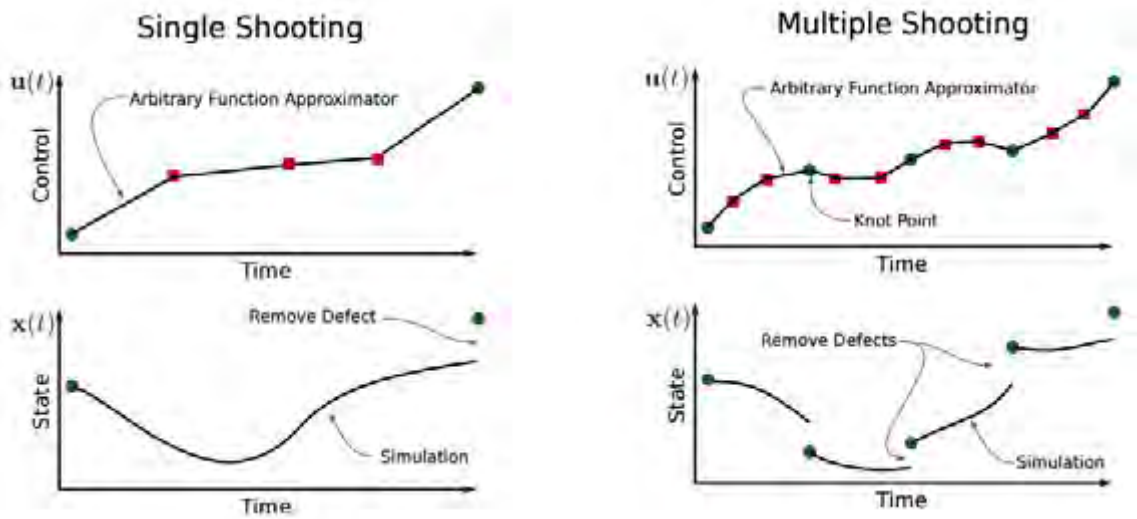

Figure 3.1: Single shooting vs. multiple shooting approach [41]

3.1 Analysis of mechanical configurations

The literature review in Chapter 1.3 reveals that brachiation is achieved most successfully with two and three-link robot configurations. Even though brachiation robots such as Brachiator III [42] which has 24 degrees-of-freedom (DOF) exist, this project is focused on the design of a robust and mechanically simple brachiation robot and therefore minimising the number of DOF is critical.

In addition to the number of links, the payload position is also considered since it affects the COM position. It comprises a large percentage of the robot mass and has a dramatic effect on the robot's dynamics. The movement of the payload can be used to affect the COM position as seen in the Expliner robot [27], where obstacle negotiation relies on this technique of payload position control.

Therefore, three optimal brachiation configurations are analysed to determine the best solution. An optimal configuration is defined as one which minimizes the actuation effort required for brachiation while reducing the mechanical and control complexities.

The three configurations are:

- A two-link configuration, with the payload split equally onto each link in a fixed position
- A two-link configuration, with the payload split equally onto each link but moveable along the length of the link
- A three-link configuration, with the payload on the middle link and moveable along the length of the link

A similar analysis of the optimal brachiation configuration was undertaken in a preliminary paper [43] written during the course of this dissertation but the results were later found to be incorrect due to a simulation setup error.

It should be noted that the payload positioning is not dynamic. The payload can only be shifted when the robot is stationary, not during brachiation. This reduces the mechanical complexity of the payload shifting mechanism and allows for a low power mechanism since the payload can be moved relatively slowly between swings.

The dynamics of the configuration models were discussed in Chapter 2. The models, shown **Figure 3.2**, are repeated here for convenience.

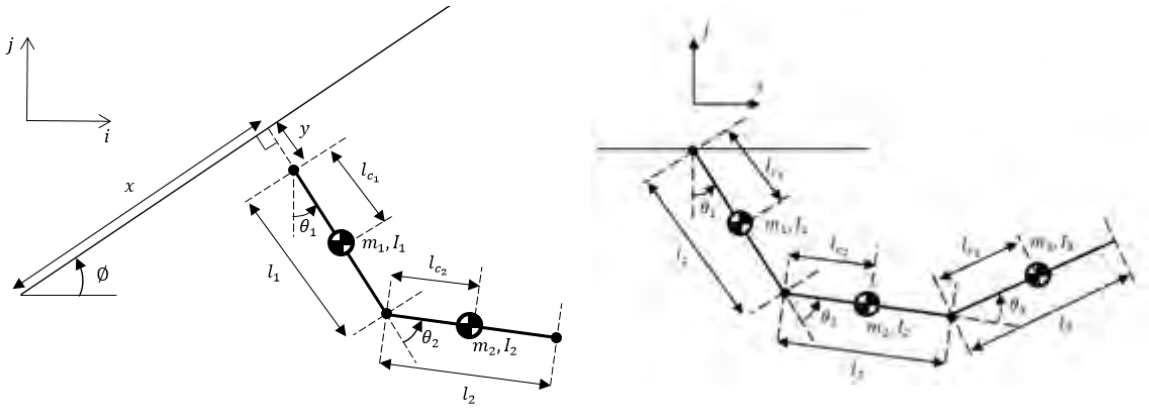

Figure 3.2: Two-link and three-link configuration models used for analysis of configuration selection

The link lengths of the configurations are based on the geometry required to negotiate a vibration damper on a horizontal conductor, discussed in Chapter 4.2.2. The configuration parameters are shown in **Table 3.1**.

Table 3.1: Robot Configuration parameters

Parameter	Two-link Fixed Payload		Two-link Moveable Payload		Three-link Moveable Payload		
	Link 1	Link 2	Link 1	Link 2	Link 1	Link 2	Link 3
m (kg)	5	5	5	5	1.5	7	7.5
l (m)	1	1	1	1	0.6	1	0.6
l_c (m)	0.5	0.5	0.2 – 0.8	0.2 - 0.8	0.3	0.2 – 0.8	0.3
I (kgm^2)	0.42	0.42	0.42	0.42	0.11	0.58	0.11
f_v $\left(\frac{\mathrm{Nms}}{\mathrm{rad}}\right)$	0.3	0.3	0.3	0.3	0.3	0.3	0.3

3.1.1 Configuration comparison

Brachiation scenario and simulation setup

The robot encounters a number of brachiation scenarios where line hardware such as vibration dampers, spacer dampers, suspension clamps and jumper cables need to be crossed.

The most challenging of these scenarios is the negotiation of jumper cables to enable multi-span inspections. The main difficulty is due to the steep incline at the connection between the jumper cable and the main conductor span. In addition, large actuation torque is required as the COM mass must be raised while brachiating and the jumper cable prevents the use of multiple swings as backward swings are obstructed by its presence. This is then the ideal scenario in which to compare the three configurations.

The configurations were simulated in open loop without disturbances to generate the optimal trajectories and determine the control effort needed to achieve brachiation. The optimal trajectories were obtained using Matlab's Fmincon algorithm, which is a constrained non-linear optimisation algorithm capable of performing single shooting.

The nonlinear optimiser finds the minimum of a problem specified as

$$\min_x f(x) \text{ such that } \begin{cases} c(x) \leq 0 \\ ceq(x) = 0 \\ A \cdot x \leq b \\ Aeq \cdot x \leq beq \\ LB \leq x \leq UB \end{cases} \tag{3.1}$$

where, $f(x)$ is a cost function, $c(x)$ and $ceq(x)$ are constraint functions, b and beq are vectors, A and Aeq are matrices, x is the optimisation parameters and, LB and UB are the upper and lower bounds of the optimisation parameters respectively.

The jumper-to-main conductor brachiation scenario, as well as all other scenarios, are defined by imposing constraints on the robot's initial and final position, as well as the velocity, acceleration and joint angles. The jumper-to-main conductor scenario is shown in **Figure 3.3**.

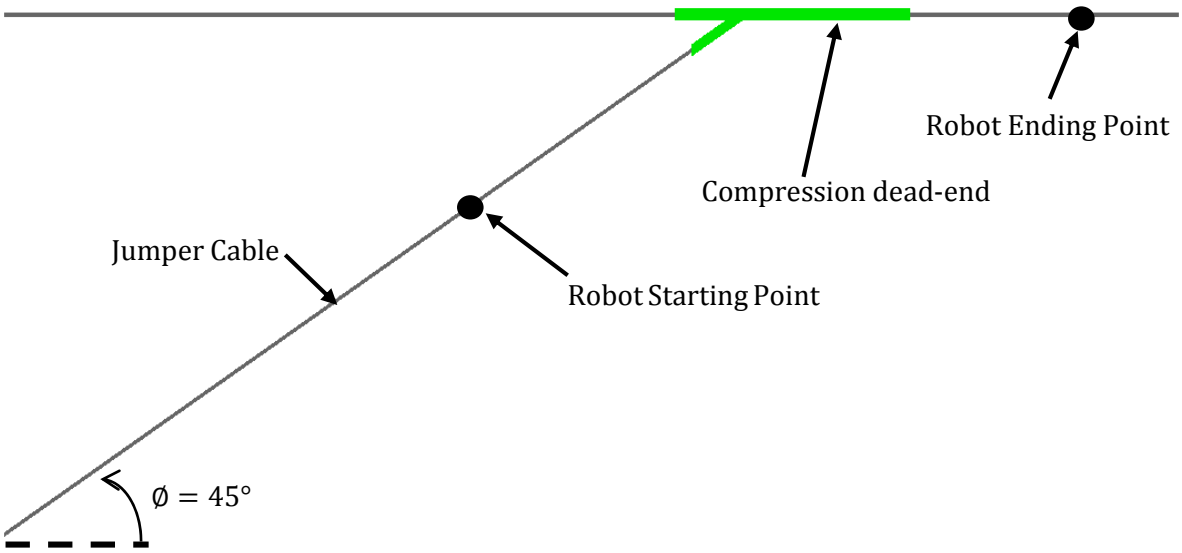

Figure 3.3: Jumper-to-main conductor brachiation scenario setup

The jumper-to-main conductor brachiation scenario can be split into two phases. The first phase being where the robot swings from the jumper cable to the main conductor. At the end of this phase, one link is on the jumper and the other on the main conductor. The second phase is then where the ends with both its links on the conductor. The end of the two phases of a jumper-to-main conductor swing can be seen in **Figure 3.4**. Only the two-link configuration is shown but the same would apply to the three-link configuration.

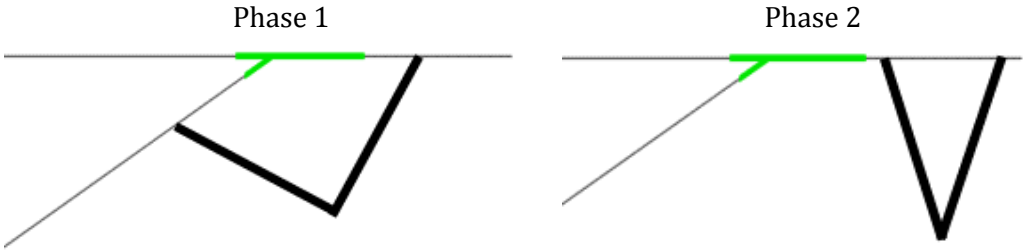

Figure 3.4: Two phases of jumper-to-main conductor brachiation sequence

The parameters used for the simulations are:

- Initial joint angles, to determine the optimal starting orientation for the configuration
- Swing time, to achieve the minimum control effort depending on the dynamics of the particular configuration
- Actuator torque, to achieve brachiation
- COM position, as a result of moving payload, to achieve minimum control effort. Only applies to configurations with moveable payloads.

In order to achieve minimal energy brachiation, the cost function is defined as

$$Cost = \int_{t_{initial}}^{t_{final}} \sum_{i=1}^{n} \tau_i^2 dt \tag{3.2}$$

where, τ_i is the actuator torque for joint i, dt is the sampling time and n is the number of actuated joints.

Analysis of configuration torque requirements

The torque required to perform the jumper-to-main conductor swing was analysed in order to aid in determining the optimal configuration which would best suit the requirements of this project. The brachiation sequences of the configurations for the first phase of the jumper-to-main conductor swing are shown in **Figure 3.5** and **Figure 3.6**.

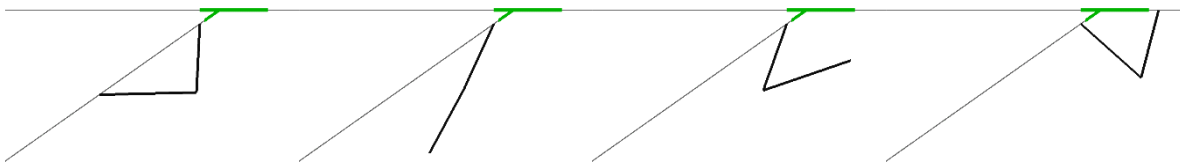

Figure 3.5: Two-link configuration jumper-to-main conductor phase 1 sequence

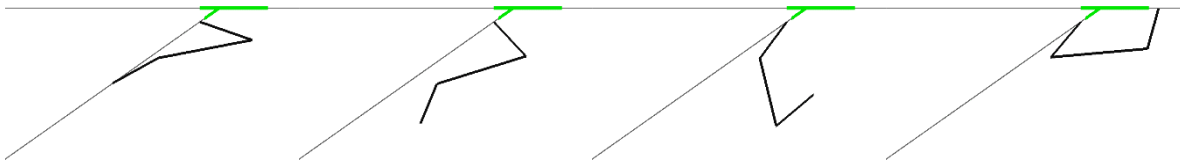

Figure 3.6: Three-link configuration jumper-to-main conductor phase 1 sequence

It should be noted that the motor model discussed in Chapter 2.4 is neglected in these simulations to simplify the configuration comparisons. The final trajectory generation in Chapter 3.2 will include the motor model to ensure the dynamics are realistically modelled. **Figure 3.7** shows a comparison of the torque required to complete the first phase of the jumper-to-main conductor.

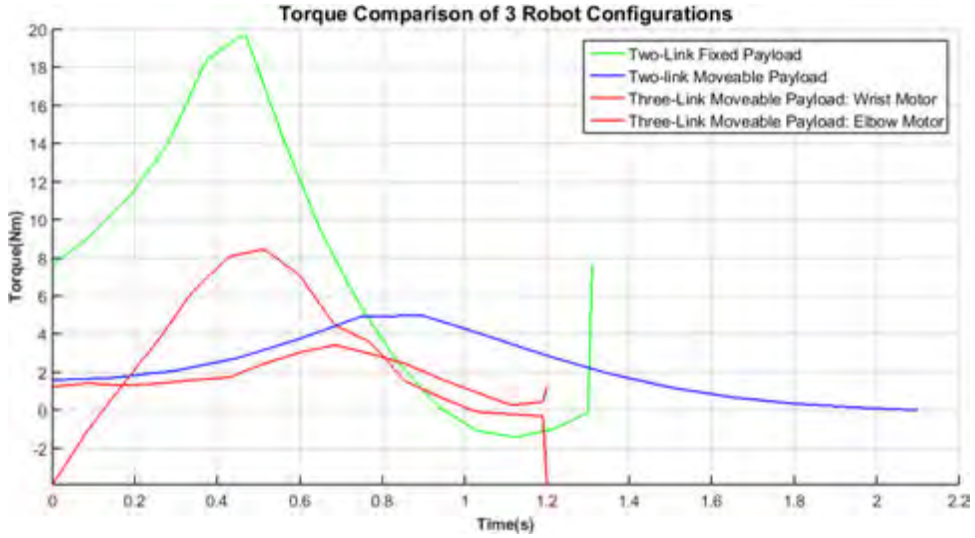

Figure 3.7: Required actuation torque for configurations while performing jumper-to-main conductor swing phase one

From **Figure 3.7** it can be seen that the Two-link Moveable Payload configuration requires a third of the maximum torque of the Two-link Fixed Payload. This means that a significant torque reduction is gained through the movement of the payload. However, since the Three-link configuration has two actuators, a better comparison between the Two and Three-link Moveable Payload configurations may be done by assessing the power required to perform the swing, as seen in **Figure 3.8**. It should be noted that the control input trajectory (torque) was approximated using a piecewise linear function and therefore the torques may appear discontinuous.

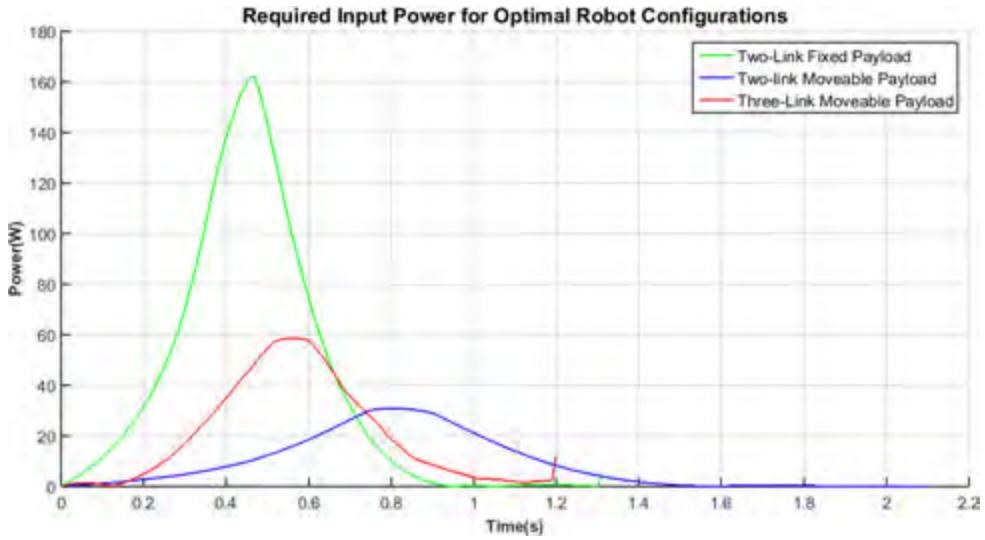

Figure 3.8: Required input power for different robot configurations

From **Figure 3.8** it can be seen that the Two-link Moveable Payload configuration has the lowest peak power requirement. Further, the energy required for brachiation can be calculated as

$$E = \int_{t_{initial}}^{t_{final}} P dt \tag{3.3}$$

where, P is the power. By comparing the required energy for each configuration, shown in **Table 3.2**. We see that the Two-link Moveable Payload is the most energy efficient configuration. It should be noted that the energy required to move the payload is not taken into account since the payload can be moved while the robot is stationary and the focus is on the energy required for brachiation.

Table 3.2: Required input energy for robot configurations

Configuration	Required Energy (J)
Two-link Fixed Payload	51.7
Two-link Moveable Payload	18.4
Three-link Moveable Payload	24.1

The reduction in required actuation torque when compared to the fixed payload scheme is due to the COM of each link being shifted such that the double pendulum has a slower rotational frequency and therefore has more time to pump energy into the system. **Figure 3.9** shows the differences between the COM positions between the Two-link Fixed Payload configuration and the Two-link Moveable Payload configuration.

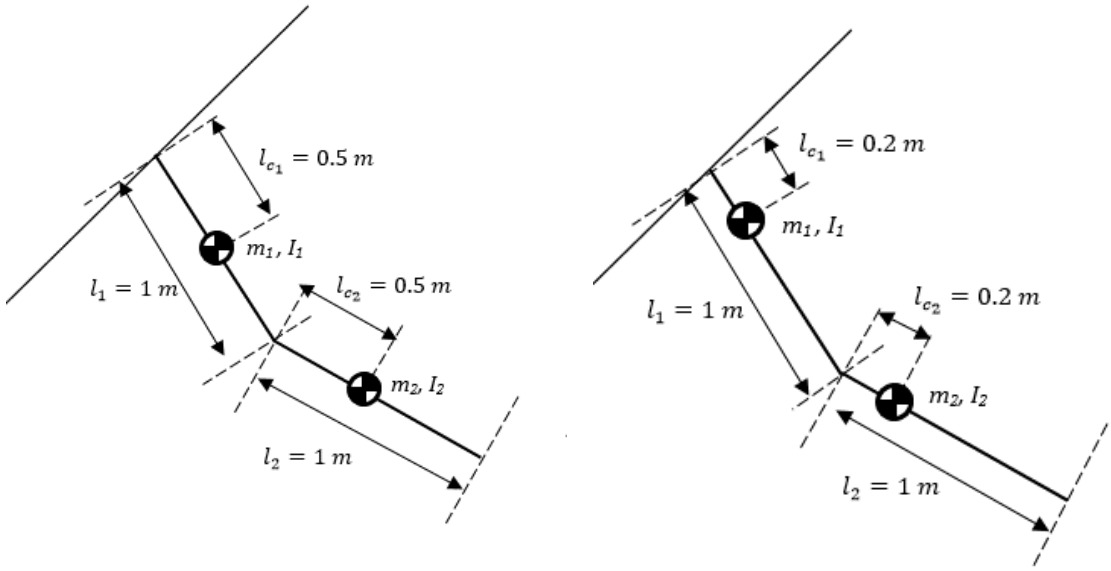

Figure 3.9: Differences between COM position of Two-link Fixed Payload and Two-link Moveable Payload configuration for first phase

Thus by being able to move the payload along the link's length, consequently adjusting the COM position, significant torque reduction is achieved.

Next, the second phase of the jumper-to-main conductor brachiation swing is analysed. The brachiation sequences of the configurations for the second phase of the jumper-to-main conductor swing are shown in **Figure 3.10** and **Figure 3.11**.

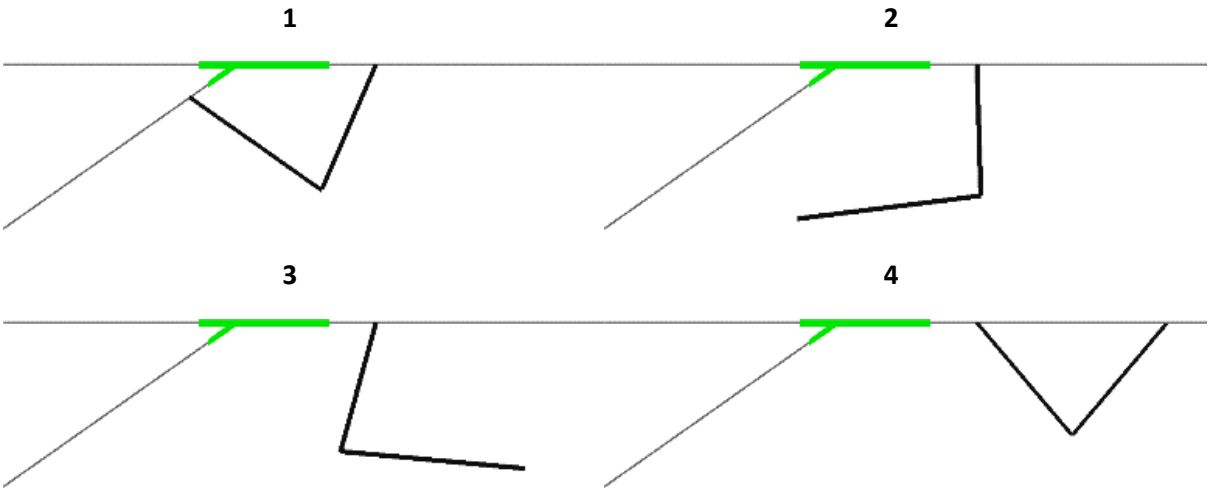

Figure 3.10: Two-link configuration jumper-to-main conductor phase 2 sequence

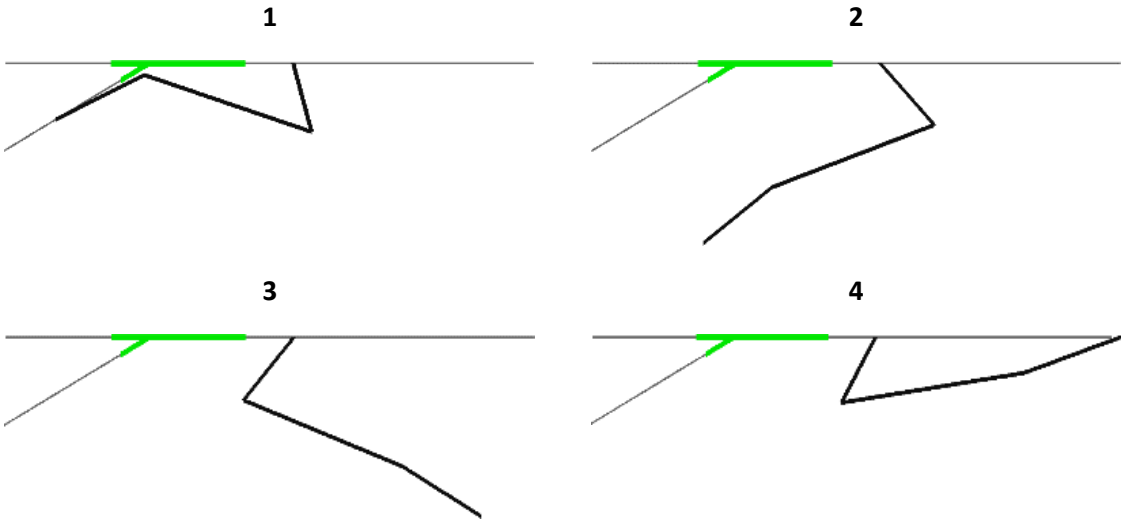

Figure 3.11: Three-link configuration jumper-to-main conductor phase 1 sequence

The required torque and power for the three configurations are shown in **Figure 3.12**. In the second phase of the swing, the configurations have similar swing durations and the Three-link Moveable Payload configuration is the most energy efficient and has the lowest peak power requirement.

Further, to analyse the effect of moving the payload to shift the COM. **Figure 3.13** shows the actuation torque required when the payload position for the Two-link Moveable Payload configuration is kept constant between phase 1 and phase 2 of the swing vs. where the payload is shifted to an optimal position before performing the swing.

From **Figure 3.13** it can be seen that moving the payload to an optimal position before brachiation has a dramatic effect on the required torque. The torque required when the payload is kept constant between swing phases 1 and 2 is significantly higher than the torque required when the payload is shifted to an optimal position.

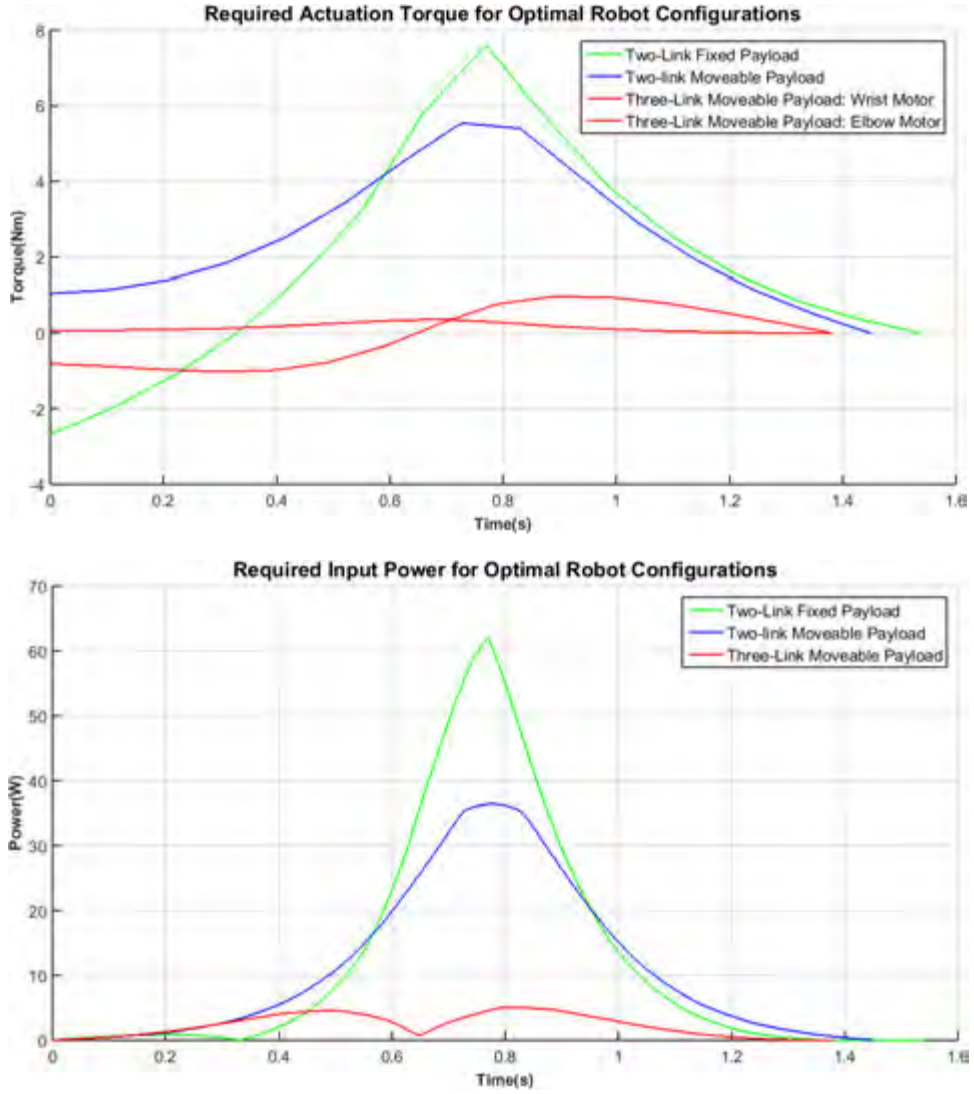

Figure 3.12: Torque and input power comparison for different configurations

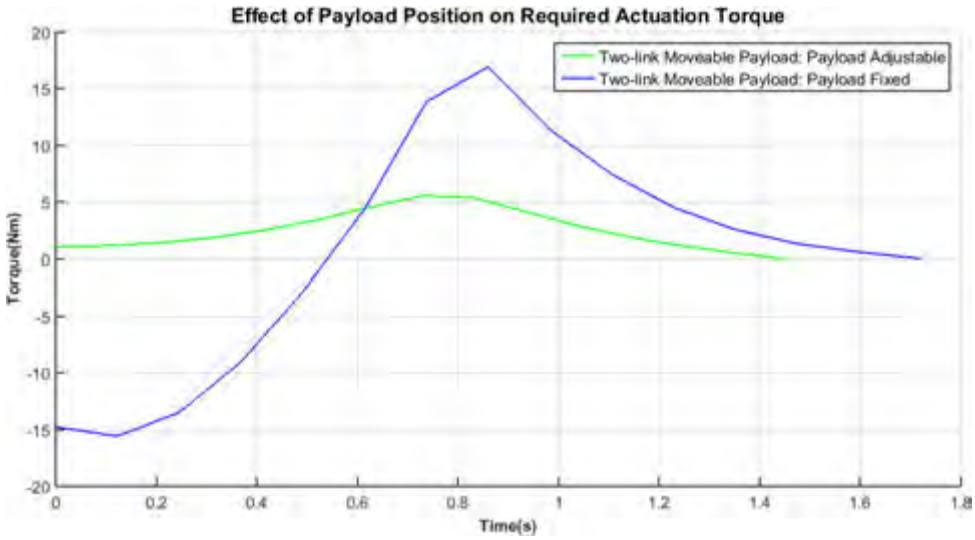

Figure 3.13: Effect of positioning payload before second phase of jumper-to-main conductor swing

Selection of configuration

The analysis of the three optimal configurations show that the Two-link Moveable Payload configuration is the most energy efficient for the first phase of the jumper-to-main conductor manoeuvre. In the second phase of the swing, the Three-link Moveable configuration is more energy efficient but since the first phase of the swing is significantly more challenging, the results of the first phase bear more weight.

Therefore, the Two-link Moveable Payload configuration is the optimal solution amongst the studied configurations. In addition, the Two-link configuration is mechanically simpler and easier to control due to reduced DOF.

For the prototype developed as a proof of concept in this project, the Two-link Fixed Payload configuration was selected in spite of it being the least energy efficient. It presents the least mechanical and control complexity and ultimately leads to a solution with higher operational robustness. The focus of this project is the design of a prototype brachiation robot which is mechanically simple and robust and therefore the higher torque requirements of the Two-link Fixed Payload are achieved by using an appropriately specified motor, thus avoiding the mechanical complexity of having to shift the payload.

While the payload position and hence COM position is fixed, the results above are used to determine the optimal position for the payload such that both phases of the swing have the lowest energy requirement.

In future development of the robot a payload positioning mechanism may be incorporated to leverage the advantageous effect of shifting the COM before brachiation.

3.2 Generation of optimal trajectories

The optimal trajectories for the robot can be refined using the final mechanical design specifications developed in Chapter 4.

By using the Two-link configuration model with constraints, developed in Chapter 2.2, the dynamic reaction forces at the gripper are calculated. These forces are then used in an iterative mechanical design process, as shown in **Figure 3.14**.

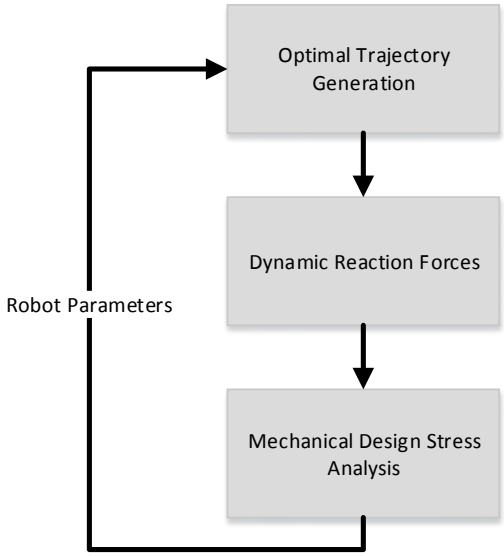

Figure 3.14: Interaction between trajectory generation and mechanical design

The final specifications of the robot are shown below in **Table 3.3**. The robot parameters, excluding friction coefficients, are determined using a detailed Solidworks model.

Table 3.3: Designed robot parameters

Robot Parameter	Value	Unit
m_1	3.221	kg
m_2	4.178	kg
l_1	1	m
l_2	1	m
l_{c_1}	0.430	m
l_{c_2}	0.602	m
I_1	0.285	kgm^2
I_2	0.191	kgm^2
f_{c_1}	unknown	Nm
f_{c_2}	0.3	Nm
f_{v_1}	unknown	$\frac{\mathrm{Nms}}{\mathrm{rad}}$
f_{v_2}	0.25	$\frac{\mathrm{Nms}}{\mathrm{rad}}$

As discussed in Chapter 4.1.4, due to time and cost constraints only one gripper was manufactured, thereby altering the robot specifications in **Table 3.3**. Thus, the final parameters of the robot used for the trajectory generation are shown in **Table 3.4**.

Table 3.4: Final robot parameters

Robot Parameter	Value	Unit
m_1	4.071	kg
m_2	2.188	kg
l_1	0.798	m
l_2	1	m
l_{c_1}	0.379	m
l_{c_2}	0.634	m
I_1	0.1085	kgm^2
I_2	0.1829	kgm^2
f_{c_1}	0.25	Nm
f_{c_2}	0.3	Nm
f_{v_1}	0.15	$\frac{\text{Nms}}{\text{rad}}$
f_{v_2}	0.25	$\frac{\text{Nms}}{\text{rad}}$

The friction coefficients are determined in Chapter 6 using experimental data.

The feasibility of various motors was assessed using the trajectory generation simulations coupled with the motor model, discussed in Chapter 2.4. A Maxon EC motor with ceramic planetary gearbox, shown in **Figure 3.15**, was selected as it best satisfied the requirements of the robot and allowed for successful brachiation in various scenarios. Critical motor and motor controller parameters are highlighted in **Table 3.5**.

.

Figure 3.15: Maxon motor combination. From left to right, 200W Maxon EC motor [44], ceramic planetary gearbox [45] and motor controller [46] respectively.

Table 3.5: Motor and motor controller parameters

Unit	Parameter	Value	Unit
Motor and Gearbox	Nominal voltage	48	V
	Nominal current	3.68	A
	Stall current	124	A
	Nominal torque	0.0929	Nm
	Stall torque	3.43	Nm
	Motor torque constant	0.634	Nm/A
	Gearbox ratio	74	–
	Maximum gearbox efficiency	72	%
Motor Controller	Maximum current (< 20 seconds)	15	A
	Maximum continuous current	5	A

Using the robot parameters in **Table 3.4** an optimal trajectory for crossing a vibration damper, one of the most common obstacles on a conductor, was generated. **Figure 3.16** shows the brachiation sequence for crossing a vibration damper.

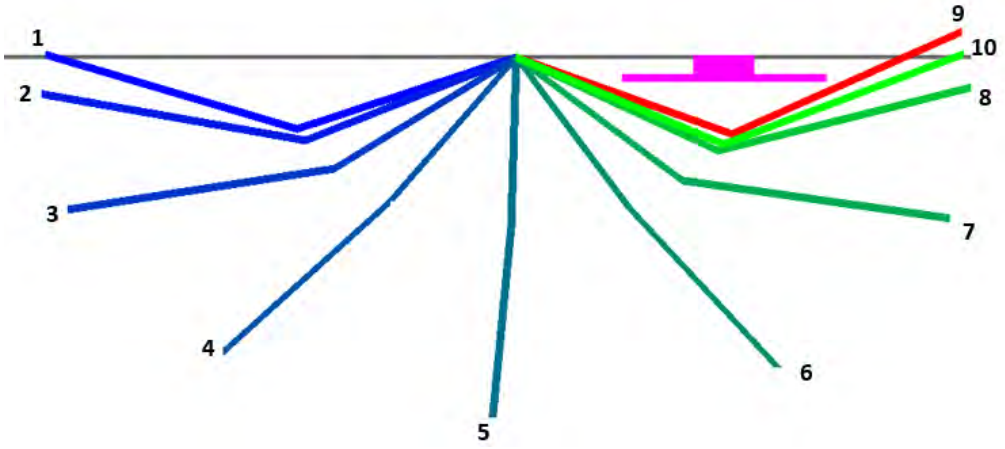

Figure 3.16: Vibration damper brachiation sequence phase 1

The initial position and final positions of the robot are shown in blue and green respectively. An overshooting phase can be seen in red in **Figure 3.16**. This overshoot is designed into the trajectory to ensure that the robot brachiates successfully in the presence of unmodelled or inaccurately modelled disturbances. The overshooting phase occurs at relatively low angular speeds and will therefore not damage the robot. Further, a controller which is able to regulate the height of the robot from the line will be implemented in the final version of the robot, preventing collisions with the line. The details of the controller will be discussed in Chapter 7. The detailed results of the vibration damper negotiation sequence including robot angles, speeds, motor torque and reaction forces can be found in Appendix B.

The second phase of the vibration damper brachiation sequence is symmetric with the first and is shown in **Figure 3.17**.

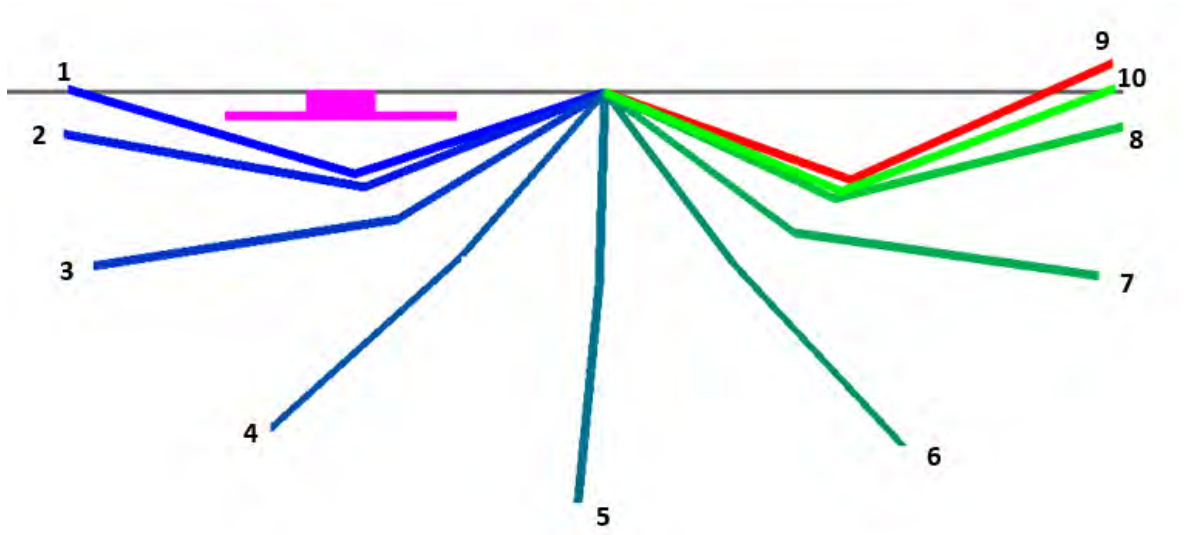

Figure 3.17: Vibration damper brachiation sequence phase 2

Other obstacles on the conductor such as spacer dampers and suspension clamps can be crossed using the same brachiation sequence as the vibration damper brachiation.

A swing up trajectory is generated to recover from failed brachiation attempts, essential for operating in a real-world environment where brachiation might fail due to unforeseen disturbances. The swing up manoeuvre for the robot is different to the one discussed in Chapter 1.3.1 as in this case the robot's desired end state is with its free gripper on the conductor instead of a vertical equilibrium position. The swing up manoeuvre for the robot is shown in **Figure 3.18**.

The detailed results of the swing up manoeuvre including robot angles, speeds, motor torque and reaction forces can be found in Appendix B.

Finally, the robot was simulated performing a jumper-to-main conductor brachiation manoeuvre, the results of which can be found in Appendix B.

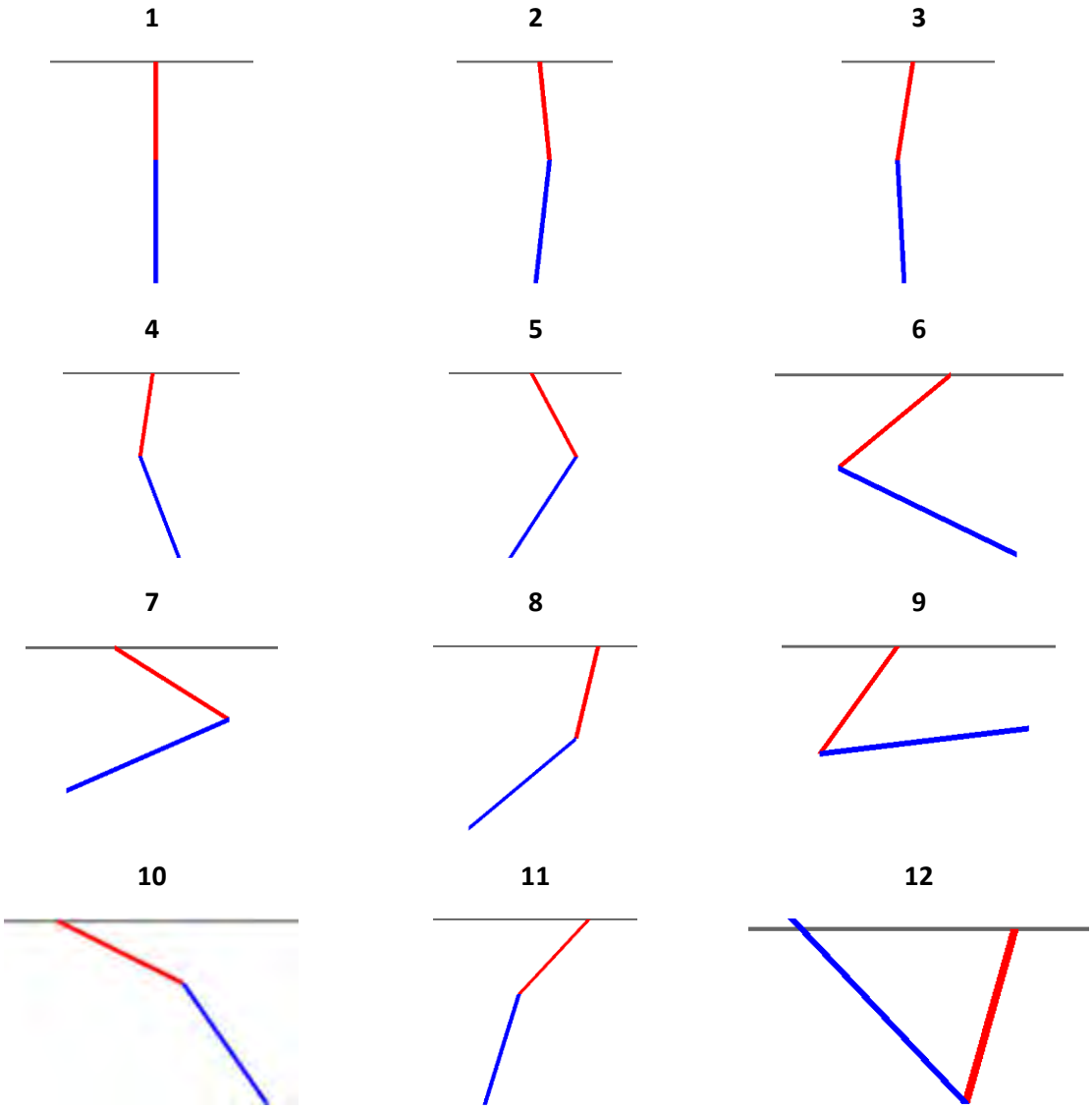

Figure 3.18: Swing up manoeuvre for recovering from failed brachiation

Chapter 4

Mechanical design

The success of the robot is dependent on the systematic design of the mechanical structure. Through proper mechanical design techniques and analysis, a robust and industrially capable robot is designed.

From the requirements laid out in Chapter 1.4.1 and the results of the configuration analysis in Chapter 3, the broad mechanical design requirements can be defined as

- The design of a two-link fixed payload mechanical structure, having a gripper at the end of each link
- A mechanical structure capable of performing brachiation for obstacle negotiation
- Design of a multi-functional gripper capable of gripping onto the conductor and enabling the robot to drive along conductors

The mechanical design is broken into two main sections, the design of a multi-functional gripper and the design of the link actuation mechanism.

4.1 Gripper design

The gripper is a critical component in the mechanical design as it serves as the connection point between the entire robot structure and the conductor.

The gripper acts as a pivoting point for the robot during brachiation supporting its entire weight for the duration of the swing. Therefore, the gripper must be mechanically robust to prevent the robot from falling off the line.

In addition, the gripper must grip onto the line without rolling or sliding during brachiation. This is critical when brachiating on an inclined conductor since sliding of the robot will mean that the robot will fail to brachiate across the obstacle and could potentially damage the swinging gripper if it collides with the obstacle.

Finally, the gripper must be capable of driving the robot along the line. This mode of locomotion offers a number of advantages over constant brachiation, such as

- Energy efficiency, driving along the line requires less energy than constantly brachiating.
- Stabilised payload, the payload is kept relatively stable during locomotion. Critical for visual inspection.
- Operational integrity, even though the robot is capable of brachiating, the manoeuvre is highly dynamic when compared to simply driving along the conductor. Driving along the conductor therefore has a lower chance of failure.

The gripper design follows a standard mechanical design approach of concept generation, concept evaluation and selection, detailed mechanical design analysis and calculations, and finally manufacture and assembly, with testing addressed in Chapter 8.

4.1.1 Concept generation, evaluation and selection

Two concepts were considered for the design of the gripper, each concept having particular strengths and weaknesses as discussed below.

Concept one

The conceptual design of Concept One is shown in **Figure 4.1**. A DC motor, sandwiched between the plates of the gripper, actuates two arms through a simple gear train allowing the gripper to open and close around the conductor. The simplistic gear train allows the optimisation of the gear ratio to meet specific torque or speed requirements.

A half-pulley profile is attached to the end of each arm, forming a wheel once the gripper is completely closed. A DC motor with gearbox is coupled to one of the half-pulleys allowing the robot to drive along the line, the V-shaped wheel formed by the half-pulleys creating a wedging action on the conductor to increase the traction force. Additionally, the half-pulleys can be coated with a conductive rubber to increase the friction coefficient and maintain electrical continuity.

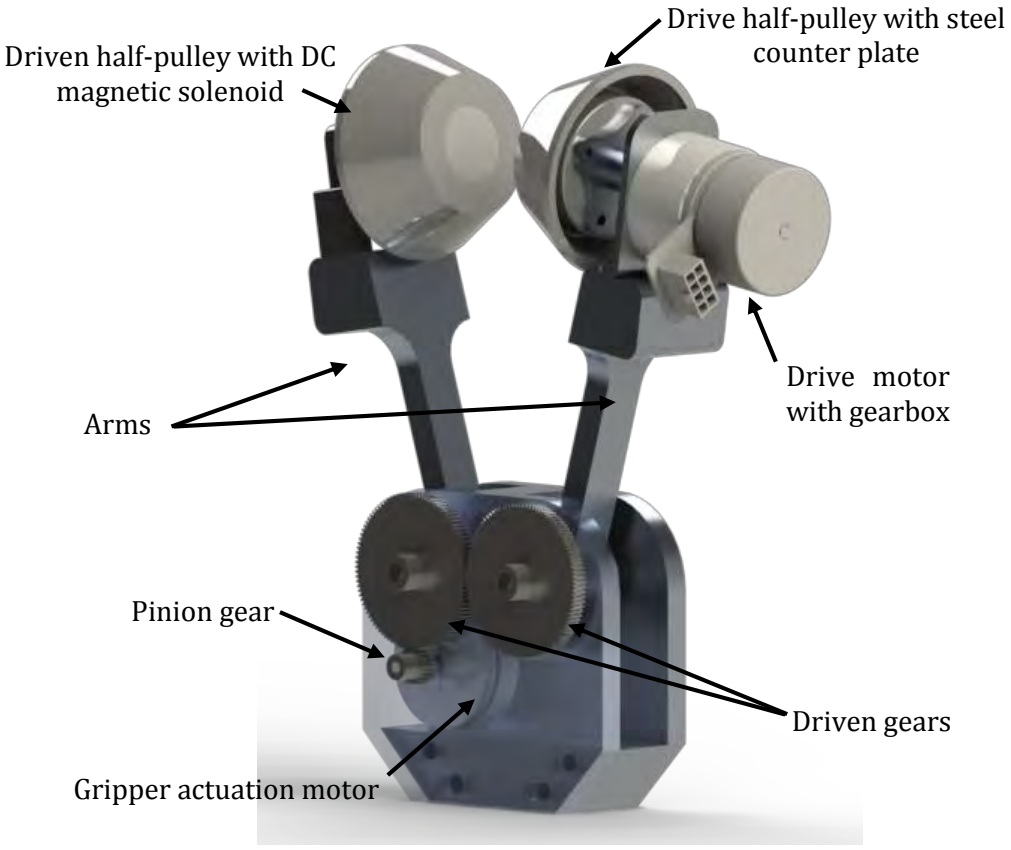

Figure 4.1: Gripper Concept One Solidworks render

The holding torque to keep the gripper closed during operation is provided by a permanent magnetic holding device in one of the half-pulleys and a steel counter plate in the other, seen in **Figure 4.2**. The permanent magnet provides magnetic force greater than the peak dynamic reaction forces during

brachiation and driving, keeping the gripper closed. A DC coil, installed in the magnet, can be energised to counter-act the permanent magnetic field of the solenoid thereby allowing the gripper to open.

Additionally, the magnetic force squeezing the half-pulleys together allows for the transmission of torque from the drive half-pulley to the driven one, thus acting like a magnetic clutch.

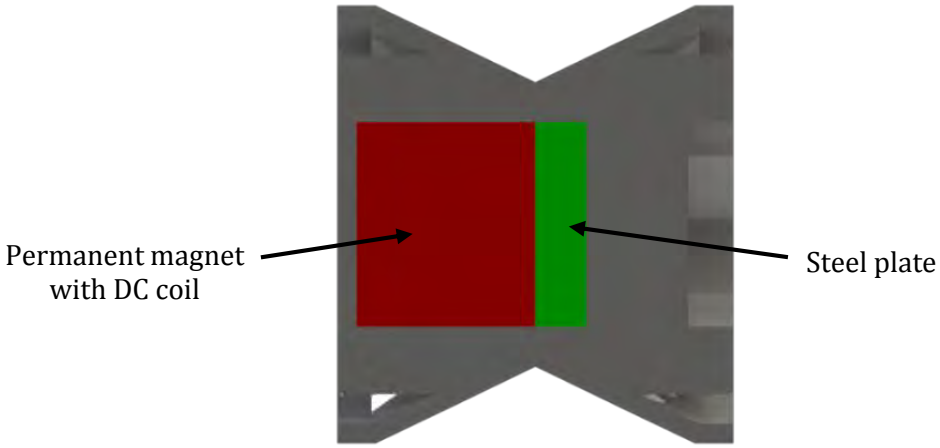

Figure 4.2: Gripper Concept One cross-section of half-pulleys

Concept two

The conceptual design of Concept Two is shown in **Figure 4.3**. The gripper is based on a four-bar mechanism enabling it to close quickly over the conductor while offering increased mechanical advantage due to the linkage design. This mechanical advantage coupled with careful design of the half-pulley shape can be used to make the four-bar mechanism self-closing, under increased weight. Thus making the design energy efficient.

In addition, the flanges on the half-pulleys act as gripping surfaces allowing the gripper to squeeze the conductor thereby anchoring the robot, eliminating the potential for slipping during brachiation. By actively gripping the conductor, the robot can also navigate steep slopes by using an 'inch-worm' manoeuvre, as used in the SkySweeper [13].

A DC motor with gearbox is connected to one of the half-pulleys allowing the robot to drive along the conductor. The half-pulleys can then be coupled using a pair of meshing face gears for additional traction force.

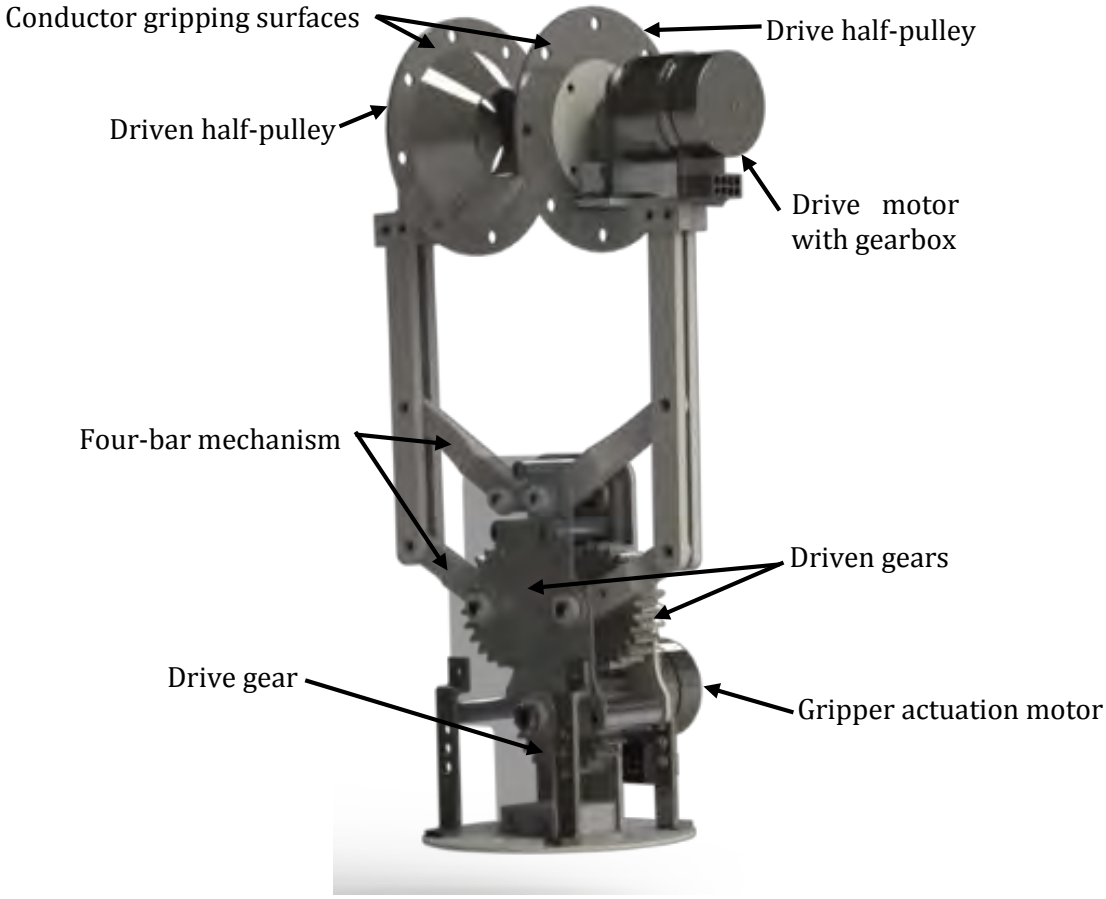

Figure 4.3: Gripper Concept Two Solidworks render

Concept evaluation and selection

The concepts were evaluated in terms of their functionality, the complexity of their design and the ease of manufacture.

The functionality of the grippers are quite similar. However, Concept Two offers the additional functionality of being able to actively grip the conductor instead of relying on the friction between the half-pulleys and the conductor to prevent slipping. This active gripping method is advantageous when brachiating on an incline as the robot will be more secure and less likely to slip. Additionally, being able to grip the line offers the ability for the robot to perform an 'inch-worm' manoeuvre.

Another factor in the functionality of the concepts, is that since the robot will operate on an energised conductor it is unsure how the magnetic field of the conductor will affect the permanent magnetic device installed in the half-pulley of Concept One. The magnet flux density of the conductor can be calculated as

$$Magnetic\ flux\ density,\ B_m = \frac{\mu_0 I_{conductor}}{2\pi r_p} \tag{4.1}$$

where, μ_0 is the permeability of the steel pulley, $I_{conductor}$ is the current in the conductor and r_p is the radius of the pulley. The magnetic flux density is then

$$Magnetic\ flux\ density,\ B_m = \frac{(1.26 \times 10^{-4})(1000)}{2\pi(30 \times 10^{-3})} = 0.7\ \text{T} \tag{4.2}$$

The strength of the magnetic field around the conductor is strong enough to potentially interfere with the permanent magnetic device in the half-pulley of Concept One. Concept Two offers a more reliable solution for resisting the high reaction forces at the gripper and providing an energy efficient method of gripping the conductor for long operations.

Assessing the complexity of the mechanical designs of the concepts, Concept One is the simplest. The arm designs are similar in both concepts, with Concept One only slightly more complex since a slip-ring for electrical connection of the DC coil in the permanent magnet is needed. However, in terms of arm actuation mechanisms, Concept One is far simpler than the complex four-bar mechanism needed in Concept Two.

In terms of ease of manufacture, both concepts will use the same manufacturing methods to fabricate components. Concept Two is slightly more difficult to manufacture due to an increased number of parts required for the design.

The functionality of the concept is the most critical decision factor. Although Concept Two's design is slightly more complex and time-consuming to manufacture, its functionality outweighs Concept One and therefore it was selected for the design of the gripper.

The following section discusses the detailed design of the gripper, followed by the manufacture and assembly, strength analysis and finally Solidworks renders and as-built pictures of the final gripper design.

4.1.2 Detailed design and analysis

An in-depth mechanical design analysis of the gripper was conducted in order to assure the success of the gripper.

Four-bar design synthesis

A typical four-bar mechanism consists of three moving linkages and one stationary linkage as shown in **Figure 4.4**. The crank is usually the input and the coupler the output, with the rocker sometimes called follower linkage used to define and constrain the motion.

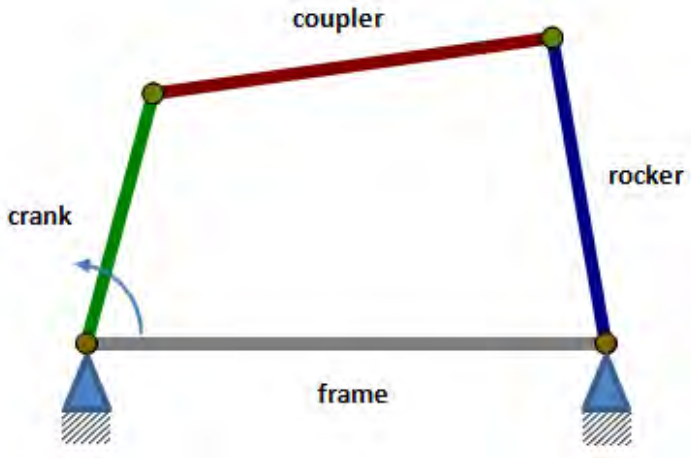

Figure 4.4: Typical four-bar mechanism [47]

The four-bar mechanism for the gripper was designed using a position synthesis technique, described in [48]. A schematic representation of the gripper, showing the gripper arm and the shape of a half-

pulley, is used to evaluate the design of the four-bar mechanism. Initially, only the desired positions of the gripper are known. Three positions, shown in **Figure 4.5**, are selected

- An open position, shown in red, for releasing the conductor at the start of brachiation and for allowing the conductor to pass through at the end of brachiation
- A partially closed position, shown in green, for catching onto the conductor. This position can also be used for driving along the conductor.
- A fully closed position, shown in blue, for gripping onto the conductor to prevent slipping during brachiation or when performing an inch-worm manoeuvre.

Then by using the position synthesis technique, represented graphically in **Figure 4.5**, the linkage lengths and centres of rotation can be determined as follows

- A coupler length was selected. This determines the attachment points of the crank and follower link, labelled as **A** and **B** respectively.
- The crank and follower attachment points were then labelled for subsequent gripper positions as **A**', **A**'' and **B**', **B**'' for the crank and follower respectively. The three attachment points for each linkage represent a circular arc.
- A line connecting the crank attachment points was then drawn, and similarly for the follower attachment points
- Perpendicular lines from the midpoint of the lines connecting the attachments points were then drawn.
- The intersection of these perpendicular lines then represent the pivot points for the follower and crank linkages
- The crank length is then given by the distance from the crank pivot to any crank attachment point, similarly for the follower length.

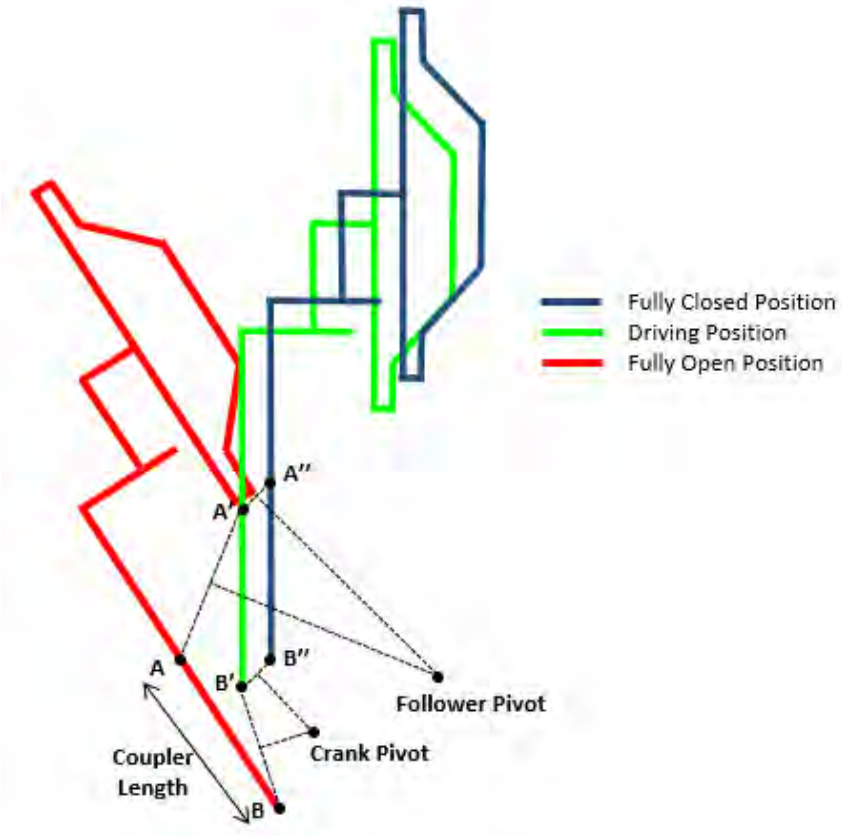

Figure 4.5: Four-bar position design synthesis

Using this technique the four-bar mechanism linkage lengths and pivot points were designed to achieve the desired motion.

In choosing the desired positions for the gripper a number of design factors had to considered.

For the fully open position the distance l_1, shown in **Figure 4.6**, determines the distance through which the conductor must pass. Since the largest conductor that the robot will operate on is a Bull conductor which has a diameter of 38.6 mm, this distance must be at least twice the maximum conductor diameter to account for any misalignment during brachiation.

Further, the distance l_2, defines the centre-centre distance of a meshing gear pair and must therefore satisfy

$$l_2 = \frac{m_{gear}(Z_{gear_1} + Z_{gear_2})}{2} \tag{4.3}$$

where, m_{gear} is the gear tooth module and Z_{gear} is the number of gear teeth. Since the two arms of the gripper must move at the same speed,

$$Z_{gear_1} = Z_{gear_2} \tag{4.4}$$

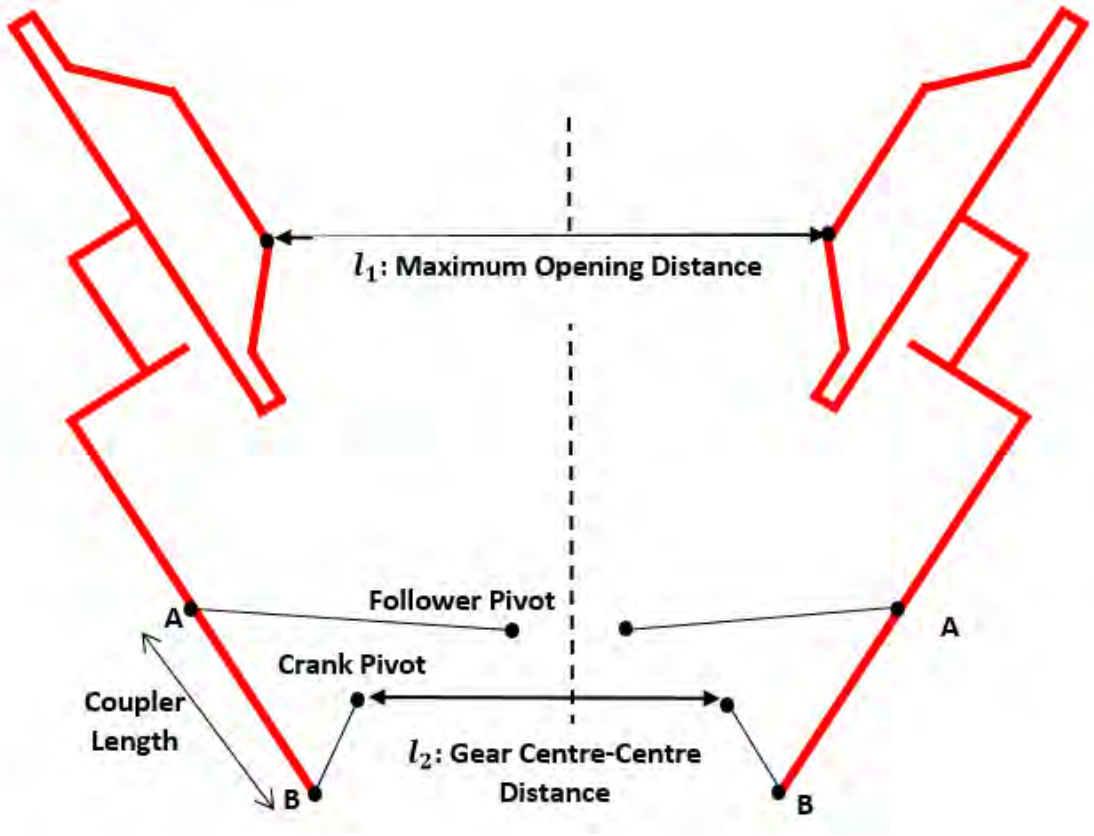

Figure 4.6: Design considerations for fully open position of four-bar mechanism

The final design of the four-bar mechanism along with mechanism specifications are shown in **Figure 4.7** and **Table 4.1**, the half-pulley profiles are omitted from the figure for clarity.

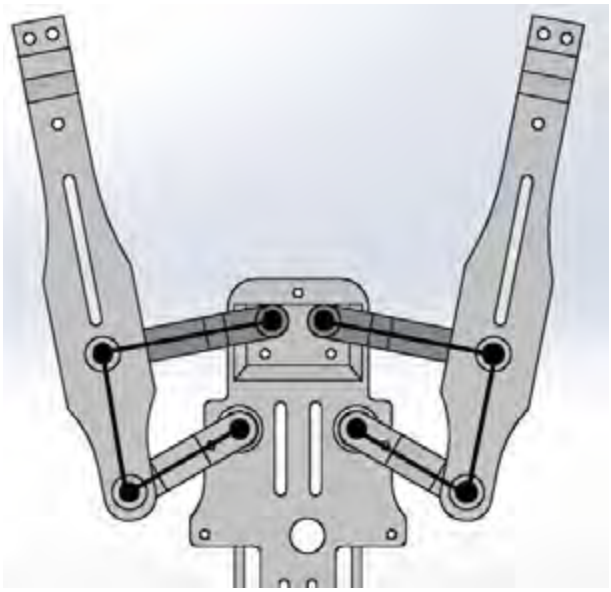

Figure 4.7: Final design of four-bar mechanism

Table 4.1: Final specifications of four-bar mechanism

Specification	Value(mm)
Coupler length	60.00
Crank length	54.27
Follower length	73.57
Maximum opening distance	108
Gear centre-centre distance	50

The gear centre-centre distance is designed to accommodate the gear shown in **Figure 4.8**, which has a module of 1 and 50 teeth. Through gear tooth stress analysis the gear was confirmed to be strong enough to withstand the torque loading during gripper actuation. The calculations for the gear stress analysis can be found in Appendix C.1.

Figure 4.8: Gripper gear

Finally, the maximum opening distance was designed to be three times the diameter of the largest conductor, the Bull conductor, to allow for misalignment during brachiation.

Selection of gripper actuation motor

The gripper actuation motor determines the time it takes for the gripper to rotate from a fully open to a semi-closed position to catch onto a conductor at the end of a brachiation manoeuvre.

In order to determine the minimum closing speed, the time it takes for the robot to fall is analysed as shown in **Figure 4.9**. It is assumed that the robot falls under the influence of gravity alone at the end of the swing, through the distance l before it is unable to catch onto the conductor as it would close below the conductor.

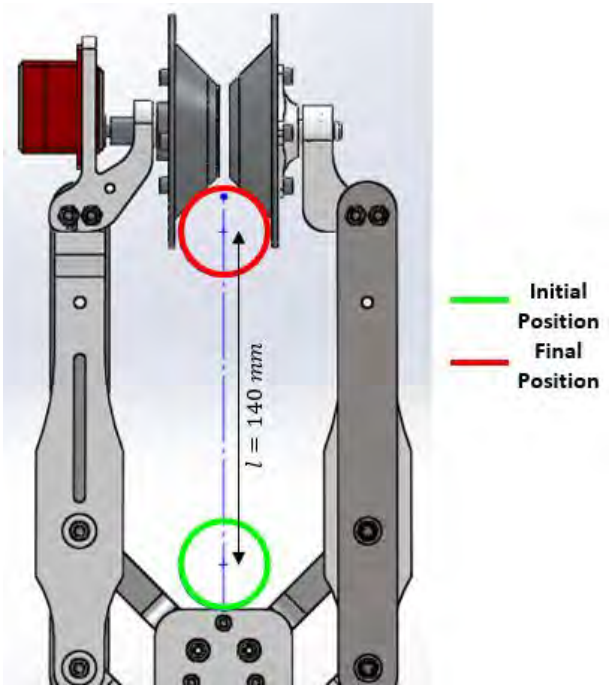

Figure 4.9: Closing speed analysis of four-bar mechanism

The minimum closing time can then be calculated as

$$Maximum\ closing\ time = \sqrt{\frac{2l}{g}} = \sqrt{\frac{2 \times 0.14}{9.81}} = 170\ \text{ms} \tag{4.5}$$

Therefore, the gripper must close in less than 170 ms.

A servo motor was selected as the gripper actuation motor since it offers position control combined with high torque and speed characteristics for relatively low cost when compared to a high quality DC motor, which would require a motor driver and encoder for position control. The servo motor selected for the gripper is shown in **Figure 4.10** along with its specifications in **Table 4.2**.

Figure 4.10: Servo motor for gripper actuation

Table 4.2: RJX-FS0521HV gripper servo specifications

Specification	Value	Units
Voltage	7.4	V
Stall Torque	1.9	Nm
Maximum Speed	181.4	Rpm

The gripper closing speed of the gripper can be analysed by simulating the four-bar mechanism using the model discussed in Chapter 2.6 coupled with the motor model discussed in Chapter 2.4. The time taken for the gripper to close was used to assess the feasibility of the selected servo motor, where the initial and final positions of the gripper are shown in **Figure 4.11**.

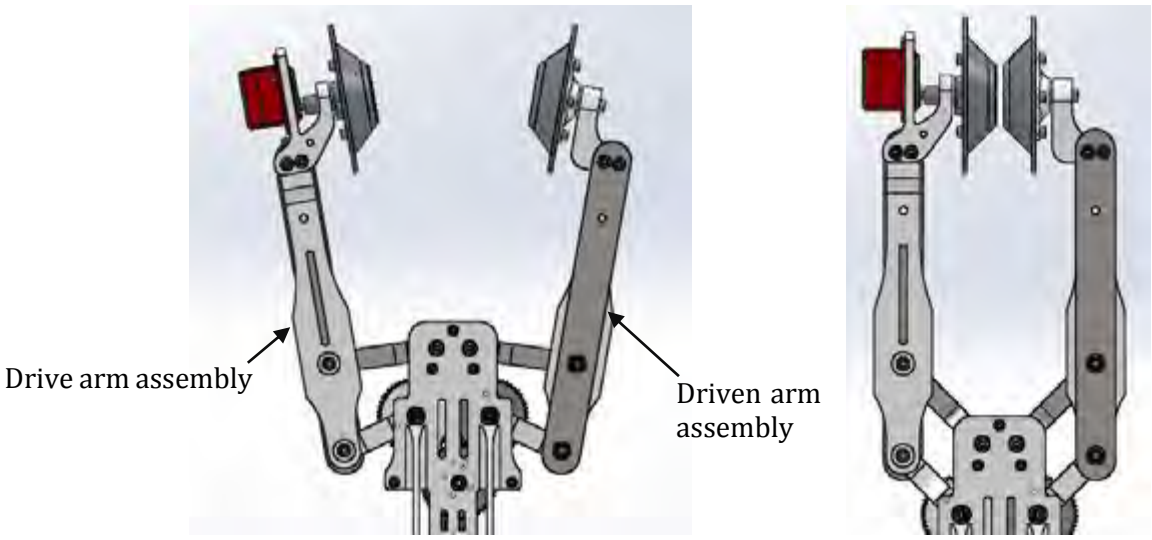

Figure 4.11: Initial and final positions of the gripper during brachiation

In simulating the four-bar mechanism, it was assumed that all the weight of the gripper arm, including the drive and driven pulley assemblies, is concentrated on the coupler link. Additionally, since each gripper arm is connected to a four-bar mechanism, only one four-bar mechanism with the combined weight of both gripper arms is simulated. This assumption is valid since the actuation motor would rotate both arms of the gripper at the same speed and is equivalent to rotating one arm gripper with a combined mass. The masses of the four-bar mechanism links used for the simulation are shown in **Table 4.3**.

Table 4.3: Four-bar link masses for simulation

Specification	Mass(g)
Crank	6.5
Follower	10.8
Driven arm assembly	286.7
Drive arm assembly	360.4
Equivalent crank	13.0
Equivalent follower	21.6
Equivalent coupler	647.1

The gripper arms are actuated through a gear pair. The pinion gear actuates one of the gears connected to a gripper arm, this gear then actuates the other gear through a 1:1 ratio since the arms

must rotate at the same speed. Therefore, the optimal gear ratio of the pinion to gripper arm gear was also analysed. The closing sequence of the gripper is shown in **Figure 4.12**, along with the relation between the closing time and the gear ratio in **Figure 4.13**.

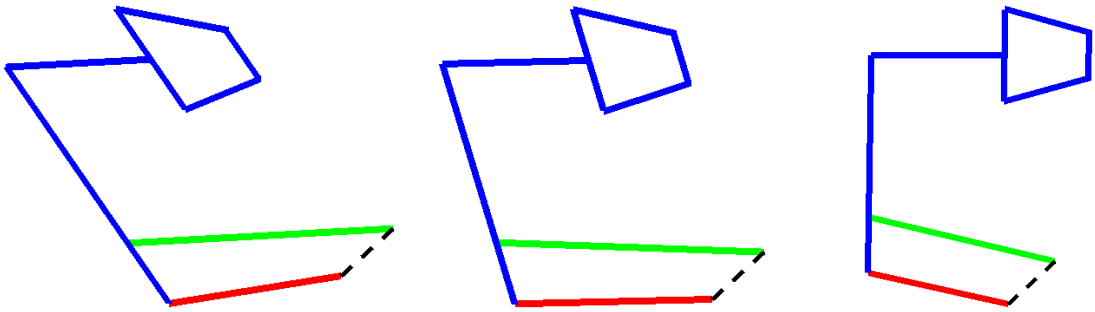

Figure 4.12: Four-bar mechanism closing sequence

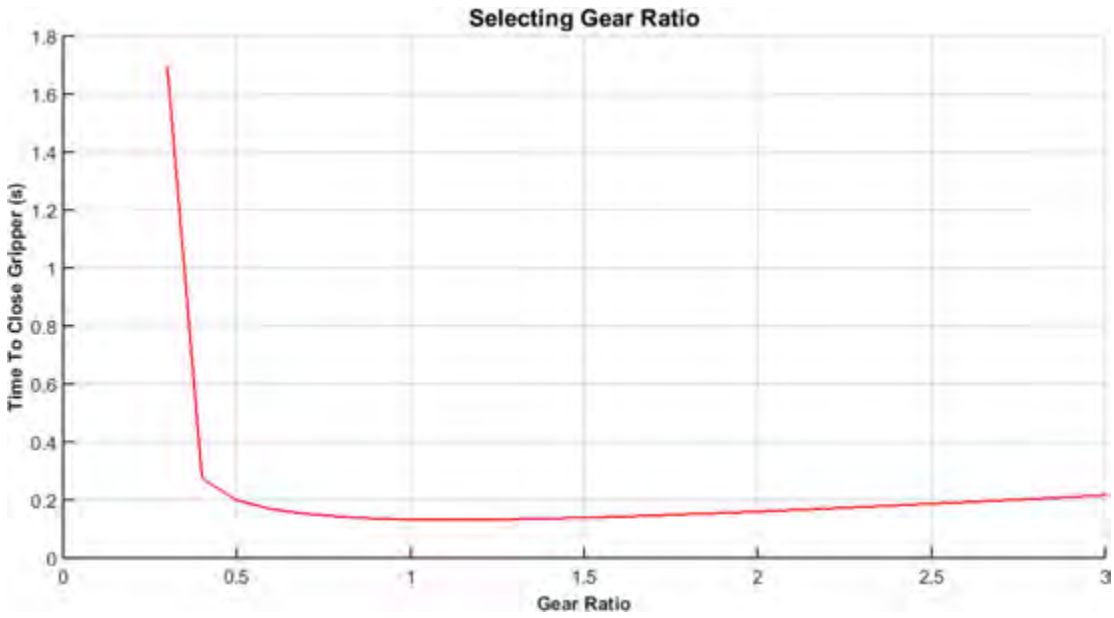

Figure 4.13: Effect of gear ratio on gripper closing speed

From **Figure 4.13**, the optimal gear ratio is between 1.1 – 1.2. Therefore a gear ratio of 1, which results in a closing time of 133 ms, was selected since all the gears would then be identical, minimizing the number of different components.

The closing speed of the gripper is 1.27 times faster than the minimum closing speed and therefore the gripper will be able to close around the conductor fast enough to successfully brachiate.

Pulley angle design

The half-pulleys are shaped to create a wedging action on the conductor to increase traction. The design has an affect on both the gripper actuation motor, and the drive motor specifications. The pulley angle, shown in **Figure 4.14**, is the design variable which has the most influence on the shape of the pulley.

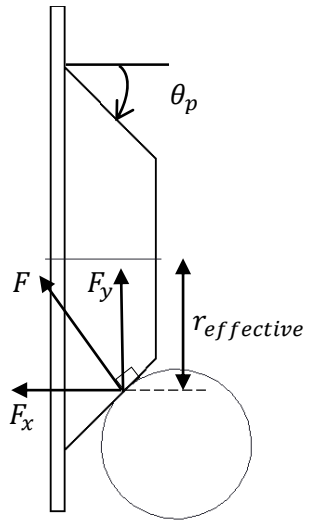

Figure 4.14: Pulley angle effect on reaction forces

Where, θ_p is the pulley angle, F is the orthogonal reaction force and F_x and F_y are the horizontal and vertical components of the orthogonal reaction force respectively, and $r_{effective}$ is the effective radius.

The pulley angle controls the relationship between the horizontal and vertical reaction forces at the point of contact with the conductor as shown in **Figure 4.14**.

The reaction forces can be calculated as

$$F_x = F \sin \theta_p \tag{4.6}$$

$$F_y = F \cos \theta_p \tag{4.7}$$

Therefore, by changing the pulley angle the ratio between the horizontal and vertical reaction components can be adjusted. This affects the reaction force on the gripper mechanism which in turn affects the holding torque of the gripper actuation motor to keep the mechanism closed.

The pulley angle also controls the effective diameter of the pulley, which is the diameter at which the pulley contacts the conductor, as shown in **Figure 4.14**. This diameter affects the speed and torque requirements of the drive motor.

Through design analysis, balancing both the geometry of the pulley and specifications of the motors a pulley angle of $45°$ was selected. This results in equivalent vertical and horizontal reaction force components and an effective diameter of 61 mm.

Selection of driving motor

The drive motors of the robot allow the robot to drive along the line which is more energy efficient than constant brachiation. The requirements for the drive motor are that the robot be capable of

- Driving at 1 m/s along a horizontal conductor
- Driving up an inclined conductor with a maximum slope of $30°$

In order to determine the speed and torque requirements for the drive motor, the half-pulley was modelled as a wheel with external forces as shown in **Figure 4.15**.

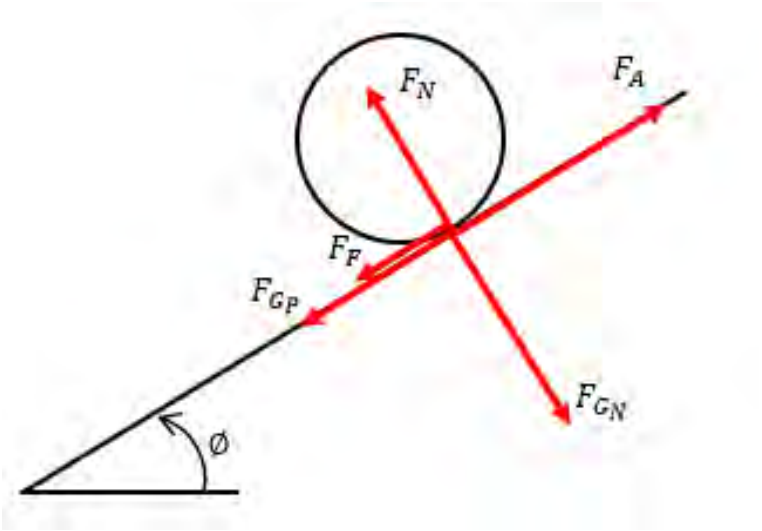

Figure 4.15: Half-pulley modelling to determine required motor specifications

Where, F_{G_N} and F_{G_P} are the normal and parallel components of the gravitational force, F_N is the normal reaction force, F_F is the frictional force, F_A is the applied force and Ø is the slope angle.

The drive motor requirements are summarised below in **Table 4.4**. The detailed calculations of the drive motor requirements can be found in Appendix C.2.

Table 4.4: Drive motor requirements

Scenario	Specification	Value	Units
0° conductor	Required torque per half-pulley pair	0.07	Nm
	Required wheel speed	313	Rpm
30° conductor	Required torque per half-pulley pair	0.52	Nm
	Required wheel speed	157	Rpm

Based on the above specifications a motor was selected to meet the requirements. Since the robot developed in this project is a prototype, a servo motor was selected and modified, converting it into a continuous rotation motor, as described in [49]. The servo motor provides a cost-effective solution since it already includes a gearbox and power electronics necessary for driving. The servo motor selected for the gripper is shown in **Figure 4.16** along with its specifications in **Table 4.5**.

Figure 4.16: Servo motor for driving

Table 4.5: RJX-FS0521THV gripper servo specifications

Specification	Value	Units
Voltage	7.4	V
Stall Torque	0.94	Nm
Maximum Speed	313	Rpm

Finite element analysis of critical components

The gripper serves as the only point of contact with the conductor during brachiation. Therefore, the mechanical strength of the gripper plays a key part in the success of the robot.

In order to assess the mechanical strength of the individual gripper components, finite element analysis using Solidworks Simulation was undertaken. This analysis allowed for the optimisation of the gripper components' strength-to-weight ratio.

The gripper parts were manufactured using a FDM 3D printer, as discussed in Chapter 4.1.3, with either ABS or PLA material being used, depending on the printer. The yield strength of ABS and PLA is approximately 44 MPa and 58 MPa [50], respectively. However, as discussed in Chapter 4.1.3, the strength of the printed parts is largely dependent on the print orientation [51, 52] and is weaker in the layered direction, the direction which the part is built, usually the Z-axis. Therefore, a yield strength of 22 MPa, half the yield strength of ABS, was chosen since this allowed the gripper parts to be printed on any 3D printer and in any orientation.

The peak gripper reaction forces during brachiation, obtained in Chapter 3, were used to analyse the strength of the components. Since the robot is tested in a controlled laboratory environment and the gripper serves as a prototype, the gripper components were designed with a yield strength safety factor of 1.1. Using a low safety factor allowed for the minimization of the gripper weight and testing of functionality, albeit with the risk of component failure. The final version of the robot would require a higher safety since the risks associated with failure would be greater.

The strength and displacement analysis of a gripper component is shown in **Figure 4.17** as an illustration of the FEA results. The detailed calculations behind the FEA analysis can be found in Appendix C.3.

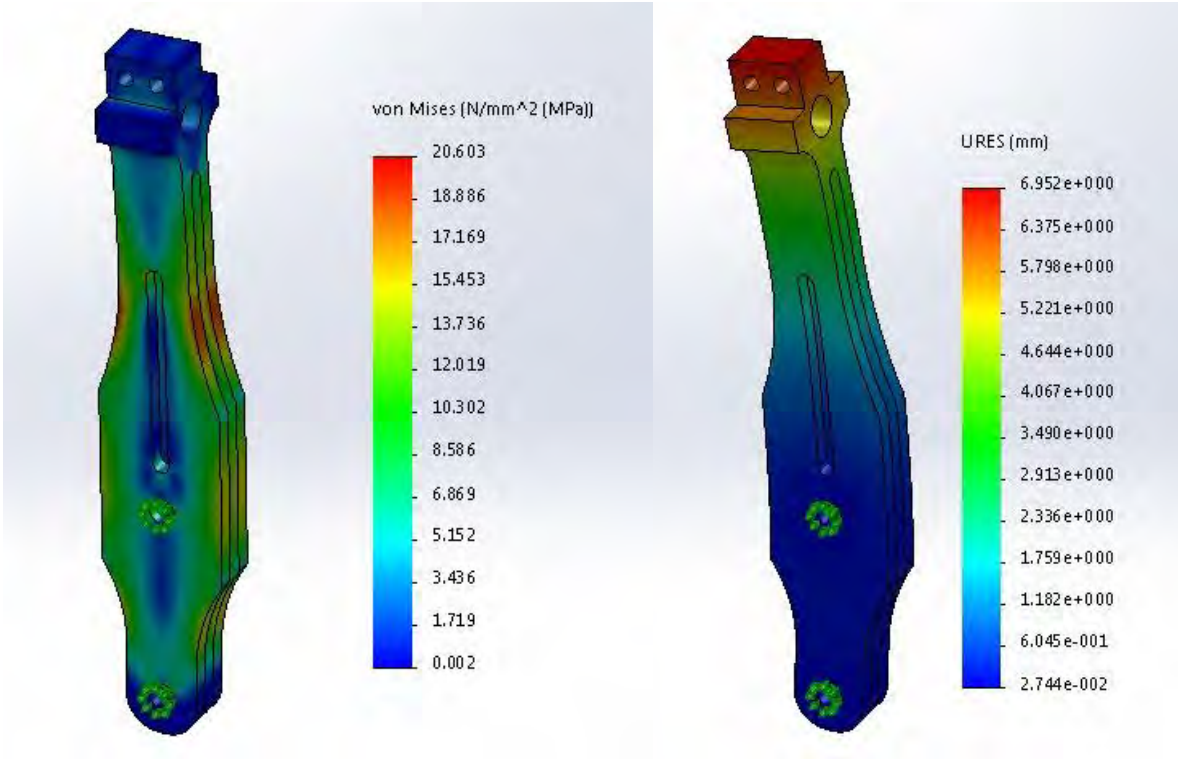

Figure 4.17: FEA analysis of gripper arm under jumper-to-main conductor brachiation conditions

Further, the FEA analysis can be expanded to include assemblies as shown in **Figure 4.18**. This was extremely useful since analysing the structure as a whole, results in a better understanding of its strength compared to analysing its individual components.

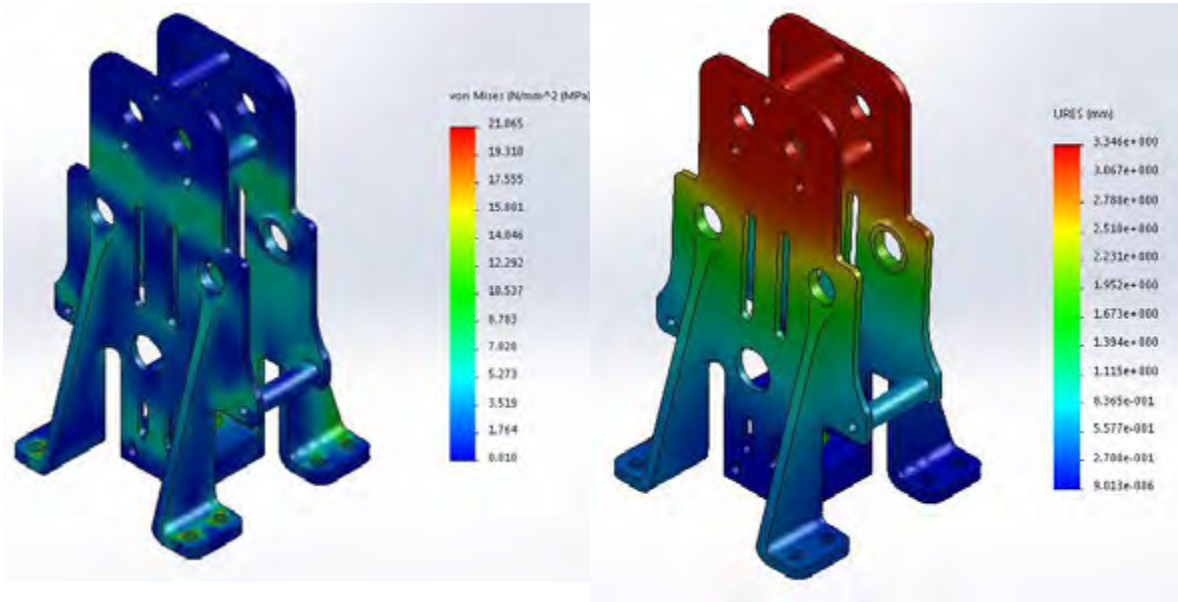

Figure 4.18: FEA analysis of gripper assembly under jumper-to-main conductor brachiation conditions

4.1.3 Manufacture and assembly

The gripper was designed for ease of manufacture and assembly with components forming sub-assemblies that can quickly be put together to complete the gripper.

Initially the gripper was designed using metals, mainly aluminium due its high strength-to-weight ratio, and was to be manufactured using traditional subtractive manufacturing techniques such as CNC milling. However, since the gripper in this project serves as a prototype and was focused on developing functionality as opposed to industrial reliability, it was decided to 3D print the gripper. An industrial version of the gripper would be made from aluminium, with steel being used for parts requiring high strength.

The gripper components were 3D printed using an Ultimaker 2+, shown in **Figure 4.19**. The advantages and disadvantages of the 3D printing manufacturing technique are summarised in **Table 4.6**.

Table 4.6: 3D printing analysis

Strengths	Weaknesses
• Faster and cheaper than traditional subtractive manufacturing techniques • Allows for relatively quick prototyping • Complex part geometry and internal features	• Poor tolerances on parts, especially holes • Low mechanical strength and stiffness mainly due to using plastic • Lower mechanical strength in the layered axis

Figure 4.19: Ultimaker 2+ [53]

The printer is capable of using both ABS and PLA filament, which are both types of plastic. The final quality and strength of the component is influenced heavily by four design factors

- Material choice. Parts printed in PLA usually have a higher stiffness than ABS parts but are more brittle and therefore worse in shock loading.
- Layer height. 3D printed parts are produced by an FDM process which builds the part layer by layer. Decreasing the layer height increases the strength of the bonding between layers creating a stronger part.
- Build orientation. The direction in which the part is built plays a significant role on its strength. By changing the orientation of the part, the strength of the part can be adjusted to best match its loading conditions.

- Infill. The infill is the amount of material inside the part, usually the parts have a honeycomb structure inside to save material. By increasing the infill ratio the parts strength increases, but only up to about 80% infill, at this point the extra material has a low effect on the parts strength.

4.1.4 Final gripper design

The final design of the gripper is shown in **Figure 4.20** along with an as-built picture in **Figure 4.21**. A mechanical stop to prevent over-centre rotation of the four-bar mechanism is incorporated, as well as steel bracing straps to the gripper arms for added stiffness. The servo's are both shown in red for clarity.

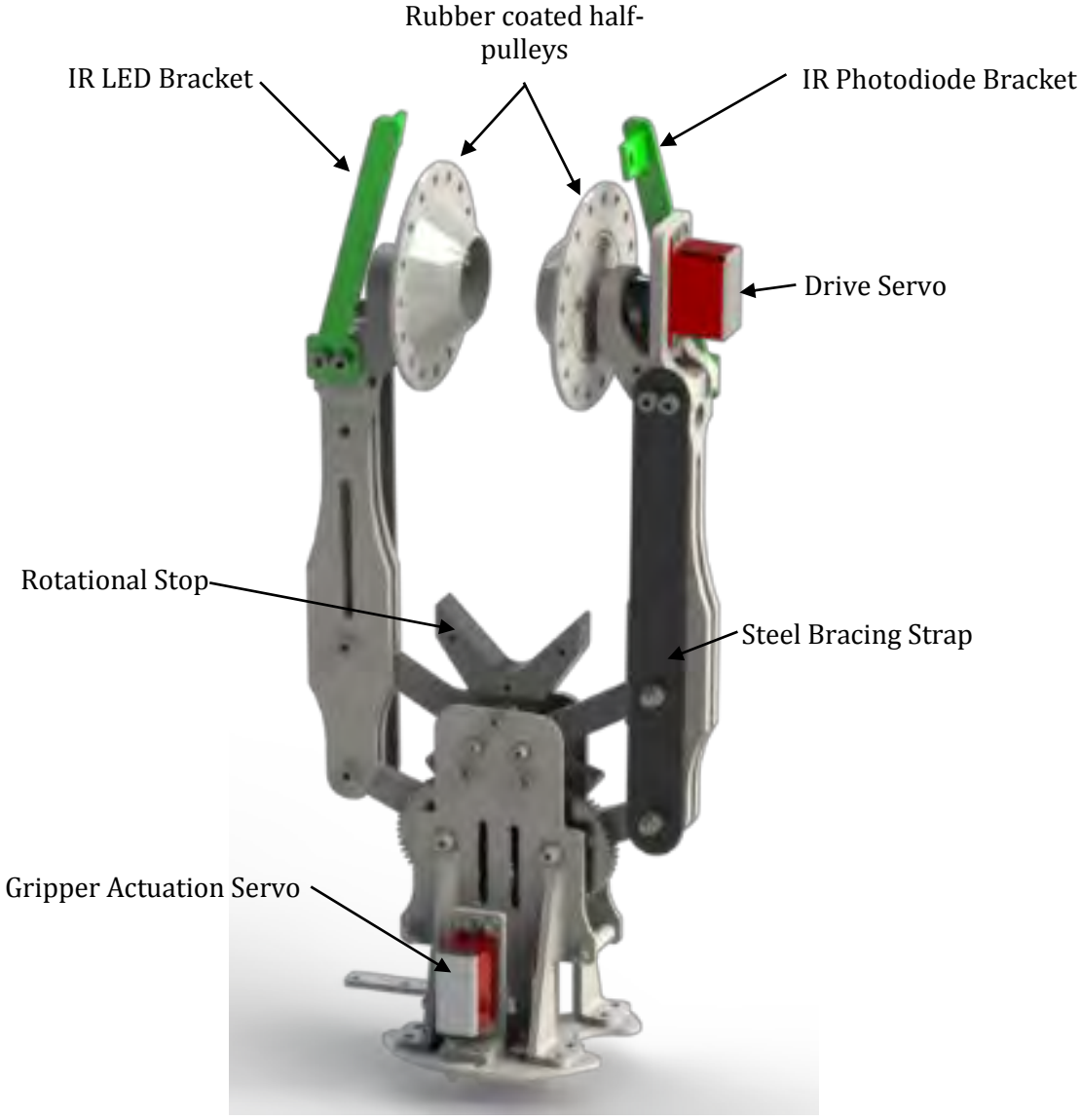

Figure 4.20: Solidworks render of final gripper design, front plate hidden

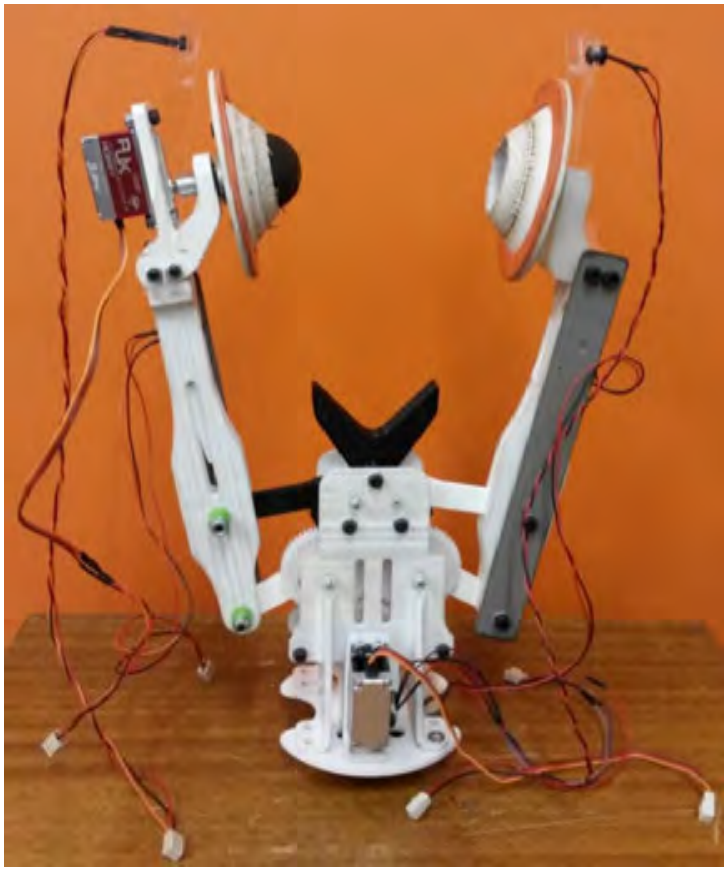

Figure 4.21: Gripper as-built

Due to time and cost constraints, only one gripper was built. A replacement gripper, shown in **Figure 4.22**, was designed and built to replicate a stationary gripper during brachiation. Therefore the robot was still able to brachiate, although only one phase of the brachiation was possible.

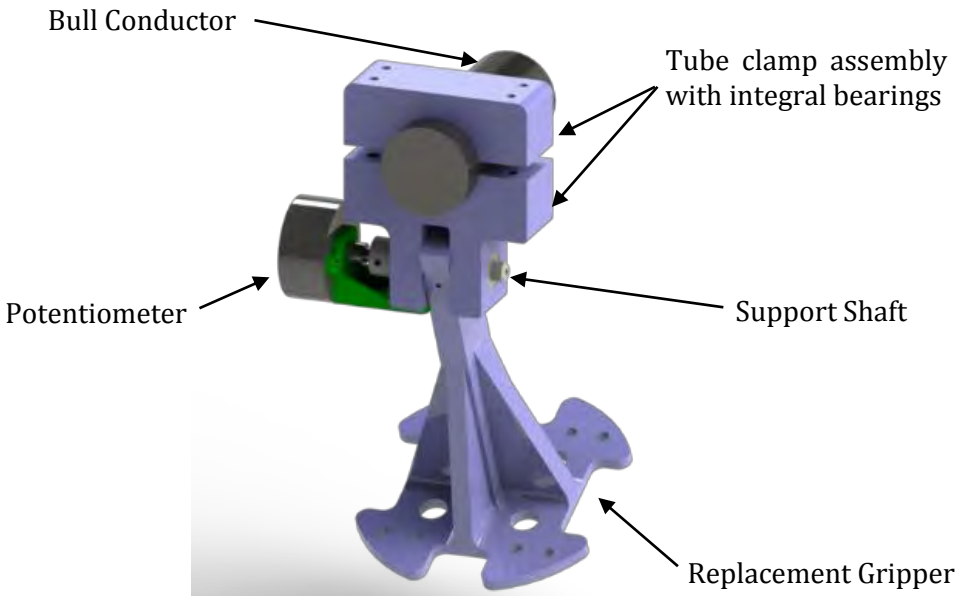

Figure 4.22: Solidworks render of replacement gripper

4.2 Link actuation mechanism

The robot developed in this project is underactuated, using a single actuator to control the trajectory of the links. Therefore, the way in which the links are actuated is critical to the success of the robot.

The link actuation mechanism was selected based on an evaluation of possible actuation methods. Following this, detailed calculations of the linkage design were conducted to ensure the mechanical robustness of the design.

4.2.1 Analysis of linkage actuation mechanisms

Two mechanisms were considered for the design of the linkage actuation mechanism, each mechanism having particular strengths and weaknesses as discussed below.

Elastic Actuation

Elastic actuators are characterised by their use of an elastic element, usually a linear or torsional spring, in parallel or series between the gearbox output and the load, as shown in **Figure 4.23**.

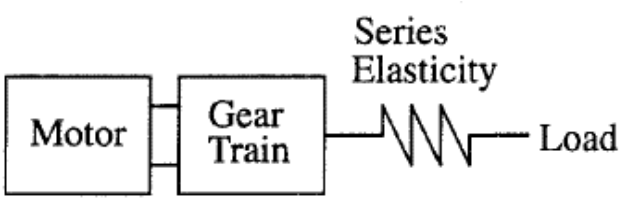

Figure 4.23: Schematic diagram of a series elastic actuator [54]

This decoupling of the motor inertia from the loads inertia allows for the design of a compliant joint, especially useful in situations where robots interact with the environment as the compliant nature of the actuators reduce damage caused by collisions. Force control applications are another area where elastic actuators are desirable, since the force can be controlled precisely by controlling the deflection of the elastic element as in [55] [56]. The actuator designs of a series elastic and parallel elastic actuator are shown in **Figure 4.24**.

Elastic actuators also offer the potential for energy storage, thus they can reduce the required power of the system, this can be seen in the SkySweeper [13]. By using a series elastic actuator the SkySweeper is able to increase the energy of the system, by deflecting the spring, while the system is stationary and once the gripper releases the line that energy is then released into the system.

Further, in [57], a clutched parallel actuator is developed. Normally, the energy stored by the elastic actuator is released when the motor driving the spring is turned off, but by having a clutched elastic actuator the energy can be released into the system at any point. The clutched parallel elastic actuator developed in [57] is shown in **Figure 4.25**.

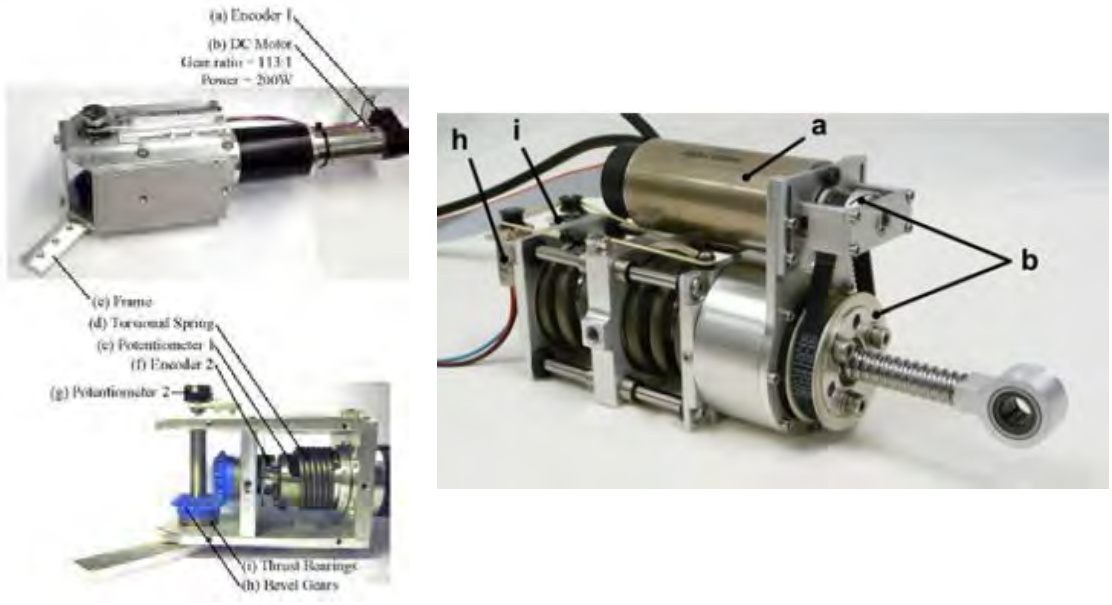

Figure 4.24: Elastic actuators. Left, series elastic actuator [55]. Right, parallel elastic actuator [56]

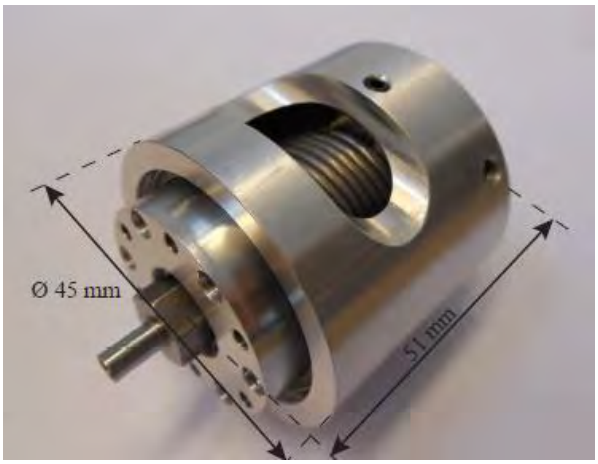

Figure 4.25: Clutched parallel elastic actuator [57]

Direct actuation

The simplest method of actuation is direct actuation, where the output shaft of the actuator is connected directly to one of the robot links.

By directly connecting the output shaft to the robots' link, the control of the robot's trajectory becomes easier since the actuated link can be controlled by measuring the position on the motor output shaft, usually through an encoder.

A special case of direct actuation is seen in [18], where two DC motors are coupled and collectively actuate one of the robot links, as shown in **Figure 4.26**. This coupling doubles the rotational speed of the motor and provides a symmetric weight balance. However, the design has issues with weight and commutation synchronization issues [56].

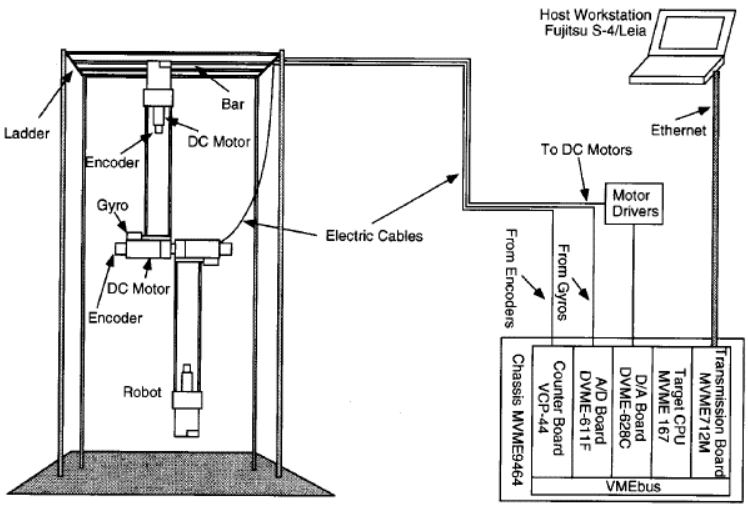

Figure 4.26: Coupled DC motors actuating robot link [18]

Direct actuation has been implemented in a number of successful brachiation research efforts [18, 58, 59].

Evaluation and selection of actuation mechanism

The actuator mechanism was selected based on power requirements, mechanical simplicity and robustness, and required control complexity.

The energy required for brachiation is equivalent in all actuation mechanisms. However, the power requirement of the actuator varies significantly. The elastic actuator mechanism is capable of increasing the energy of the system while the system is stationary whereas in direct actuation the energy required for brachiation must be inserted while brachiating, resulting in a high power requirement.

In terms of mechanical simplicity and robustness, direct actuation offers the best solution since there are less mechanical parts and the design is simple, increasing the reliability of the robot, which is key to its success.

The control of the elastic actuator is more complex than direct actuation since the elastic elements deflection must be measured to accurately control the output torque. Further, the elastic elements' generated torque is only linear in a small deflection region as shown in **Figure 4.27**.

Since this project is focused on developing a prototype as a proof of concept, the mechanical simplicity and robustness was deemed the most critical decision factor. Therefore, direct actuation was selected for the link actuation mechanism. An industrial version of the robot, developed at a later stage, could focus on exploiting the advantages of elastic actuation.

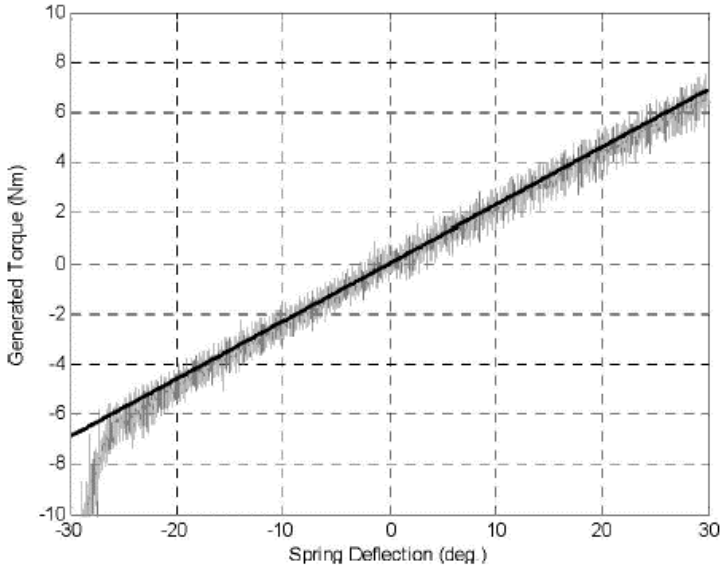

Figure 4.27: Non-linear generated torque of spring [55]

4.2.2 Detailed linkage design

An in-depth mechanical design analysis of the link mechanism was conducted in order to assure the success of the robot.

Linkage length design

The robot must be capable of brachiating across obstacles on the conductor and therefore the length of its links are an important design variable.

The longest obstacle the robot will encounter is a vibration damper and was therefore the best obstacle to base the robot's link length on. A range of vibration dampers and their associated specifications is shown in **Figure 4.28** and **Table 4.7**.

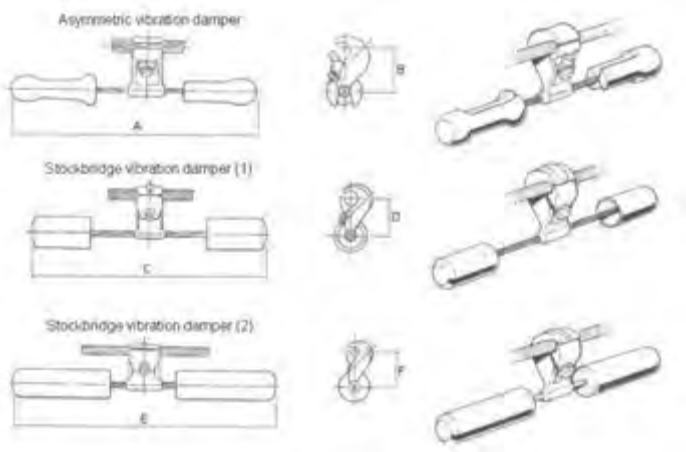

Figure 4.28: Range of possible vibration dampers on conductor [60]

Table 4.7: Vibration damper specifications. Adapted from [60]

Vibration Damper Type	Dimension	Minimum (mm)	Maximum (mm)
Asymmetric	A	411	566
	B	78	100
Stockbridge (1)	C	290	590
	D	48	100
Stockbridge (2)	E	439	673
	F	78	99

The longest obstacle the robot would encounter is therefore a type 2 Stockbridge vibration damper. In order to calculate the required length of the robot, the initial pose of the robot was examined as shown in **Figure 4.29**.

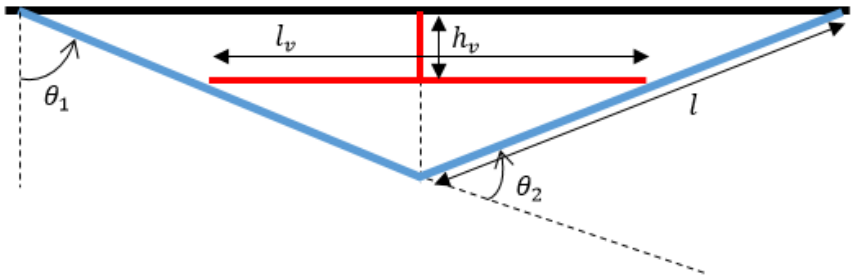

Figure 4.29: Link length calculation diagram

The optimal initial pose for the second phase of the brachiation manoeuvre is one where the COM is as high as possible thereby maximising the potential energy of the system which then can be traded for kinetic energy through the swing, ending in a pose with lower potential energy. Therefore, the link length was calculated using **Figure 4.29** as

$$Link\ length = \frac{l_v}{2\cos(90 - \theta_1)} + \frac{h_v}{\sin(90 - \theta_1)} \tag{4.8}$$

where the values are

Table 4.8: Link length calculation values

Specification	Value	Units
l_v	673	mm
h_v	99	mm
θ_1	80	°

The link length then equals 912 mm. A tolerance of 10% was added to this value to ensure the robot is not in contact with the vibration damper. The final link length was then selected as 1 m for each link.

Finite element analysis of linkage mechanism

The linkage actuation mechanism along with the robot's links form the structure of the robot to which the grippers and payload are attached. The mechanical strength of the structure is key to successful brachiation.

As in Chapter 4.1.2, the mechanical structure of the robot was analysed using FEA in Solidworks. The structure of the robot was manufactured from aluminium 6082-T6 since it provides a high-strength-to-weight ratio. The aluminium has a yield strength of 240 MPa and an ultimate tensile strength of 295 MPa [61], it does however have a finite endurance limit meaning that it cannot undergo cyclic loading conditions indefinitely.

The fatigue strength of aluminium, the strength below which it can undergo cyclic loading up to 5×10^8 cycles, is approximately 0.35 times its ultimate tensile strength [62]. Therefore the robot structure was designed such that the maximum stress was less than 103 MPa.

The stress and displacement analysis of one of the linkage mechanism components is shown in **Figure 4.30** for reference. Detailed calculations and the FEA of the other components can be found in Appendix C.3.

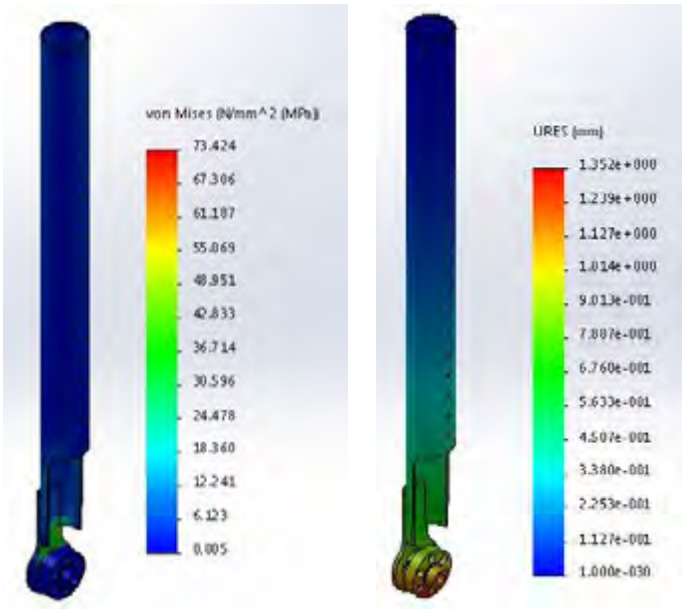

Figure 4.30: FEA analysis of linkage mechanism assembly under jumper-to-main conductor brachiation conditions

4.2.3 Final design of linkage mechanism

The final design of the robot structure along with the linkage actuation mechanism is shown in **Figure 4.31**. The links feature cut-outs at the bottom, near the link actuation mechanism, to increase the rotational freedom between them. The final design is both light-weight and mechanically robust. Additionally, the modular design allows for quick assembly and disassembly.

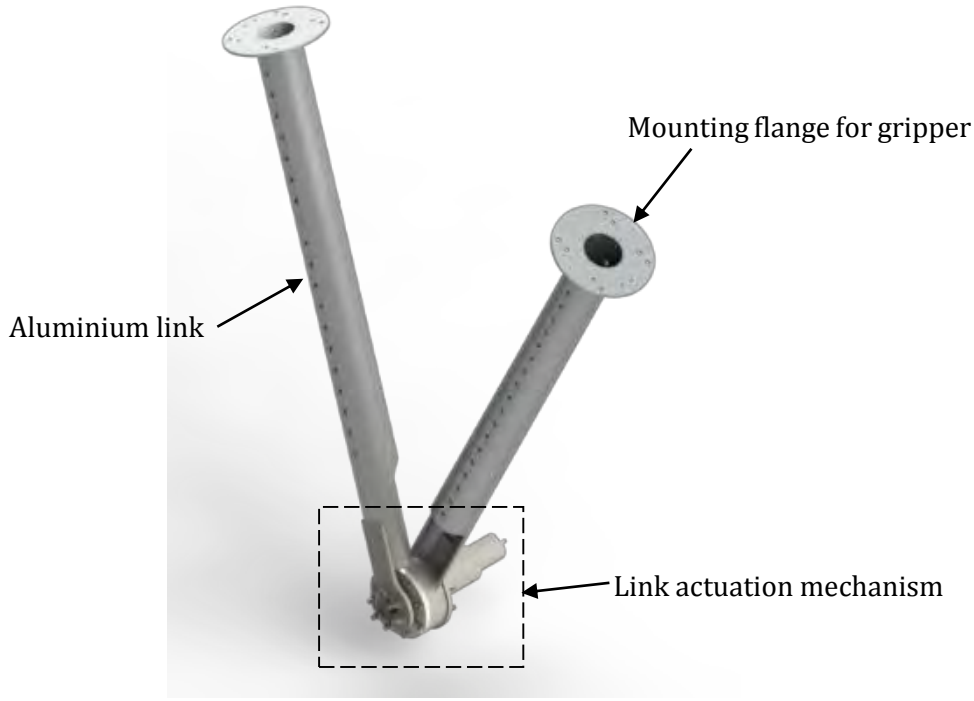

Figure 4.31: Solidworks render of robot structure

A cross-section view of the link actuation mechanism is shown below in **Figure 4.32**. The link assemblies, Link 1 and Link 2 assembly, slide into each other and are tightened together by the removable vesconite half-rings, thus completing the linkage mechanism, as shown in **Figure 4.33**.

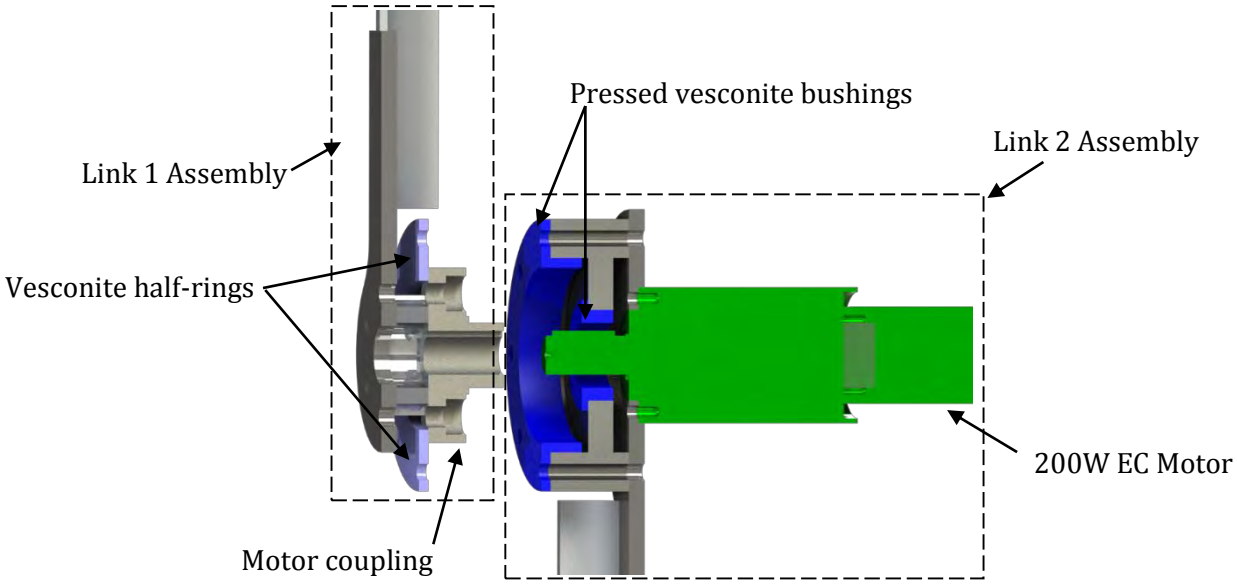

Figure 4.32: Detailed cross-section view of link actuation mechanism

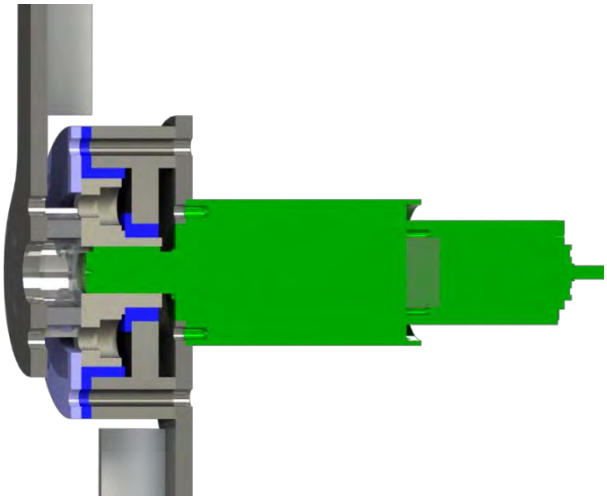

Figure 4.33: Cross-section view of complete linkage mechanism

4.3 Final Robot Design

The final design of the robot is shown in **Figure 4.34**. The robot has one gripper with the other gripper being a replacement gripper, as discussed in Chapter 4.1.2. IMU's are mounted on each link at the corresponding COM position, identified using the Solidworks model, to measure the pose of the robot. The electronics, discussed in Chapter 5, are mounted on Link 1, resulting in an uneven weight balance between the two links, however once the robot's payload such as an inspection camera is mounted to Link 2 in future iterations, the weight balance will be symmetrical.

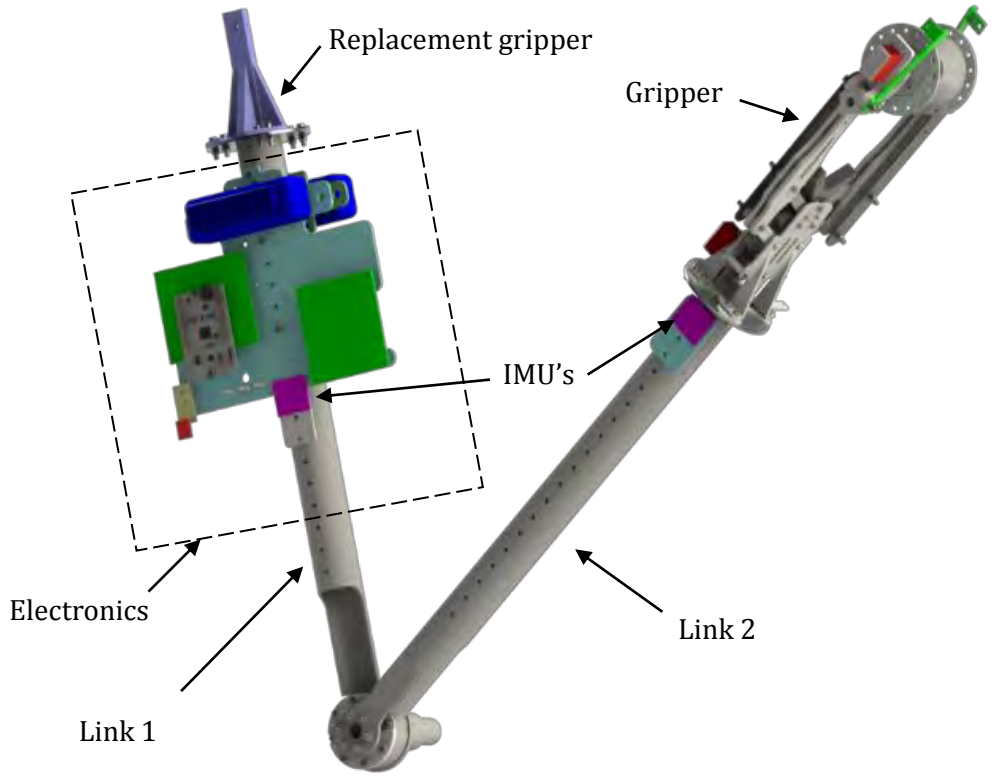

Figure 4.34: Final design of robot

Chapter 5

Electrical and software design

The electrical hardware and software design is presented in this chapter. The aim is to give the reader an idea of the key elements of the electrical design responsible for controlling the robot.

A high-level overview of the electrical design architecture is shown in **Figure 5.1**. A central microprocessor (STM32F4) interfaces to multiple actuators and sensors to allow the robot to both sense its environment and actuate within it.

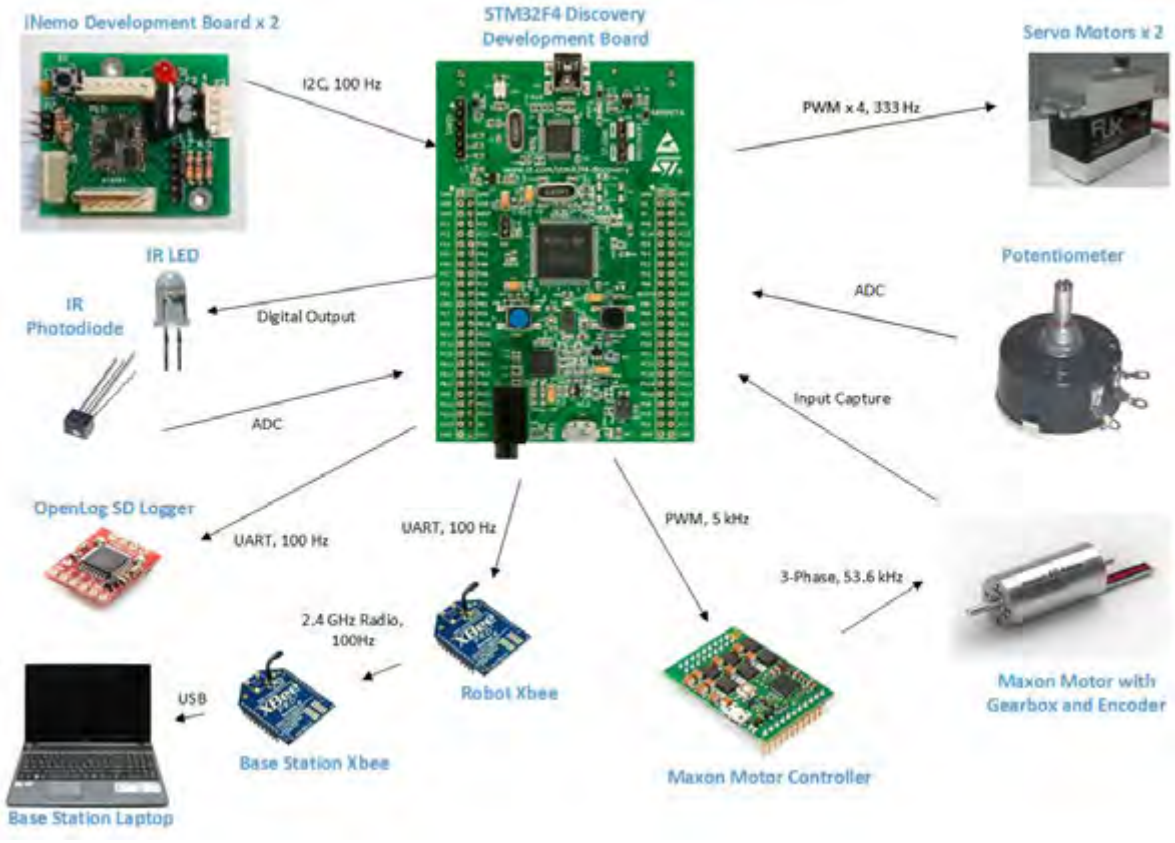

Figure 5.1: Electrical design architecture [44, 46, 63, 64, 65, 66, 67, 68, 69, 70]

The following sub-sections discuss the functions of the individual components and their role in controlling the robot.

5.1 Attitude estimation

The iNemo development board, shown in **Figure 5.2**, was obtained from a concurrent MSc. Project [63] where it was used in an inertial sensor network.

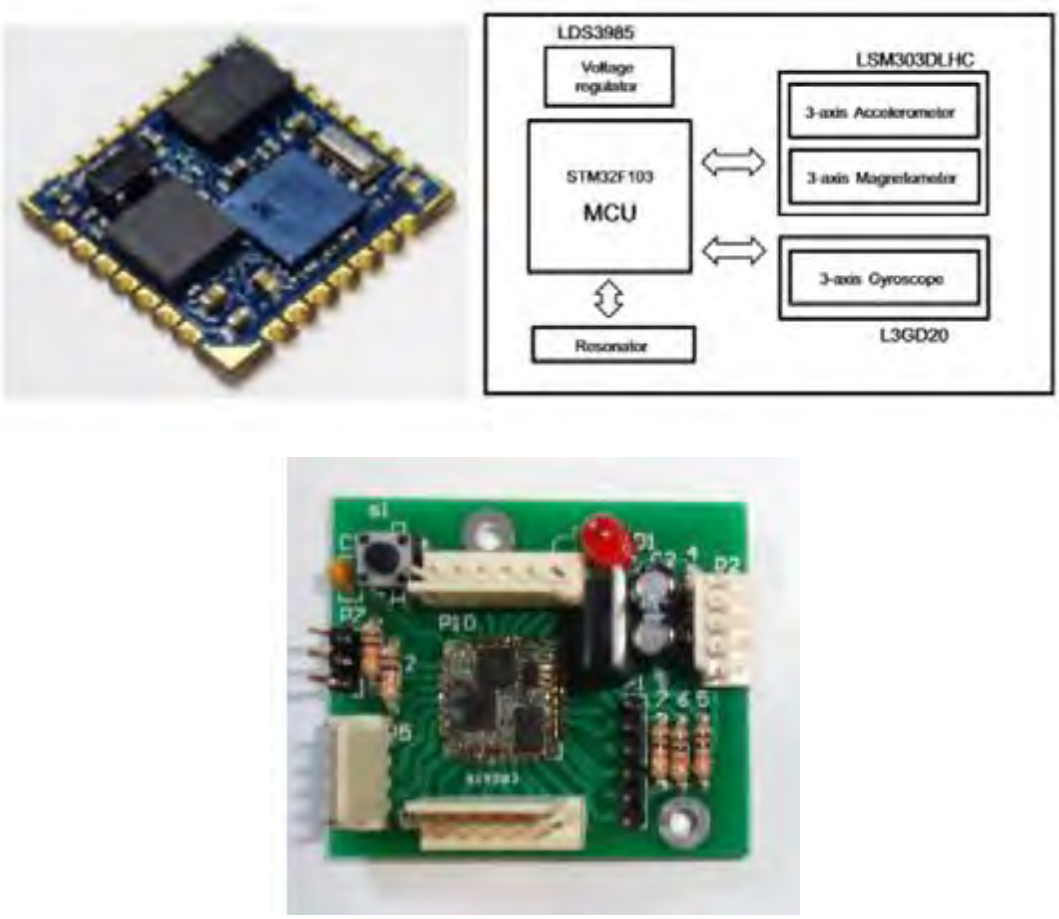

Figure 5.2: iNemo Development Board [63]

The development board consists of 9-axis IMU, which includes a 3-axis gyroscope, 3-axis magnetometer and a 3-axis accelerometer. Additionally, a temperature sensor, an ARM Cortex M3 microcontroller and a voltage regulator are included to allow the board to be deployed as a stand-alone inertial module.

An iNemo board was mounted on each link of the robot at the COM position, obtained from the Solidworks model, to estimate the attitude of the robot using an Extended Kalman Filter algorithm.

The iNemo calibration and setup, basic overview of the EKF algorithm and reference attitude using a motor encoder and potentiometer are discussed below.

5.1.1 iNemo calibration and setup

The sensors on the iNemo boards first needed to be calibrated before they could be used in the EKF algorithm. This calibration removes any static biases and co-axis coupling resulting from sensor axes not being perfectly perpendicular.

Accelerometer calibration

The accelerometer was calibrated using a static calibration method and a 12 parameter calibration algorithm, detailed in [63]. The sensor was placed in six positions, using a gimbal-type structure as shown in **Figure 5.3** . The six positions represent the positive and negative gravity in each of the axes.

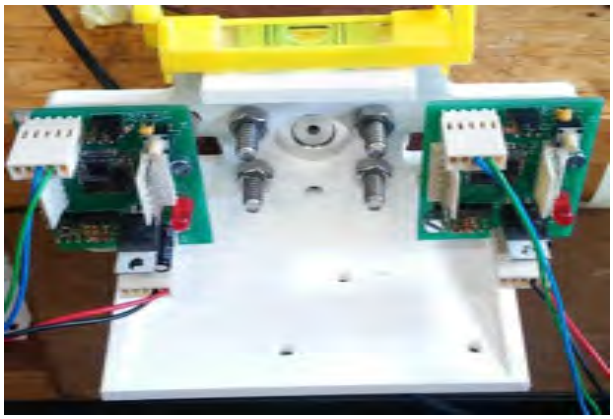

Figure 5.3: Calibration of iNemo boards

The data was logged for 1 minute in each position and then using the calibration algorithm, a calibration matrix which can be applied to the raw sensor data was obtained.

Gyroscope calibration

The gyroscope was calibrated using a static calibration method, detailed in [63]. The sensor was left stationary for 10 minutes while the angular rates and temperature were logged. A heat gun and fan were used to vary the temperature of the sensor so that a wider range of temperatures were calibrated for. **Figure 5.4** shows the angular rate measurement of one of the axes as a function of temperature.

The temperature dependent gyroscope bias of each axis was found by fitting a straight line to the data. The axis-intercept of the line is the zero degree Celsius bias and the slope is the gradient of the temperature dependence. The bias can then be calculated and subtracted from the measured gyroscope value to correct for temperature.

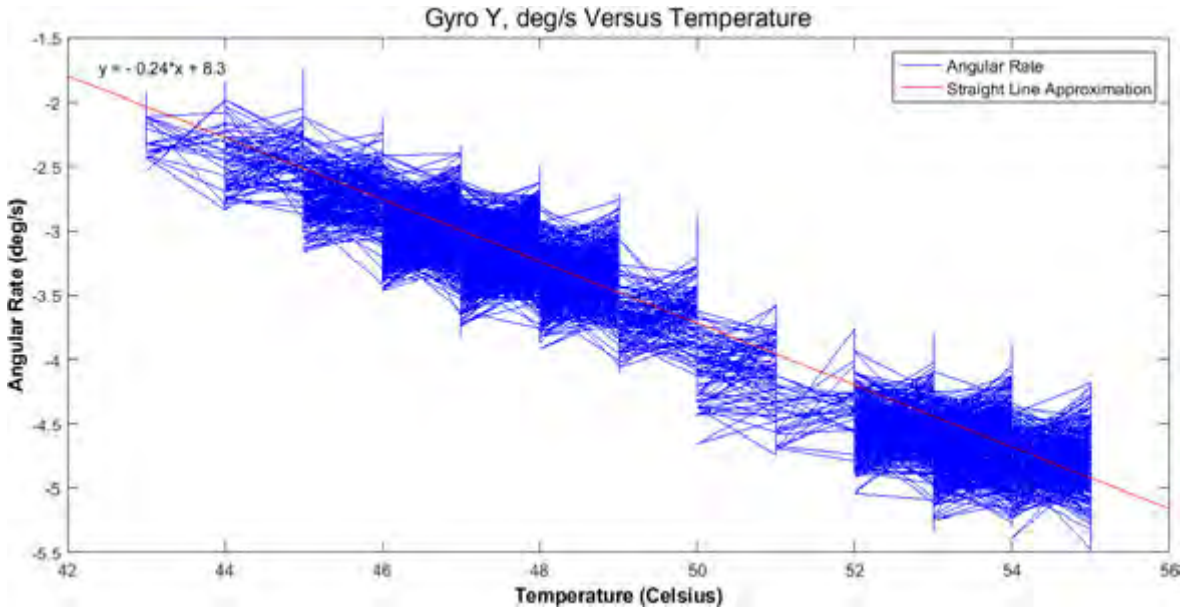

Figure 5.4: Gyroscope data showing variation of angular rate measurement with temperature

Extended Kalman Filter

In collaboration with a concurrent MSc. project an Extended Kalman Filter (EKF) was designed for the state estimation of the robot. However, the implementation, testing and tuning of the EKF is the sole work of this project.

An EKF is a computationally efficient estimation algorithm capable of estimating the state of a non-linear system taking into account the presence of model and measurement noise. The EKF uses the model information combined with actual sensor measurements to estimate the state. This blends the raw sensor measurements to account for the system dynamics and noise in a way that is optimal relative to a local linearization of the dynamics. A Kalman gain is used to weight the two signals, actual and estimated, based on their respective uncertainty in a least squares approach. The uncertainty of the signals is captured as a noise covariance.

The algorithm can be split into two distinct parts, as shown in **Figure 5.5**. The first part, known as the prediction stage, is to predict the new state of the robot using a previous estimate and a covariance matrix. The second part, known as the update stage, is where the predicted state is updated using data from sensors and the EKF filter outputs. The EKF is run every sampling period (10 ms) in order to obtain the new state estimate of the robot.

The error covariance is a measure of the accuracy of the estimated state vector. The algorithm is designed to minimize the state error covariance resulting in accurate state estimation.

Although the EKF is able to estimate the state of non-linear systems it operates on the linearised dynamics and therefore assumes the system is locally linear, i.e. linear in a small region around the operating point being analysed. A reliable mathematical model is required for accurate prediction of the states and model states must be observable to prevent divergence of the estimation. Additionally, it assumes the model and sensor noise, used as inputs to the algorithm, are white noise, ideally with a Gaussian distribution. If the noise is not Gaussian, the solution is sub-optimal since the covariances are non-exact approximations. However, it still provides the best linear unbiased estimator of a linearised system's state.

Detailed equations for the EKF filter can be found in [63, 71].

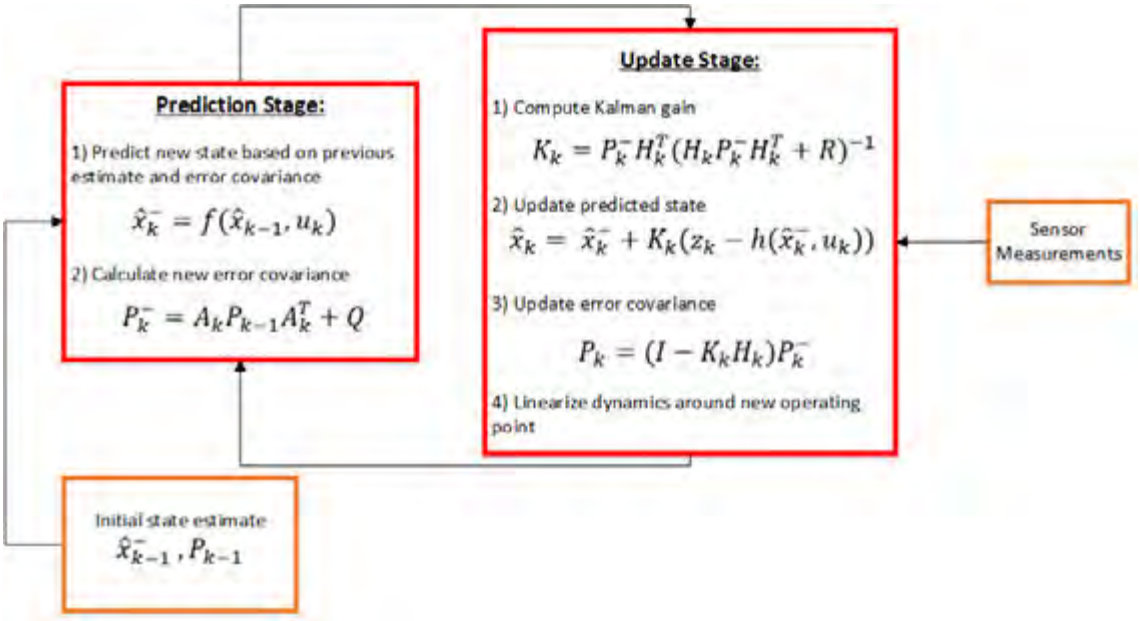

Figure 5.5: EKF structure

Reference attitude through encoder and potentiometer

The attitude of the robot can also be determined using the potentiometer, attached to the replacement gripper, and motor encoder. The potentiometer gives an absolute measurement of θ_1 and the motor encoder gives a relative measurement of θ_2.

By having redundancy in the attitude estimation i.e. being able to determine the attitude through either the EKF or the potentiometer and encoder allows for the validation of the EKF algorithm. Additionally, the EKF algorithm can be used to initialise the encoder so that the angle measurement is given as an absolute angle.

The potentiometer signal had some high frequency noise and was therefore filtered using a 1st order low-pass filter with a 8 Hz cut-off frequency to get a more accurate angle measurement. It is continuously sampled (100 Hz) using a 12-bit ADC, and has a theoretical resolution of $0.065°/\text{bit}$ over the operating range.

The encoder signal is noise free and therefore provides the most accurate measurement of the angle between the robot links. Further, the encoder is unaffected by out-of-plane motion, which negatively affects the accuracy of the EKF measurement since the model used for the algorithm is planar. It has two channels and 500 ticks per revolution and is read using input capture in an encoder mode which measures the rising and falling edges of both channels resulting in a resolution of $0.18°/\text{encoder tick}$, this process is called quadrature decoding.

5.2 Power line sensing

An infrared LED and phototransistor were mounted on the gripper arms, one on each side, in order to sense the presence of the conductor.

The signal from the IR phototransistor is fed into an ADC which is sampled continuously. The presence of the line can then be identified by a sharp decrease in the ADC value as the conductor blocks the light from the LED.

The detection of the line is used to actuate the gripper at the end of the swing in order to catch onto the conductor. Originally, the IR pair was mounted in the slot of the gripper arms, but as discussed in Chapter 9 this resulted in delayed actuation of the gripper and failure to close around the conductor in time. Therefore, the IR pair was moved to above the half-pulleys as shown in **Figure 4.20** so that the gripper would be actuated in time to catch onto the conductor.

5.3 Data logging

Data logging allows for the debugging of the robot as well as the comparison of real-world robot information to simulated information. The robot is capable of logging data, state information and other relevant operational information, at 100 Hz using either an Xbee to a PC or OpenLog (serial data logger) to an SD card.

The XBee operates at a maximum baud rate of 11500 bit/s and allows for real-time data analysis via a GUI. The OpenLog does not allow for real-time data analysis, however, it can operate at a baud rate up to 1 Mb/s without carrying the risk of data corruption(packet loss) over the air as the Xbee does.

5.4 Motor control

The link actuation motor is controlled via a Maxon ESCON Module 50/5 motor controller, which receives PWM and direction commands from the central microcontroller based on the required motor speed and direction.

The motor controller provides a simple way of interfacing to the motor and has a number of safety features for motor protection. However, the limits of the motor controller in terms of maximum output current are extremely conservative and prevent the extraction of motors full capability, as discussed in Chapter 6.3.

The motor controller can be used with ESCON Studio, a software package provided by Maxon, to record information such as output current and motor speed, allowing for the real-time analysis of the motor performance. This data logging feature was used (see Chapter 6.3) to perform system identification on the robot.

Chapter 6

System Identification

The generation of the optimal trajectories and the control of the robot depend on the validity of the mathematical models. Therefore, system identification was performed in order to verify the accuracy of the mathematical models and to determine unknown parameters such as friction coefficients.

The system identification was performed by comparing the data from the real robot, which is the reference, to the simulation. The closer the correlation between the simulation and the real robot, the more accurate the simulated model and the lower the plant model uncertainty.

The system identification was performed in three stages as discussed below.

6.1 Single pendulum friction estimation

Initially, system identification was performed on a single pendulum i.e. only one of the robot's links. This allowed for the identification of the friction coefficients of the replacement gripper joint and verification of the parameters obtained from the Solidworks model.

The test was performed as shown in **Figure 6.1**. The pendulum was held at some arbitrary initial angle and then released and allowed to swing freely until it came to rest. A video of the test can be found in Appendix D.

Figure 6.1: Single pendulum system identification experiment

The data from the robot was logged and then compared to the simulation as shown in **Figure 6.2**. The angle of the top link is obtained from the potentiometer coupled to the replacement gripper. The friction parameters used in the simulation are shown in **Table 6.1**.

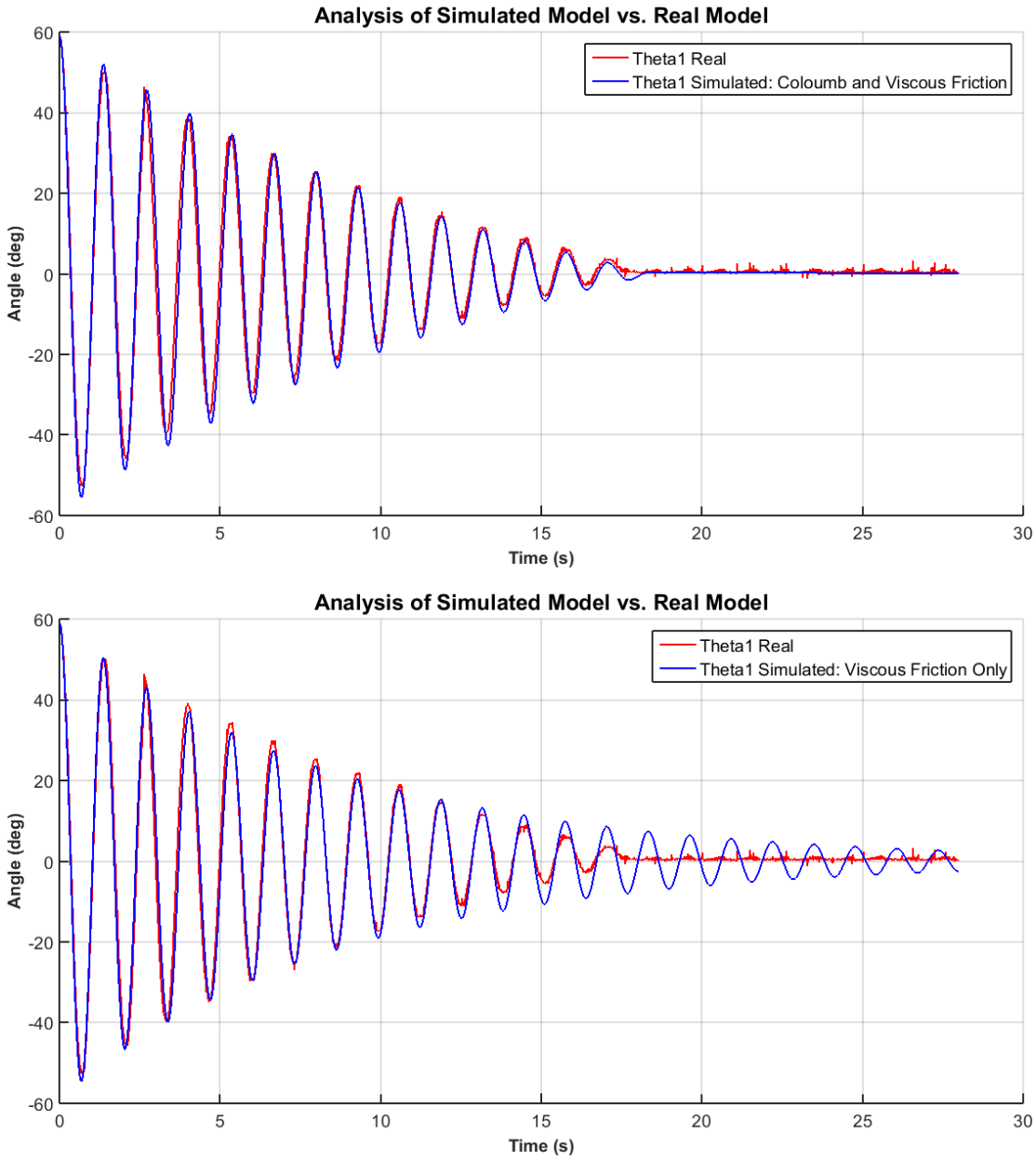

Figure 6.2: Single pendulum friction estimation. Top, simulation using Coulomb and viscous friction. Bottom, simulation using viscous friction only.

Table 6.1: Friction coefficient from single pendulum system identifcation

Model	Specification	Value	Units
Coulomb and viscous friction	Coulomb friction coefficient, F_c	0.105	Nm
	Viscous friction coefficient, F_v	0.05	$\left(\frac{\mathrm{Nms}}{\mathrm{rad}}\right)$
Viscous friction only	Viscous friction coefficient, F_v	0.1	$\left(\frac{\mathrm{Nms}}{\mathrm{rad}}\right)$

The Coulomb and viscous friction model, discussed in Chapter 2.5, was used to obtain the friction coefficients. As discussed in Chapter 2.5, the viscous friction only model was used for the control of the robot. However, during system identification it is better to use a more detailed model as viscous

friction alone cannot account for the real robot's behaviour, as shown in the bottom graph of **Figure 6.2**. The total RMS error for the model with Coulomb and viscous friction is 3.5 degrees, while the model with viscous friction only is 13.6 degrees. Further, the model with viscous friction only, continues to oscillate long after the real robot has settled.

From **Figure 6.2** it can be seen that the simulation with Coulomb and viscous friction is accurate despite the overshoot at the troughs of the swing. This overshoot is most likely the effect of static friction, which was neglected in the simulation. The static friction of the joint would act to decrease the system's energy faster than expected and would act at the turning points as the link's velocity goes through zero.

6.2 Double pendulum friction estimation

The next stage of the system identification was to test the planar double pendulum model which the optimal trajectory generation and control are based on.

The test was performed by starting the robot from some arbitrary position on the conductor, which was replicated by a steel pipe of the same diameter, as shown in **Figure 6.3**. The gripper was then opened and the robot allowed to swing freely until it came to rest. The link actuation motor is disabled in the test and therefore provides no effect on the swing behaviour. A video of the test can be found in Appendix D.

Figure 6.3: Double pendulum system identification experiment

The data of the robot was captured throughout the swing and then compared to the simulation. The top link angle, θ_1,was again measured using the potentiometer and the relative angle between the two links, θ_2, was measured using the motor encoder. The results of the test are shown in **Figure 6.4**.

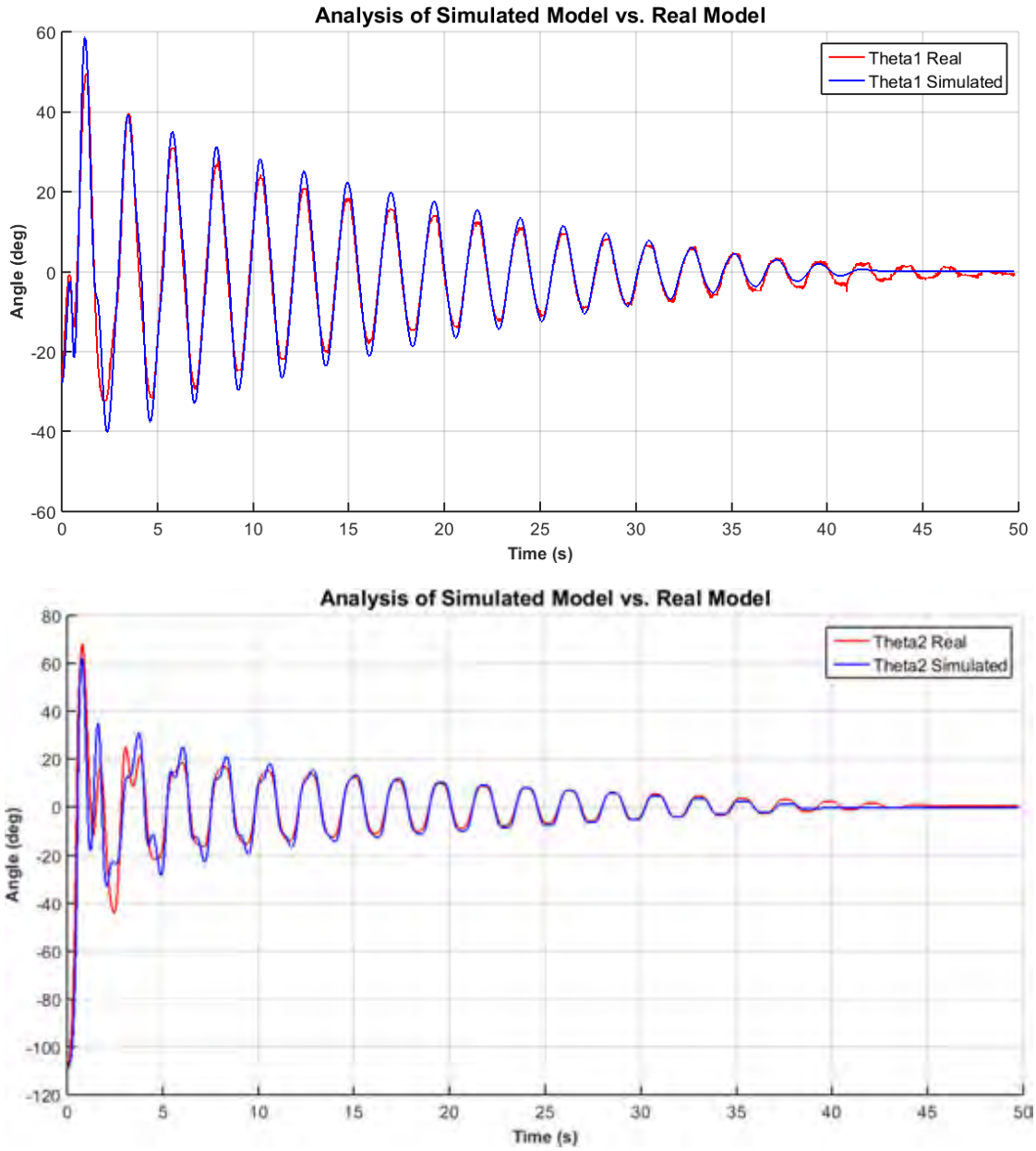

Figure 6.4: Double pendulum friction estimation. The top graph shows a comparison between the real measurement of θ_1 and the simulated measurement. A similar comparison is shown in the bottom graph for θ_2.

From **Figure 6.4**, it can be seen that double pendulum simulation accurately tracks the real robot measurements, despite the initial lack of fidelity, and is therefore a reliable model on which to base the control design for achieving brachiation. The friction parameters obtained from the simulation are shown in **Table 6.2**.

Table 6.2: Friction coefficient from double pendulum system identifcation

Robot Link	Specification	Value	Units
1	Coulomb friction coefficient, F_{c_1}	0.255	Nm
	Viscous friction coefficient, f_{v_1}	0.15	$\left(\frac{\mathrm{Nms}}{\mathrm{rad}}\right)$
2	Coulomb friction coefficient, F_{c_2}	0.3	Nm
	Viscous friction coefficient, f_{v_2}	0.25	$\left(\frac{\mathrm{Nms}}{\mathrm{rad}}\right)$

The friction coefficient of the replacement gripper joint increased from the result found in the single pendulum test due to the increased weight applied to the joint.

6.3 Motor step test

The final stage of the system identification was to perform a step test to verify the actuator modelling and the complete systems' behaviour.

The robot was left hanging vertically down and then a step in the motor voltage from 0 V to 5 V was applied. The initial and final positions of the robot are shown in **Figure 6.5**. A video of the test can be found in Appendix D.

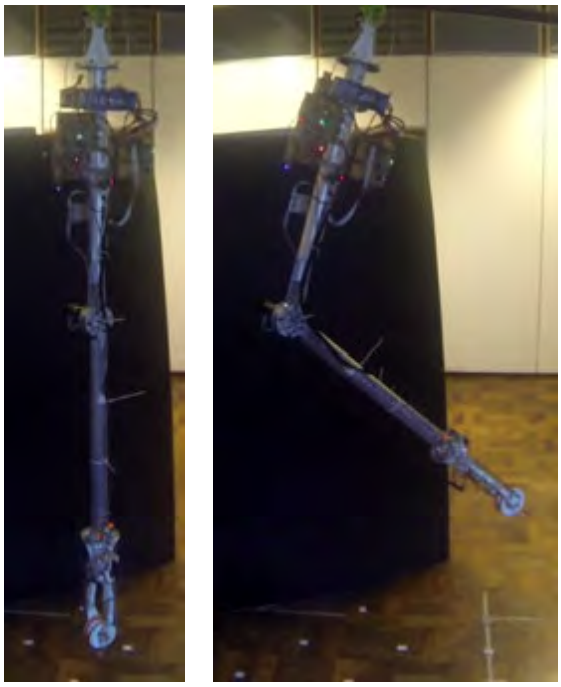

Figure 6.5: Motor step experiment. Left is the initial position of the robot. Right is the final position of the robot.

Similar to the double pendulum test, the robot data was logged and compared to a simulation. However, before the trajectory of the links could be compared the actuator model first had to be verified.

The motor controller current output was logged using the ESCON Studio software package and then converted to a torque as

$$torque = k_m I_{controller} N \eta \tag{6.1}$$

where, k_m is the motor torque constant, $I_{controller}$ is the controller output current, N is the gearbox ratio and η is the gearbox efficiency. The value of the parameters can be found in **Table 3.5**.

This torque was then compared to two simulation torques. One where the speed input came from the model itself, and the other where the speed input came from the real robot. The results of torque comparison can be seen in **Figure 6.6**.

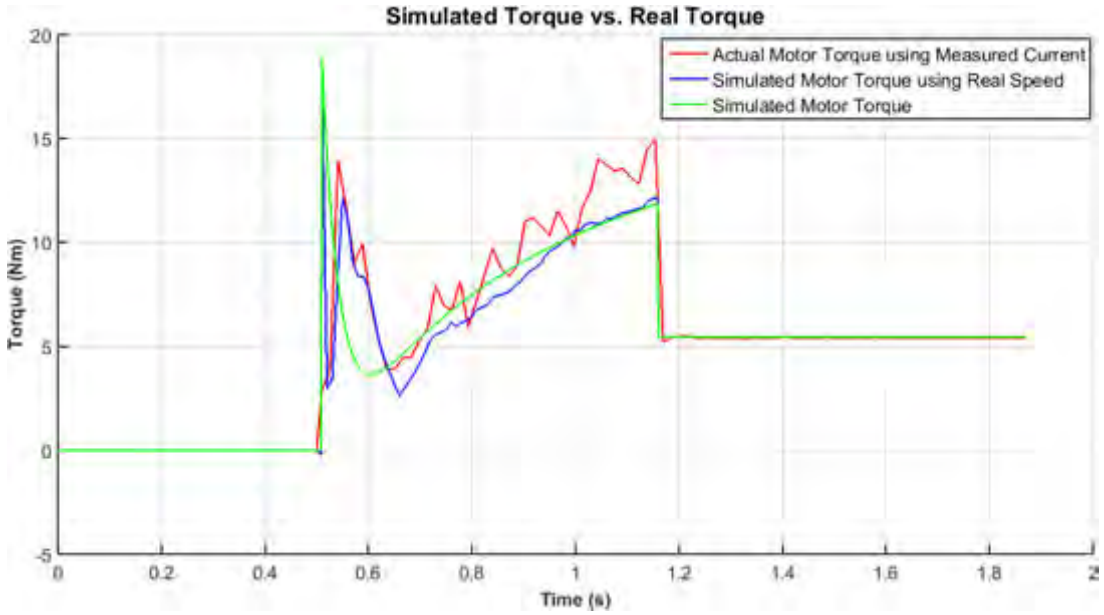

Figure 6.6: Actuator model verification

The simulation torque using the real speed is the best match to the actual torque. The robot's link speed in the simulation differs from the real robot's speed and therefore causes the slight mismatch between the simulation torque and the actual torque.

The initial spike in torque for the simulation is higher than the actual torque since the simulation was run at sampling frequency of 1 ms, while the data for the output current was logged at 15.7 ms. The low data logging rate of the software is a result of the time period data was logged for, as the period increased the logging rate decreased. The data was therefore logged for the shortest possible period to obtain the best logging rate.

While the simulation torque is not an exact match of the actual torque, the torque profile is fairly accurate and therefore the reliability of the motor model was confirmed. After confirming the motor model, the measured and simulated link trajectories were compared as shown in **Figure 6.7**.

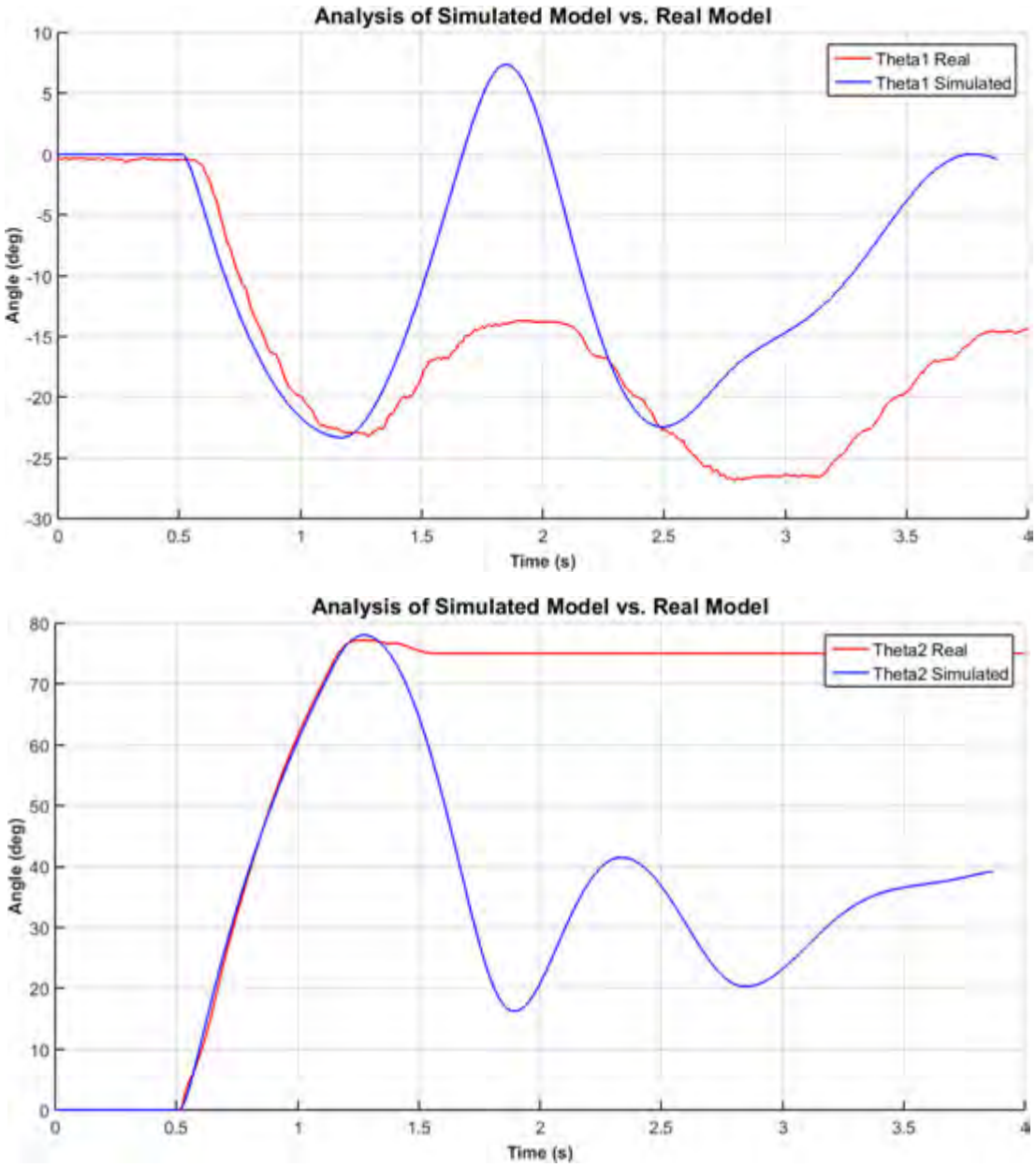

Figure 6.7: Motor step results

The difference in the trajectories is a result of the simulation neglecting static friction of the joints. The static friction in the second joint is enough to lock the second angle and since the simulation does not have this static friction it continues to oscillate.

Therefore, only the transient behaviour of the robot, from 0–1.25 s, is of importance in confirming the robot model and parameters. It can be seen that the transient behaviour is well matched between the simulation and the real robot. Thus the robot parameters and mathematical models are accurate representations of the real system.

Finally, the Maxon controller output current is analysed to verify its specifications as provided by the datasheet and shown in **Table 3.5**. The motor controller output current is shown in **Figure 6.8**.

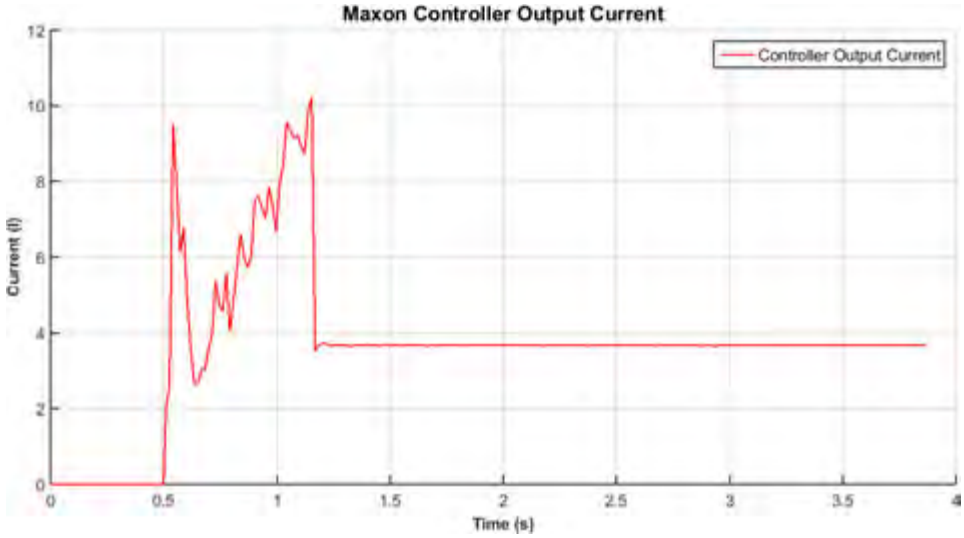

Figure 6.8: Maxon controller output current

The controller datasheet is quoted to have a maximum current output of 15 A for a period of less than 20 seconds, but in testing it was found that this period was significantly shorter, and actually in the range of 0.5 – 1 second. The period being lower than specified is most likely due to differing thermal conditions, the specifications given at lower operating temperatures or with air cooling to the motor.

Further, the maximum continuous current is quoted at 5 A but in testing it is shown that the maximum continuous current is only 3.7 A. The true controller output specifications where therefore used when simulating the brachiation manoeuvres of the robot. The final robot parameters can be found in **Table 3.4**.

Chapter 7

Control design

The control system design of the robot is presented in this chapter. The design is especially challenging since the robot is underactuated and highly nonlinear. A partial feedback linearization approach is proposed for the control of the robot.

The feedback linearization method is discussed in Section 7.1, followed by the design of the controller in Section 7.2 and testing of its ability to track the reference trajectory in Section 7.3. Finally, a method to overcome static friction is proposed in Section 7.4 along with the controller architecture.

7.1 Partial feedback linearization

The aim of feedback linearization is to simplify the control design of a nonlinear system by linearizing it and creating a linear map of inputs to outputs. This linearized model can then be used to design a controller which can command the system to track a desired reference trajectory. A disadvantage of feedback linearization is that the control inputs are not the same as the physical system's inputs and the designer may lose sight of the latter.

The robot in this project is underactuated and therefore full feedback linearization is not possible. However, partial feedback linearization (PFL) of either the actuated joint, known as collocated PFL or the passive joint, known as non-collocated PFL is possible. This linearization is state-dependent and valid across the entire operating region but depends on perfectly known (i.e. certain) parameters.

The partial feedback linearization of both actuated and unactuated joints is discussed below.

Collocated PFL

First, the equations of motion for the double pendulum are derived. The mathematical model for the double pendulum, presented in Chapter 2, is shown here for convenience in **Figure 7.1**.

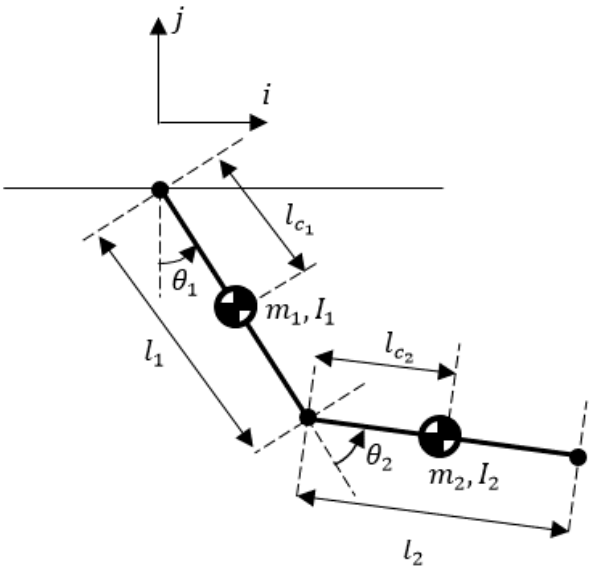

Figure 7.1: Generalised coordinates of double pendulum robot configuration

The state vector was chosen as

$$q = (\theta_1, \theta_2)^T \tag{7.1}$$

Then by using the manipulator equation (2.5), the angular accelerations are

$$\ddot{\theta}_1 = -\frac{\left(F_1 + m_{12}\ddot{\theta}_2 + c_{11}\dot{\theta}_1 + c_{12}\dot{\theta}_2 + G_1\right)}{m_{11}} \tag{7.2}$$

$$\ddot{\theta}_2 = \frac{\tau - F_1 - m_{21}\ddot{\theta}_1 - c_{21}\dot{\theta}_1 + c_{22}\dot{\theta}_2 + G_2}{m_{22}} \tag{7.3}$$

In the general PFL method, the output map is chosen such that

$$y = f(q) \tag{7.4}$$

From the method described in [72, 17] the actuated joint, q_2, is then commanded such that

$$\ddot{q}_2 = \ddot{\theta}_2 = \bar{J}^{+}\left[u - \dot{J}\dot{q} + J_1 m_{11}^{-1}\left(c_{11}\dot{\theta}_1 + c_{12}\dot{\theta}_2 + G_1 + F_1\right)\right] \tag{7.5}$$

where, u is the controller output. The Jacobians in (7.5) are partial derivatives of the output map in (7.4) with respect to the states. The Jacobians are then defined as

$$J = \begin{bmatrix} J_1 \\ J_2 \end{bmatrix} = \begin{bmatrix} \dfrac{\partial f}{\partial q_1} \\ \dfrac{\partial f}{\partial q_2} \end{bmatrix} \tag{7.6}$$

$$\bar{J} = J_2 - J_1 m_{11}^{-1} m_{12} \tag{7.7}$$

$$\bar{J}^{+} = \bar{J}^T(\bar{J}\bar{J}^T)^{-1} \tag{7.8}$$

For the collocated PFL case, the output map is chosen as

$$y = q_2 = \theta_2 \tag{7.9}$$

The input torque is then collocated with the output since the output shaft of the motor directly controls θ_2 as discussed in Chapter 4.2.

The Jacobians then evaluate to

$$J_1 = 0,\ J_2 = 1, \dot{J} = 0,\ \bar{J} = 1,\ \bar{J}^T = 1 \tag{7.10}$$

Substituting (7.10) into (7.5), we have the commanded joint acceleration as

$$\ddot{q}_2 = \ddot{\theta}_2 = u \tag{7.11}$$

Substituting (7.11) and (7.2) into (7.3), we have the commanded torque as

$$\tau = -m_{12}m_{11}^{-1}\left(F_1 + m_{12}u + c_{11}\dot{\theta}_1 + c_{12}\dot{\theta}_2 + G_1\right) + F_2 + m_{22}u + c_{21}\dot{\theta}_1 + c_{22}\dot{\theta}_2 + G_2 \tag{7.12}$$

By inputting the torque from (7.12) into the system, the robot can be forced to track a reference trajectory.

Non-collocated PFL

In the non-collocated PFL case, the angle θ_1 which corresponds to the unactuated DOF is usually controlled. However, we choose to control the height of the robot's end effector and choose the output map as

$$y = -(l_1\cos\theta_1 + l_2\cos(\theta_1 + \theta_2)) \tag{7.13}$$

Ultimately, the goal of the robot at the end of the brachiation swing is to get the free gripper back onto the line and therefore controlling the end-effector height is valuable. Further, the optimal trajectories were designed so that the end-effector slightly overshoots the conductor to ensure an excess of energy in the system so that brachiation is more reliable. Therefore, by being able to control the end-effector height, the robot can avoid crashing into the line at the end of the swing.

As in the collocated case, the actuated DOF is commanded as in (7.5). The Jacobians for the output mapping in (7.13) evaluate to

$$J = \begin{bmatrix} J_1 \\ J_2 \end{bmatrix} = \begin{bmatrix} l_1 sin\theta_1 + l_2\sin(\theta_1 + \theta_2) \\ l_2\sin(\theta_1 + \theta_2) \end{bmatrix} \tag{7.14}$$

$$\dot{J} = \begin{bmatrix} \dot{J}_1 \\ \dot{J}_2 \end{bmatrix} = \begin{bmatrix} \dot{\theta}_1 l_1 cos\theta_1 + \dot{\theta}_1 l_2 cos(\theta_1+\theta_2) + \dot{\theta}_2 l_2 cos(\theta_1+\theta_2) \\ \dot{\theta}_1 l_2 cos(\theta_1+\theta_2) + \dot{\theta}_2 l_2 cos(\theta_1+\theta_2) \end{bmatrix}$$

$$\bar{J} = l_2\sin(\theta_1 + \theta_2) - m_{11}^{-1}m_{12}(l_1 sin\theta_1 + l_2\sin(\theta_1 + \theta_2)) \tag{7.15}$$

$$\bar{J}^+ = \frac{m_{11}}{l_2\sin(\theta_1 + \theta_2) - m_{12}(l_1 sin\theta_1 + l_2\sin(\theta_1 + \theta_2))} \tag{7.16}$$

Which can be substituted into (7.5) to determine the required command for $\ddot{\theta}_2$.

The torque required to achieve tracking of a desired reference trajectory is then

$$\tau = \ddot{\theta}_2 m_{22} + F_2 + m_{21}\left(-\frac{(F_1 + m_{12}\ddot{\theta}_2 + c_{11}\dot{\theta}_1 + c_{12}\dot{\theta}_2 + G_1)}{m_{11}}\right) + c_{21}\dot{\theta}_1 + c_{22}\dot{\theta}_2 + G_2 \quad (7.17)$$

where, $\ddot{\theta}_2$ is defined as in (7.5).

PFL selection

The collocated mapping was used for the whole swing but it would be possible to switch to a non-collocated mapping in the final part of the swing. The switch would allow the position set-point and velocity to change as the end-effector got close to the line. The non-collocated mapping, described in (7.13), cannot be used for the entire swing since it does not take into account which side of the line the reference height is. If the non-collocated mapping is used before the vertical position (both links vertically down), the robot may try to swing backwards to reach its initial position instead of its desired final position.

While the exclusive use of the collocated PFL mapping proved successful, as shown in Chapter 9, it is believed that the success rate could have been increased by implementing the switch to the non-collocated mapping.

7.2 Controller design

The PFL mapping allows for the design of the controller based upon a linearized plant. The linearized plant is given (from (7.11)) by the transfer function

$$P = \frac{1}{s^2} \quad (7.18)$$

which is a standard double integrator i.e. a plant with two poles at the origin.

By using the Nichols chart, we are able to see the behaviour of the plant over the entire frequency range. The Nichols chart of the plant is shown in **Figure 7.2**. From **Figure 7.2**, we see that without compensation the loop goes through the -1 point and therefore is unstable and requires a dynamic controller.

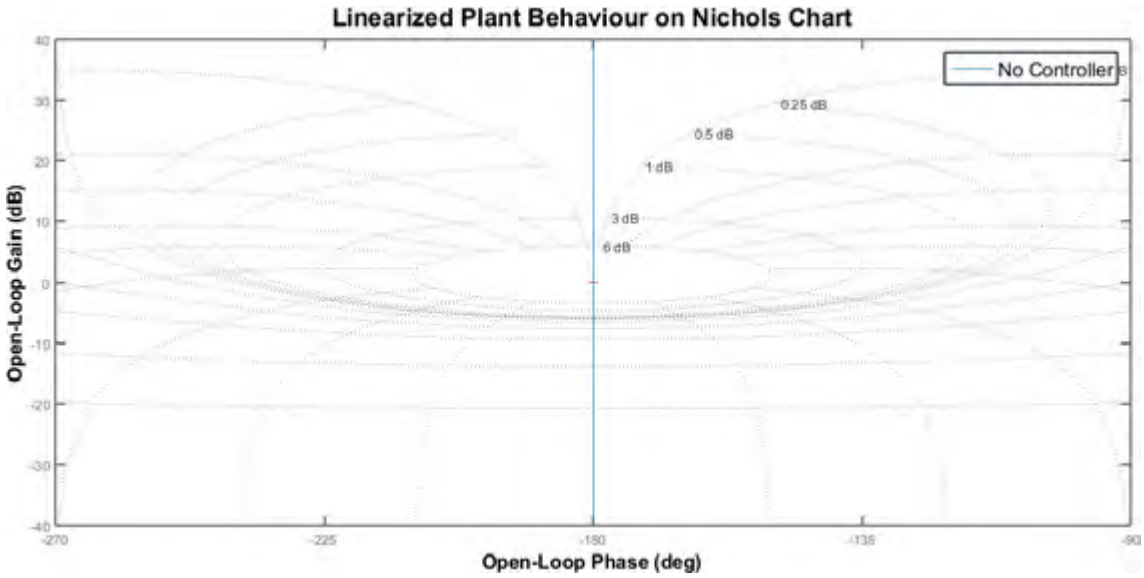

Figure 7.2: Linearized plant on Nichols chart

PD control is applied to the plant to give the system high frequency gain, allowing it to track the reference trajectory. The PD controller is implemented with a low frequency zero, adding phase lead to get around the -1 point and then a less dominant pole to ensure that the controller is "proper" (i.e. does not roll up at high frequency). Additionally, a controller gain is tuned to shape the loop gain. The Nichols chart of the plant with a PD controller is shown in **Figure 7.3**

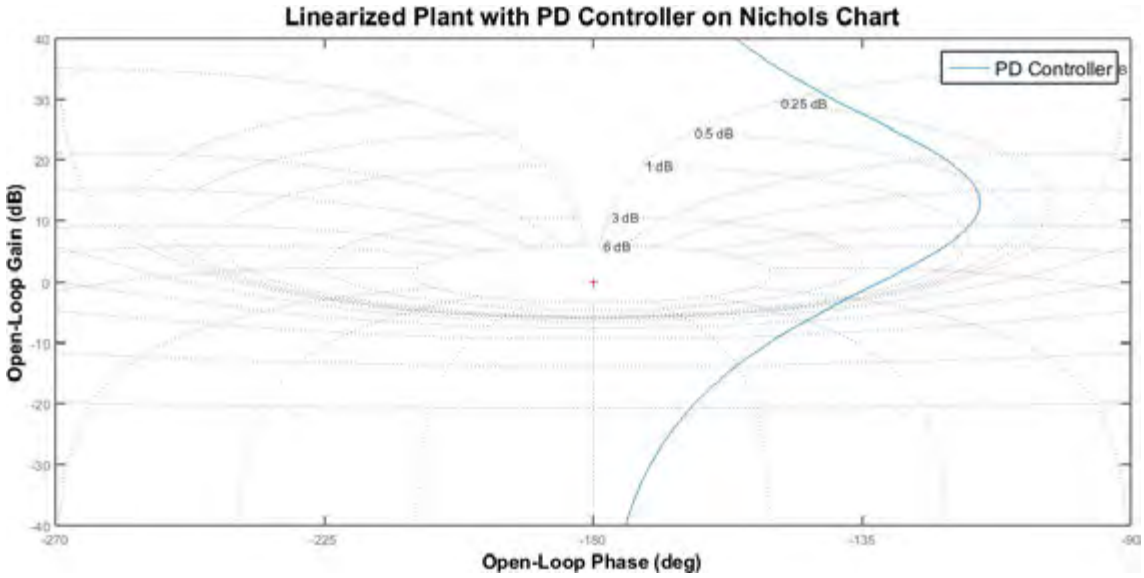

Figure 7.3: Linearized plant with PD control on Nichols chart

In order to remove the steady-state tracking error, an integrator and a low frequency zero, sufficiently below the frequency of the zero for the PD controller, is added. This increases the low frequency gain of the system, improving the controller's steady-state tracking behaviour. The behaviour of the final PID controller on a Nichols chart is shown in **Figure 7.4**

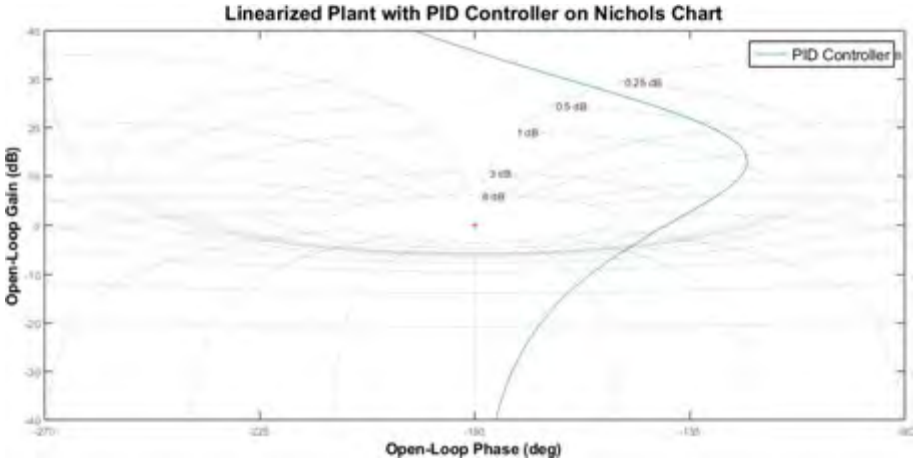

Figure 7.4: Linearized plant with PID control on Nichols chart

From the optimal trajectories, found in Appendix B, the trajectories take approximately 1.4 s to complete. Therefore a controller with sufficiently fast response behaviour was designed. The closed loop step response of the system is shown in **Figure 7.5**

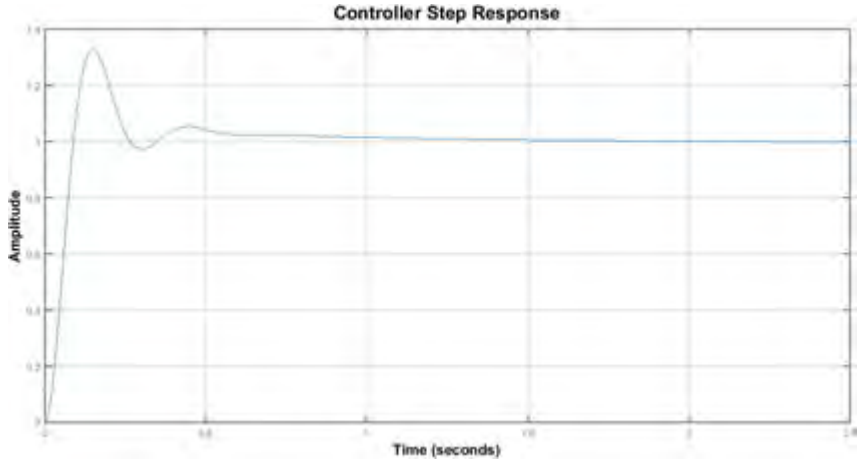

Figure 7.5: Step response of PID controller on linearized plant

From **Figure 7.5**, the rise time is approximately 60 ms and therefore would be fast enough to account for uncertainties and disturbances. Although the overshoot seems large, it is an exaggeration of the controller's true behaviour since the real reference signal will be smooth and not a step.

The final controller as a transfer function is then

$$G = \frac{1.4s^2 + 2.4s + 1}{0.05s^2 + s}\left(\frac{1}{s^2}\right) \tag{7.19}$$

7.3 Trajectory tracking and robustness

The ability of the controller to track a reference trajectory is the true test of its performance. In order to test the controller's tracking performance, the robot was simulated with a simulation structure as shown in **Figure 7.6**.

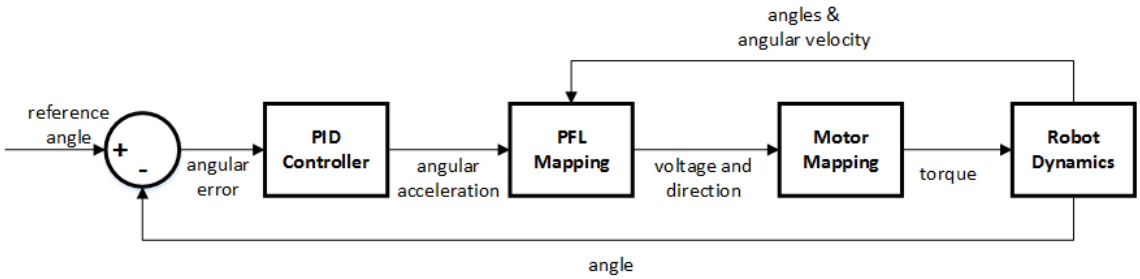

Figure 7.6: Simulation structure

The reference angle, is the trajectory of θ_2 since the collocated PFL output map was selected, where the reference trajectory is generated in Chapter 3.

The tracking behaviour of the controller for the first phase of the vibration damper negotiation swing was analysed. The optimal trajectory and related results for the manoeuvre can be found in Appendix B.

To verify the performance of the controller, the tracking of the θ_1 and θ_2 optimal trajectories was analysed. The height of the end-effector was also analysed since as previously discussed, the ultimate goal of the robot is to catch onto the conductor once it has swung past the obstacle. Finally, the controller actuation required to track the reference trajectory is compared to the optimal actuation to gain an understanding of how effective the controller is in terms of energy usage. The results of the trajectory tracking are shown in **Figure 7.7**.

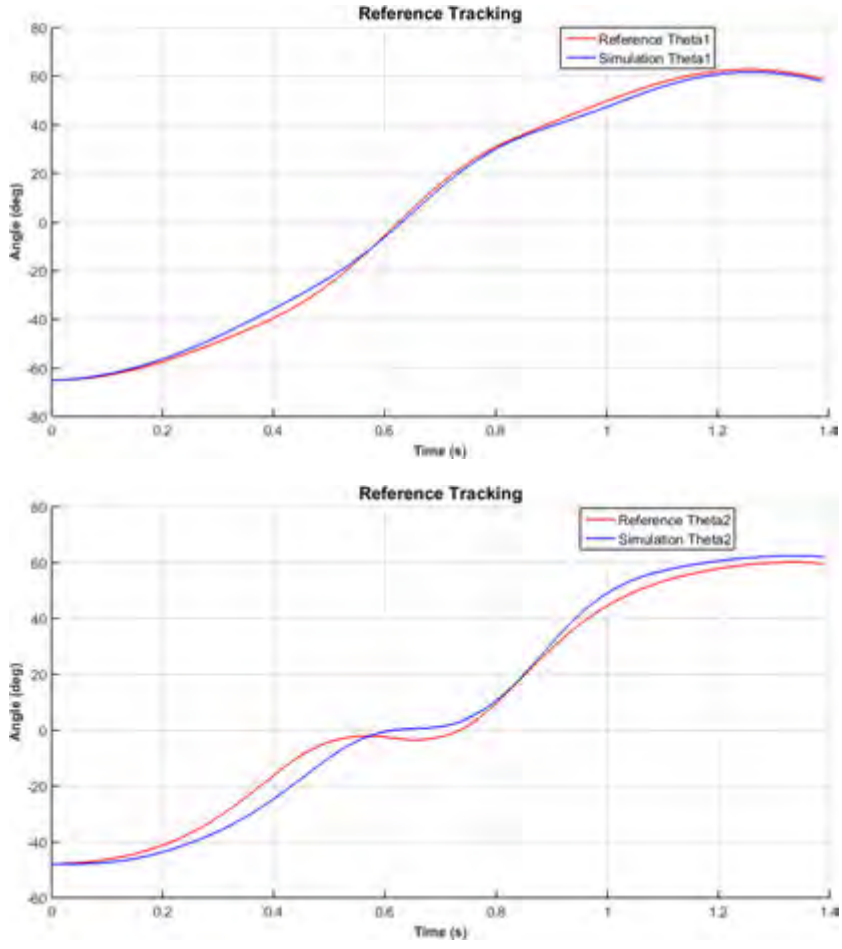

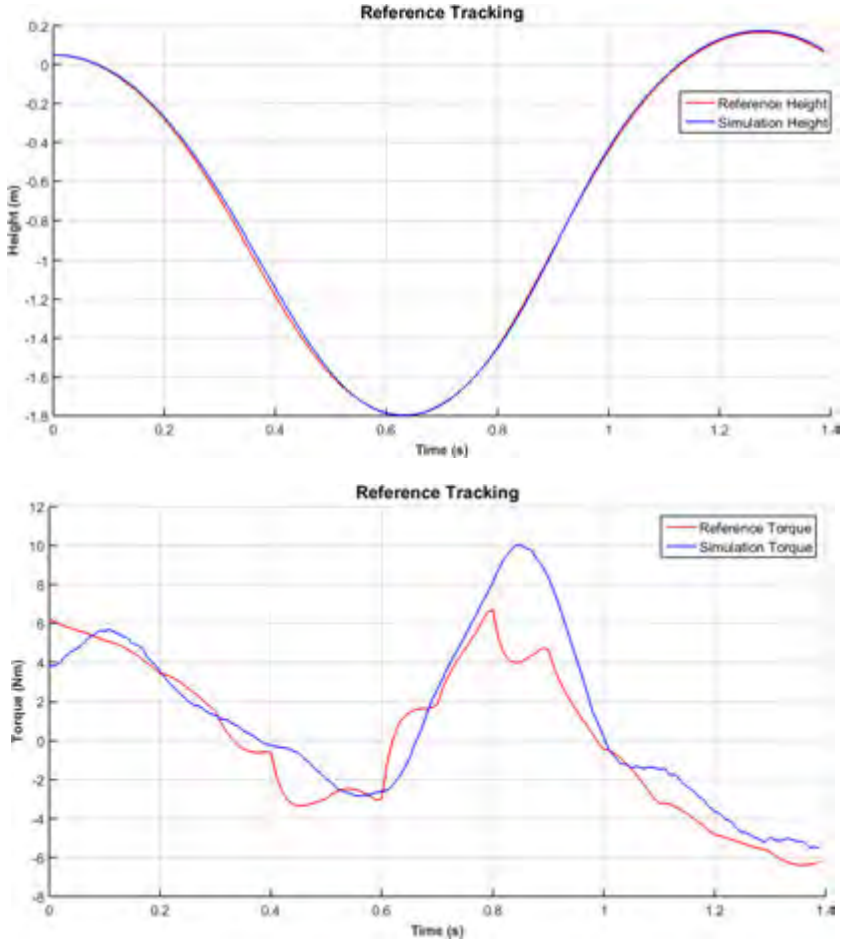

Figure 7.7: Vibration damper trajectory tracking results

From **Figure 7.7**, the results show that the controller accurately tracks the θ_2 reference trajectory. Although the final values of θ_1 and θ_2 deviate from the optimal values, the end-effector height still tracks accurately, therefore the robot will be able to brachiate successfully. Additionally, the controller actuation torque closely matches the optimal torque, aside from the small mismatch at 0.9 s, and therefore the resulting swing is still energy efficient. Further, it should be noted that because the controller has finite bandwidth, perfect trajectory tracking is not realisable. Also, the optimal trajectory is crude as it is based on a finite gridding of the time points over a swing.

The reader should note that the height of the end-effector in **Figure 7.7** is above the 0 m height since the pivoting point, and hence the origin of the robot's coordinate frame, is slightly below the line due to the design of the replacement gripper as shown in **Figure 7.8**. Therefore, from the robot's coordinate frame, the line is actually 0.05 m above the origin.

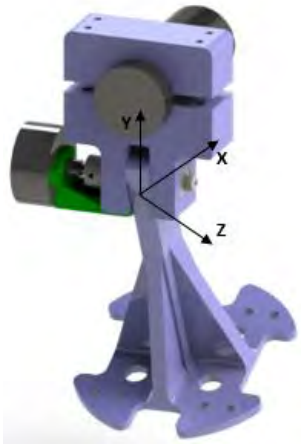

Figure 7.8: Replacement gripper showing coordinate frame of robot

Reference tracking with plant uncertainty

After evaluating the controllers reference tracking, the controller's robustness and ability to track the reference with plant uncertainty was evaluated.

The uncertainty assigned to the robot parameters was made realistic by evaluating each robot parameter and determining what level of uncertainty would be associated with it. For example, the mass properties of the robot are highly accurate since the entire robot was modelled in Solidworks, with a high level of detail, including weight of the bolts and nuts in the assembly and therefore the uncertainty of the mass is small. Other parameters, such as COM position and friction even though system identification was performed, have a higher level of uncertainty. The robot parameters and their corresponding level of uncertainty are given in **Table 7.1**.

Table 7.1: Robot parameter uncertainty

Robot Parameter	Uncertainty	Unit
Mass	2	%
COM position	15	%
Inertia	15	%
Friction coefficient	30	%
Starting angle	5	°

From **Table 7.1**, sets of robot parameters were generated where the robot parameter was allowed to vary between an upper and lower limit defined as

$$Parameter\ upper\ limit = \ Original\ parmater(1 + parameter\ uncertainty) \quad (7.20)$$

$$Parameter\ lower\ limit = \ Original\ parameter(1 - parameter\ uncertainty) \quad (7.21)$$

The robot was then simulated 1000 times, each time with a different set of robot parameters. Two worst-case scenarios were identified. The first scenario was where the set of robot parameters generated the largest difference between the final value of θ_1 and the θ_1 reference and the other scenario, the set of robot parameters that generated the largest between the final value of θ_2 and the θ_2 reference. The results of the worst-case scenarios are shown in **Figure 7.9** and **Figure 7.10**.

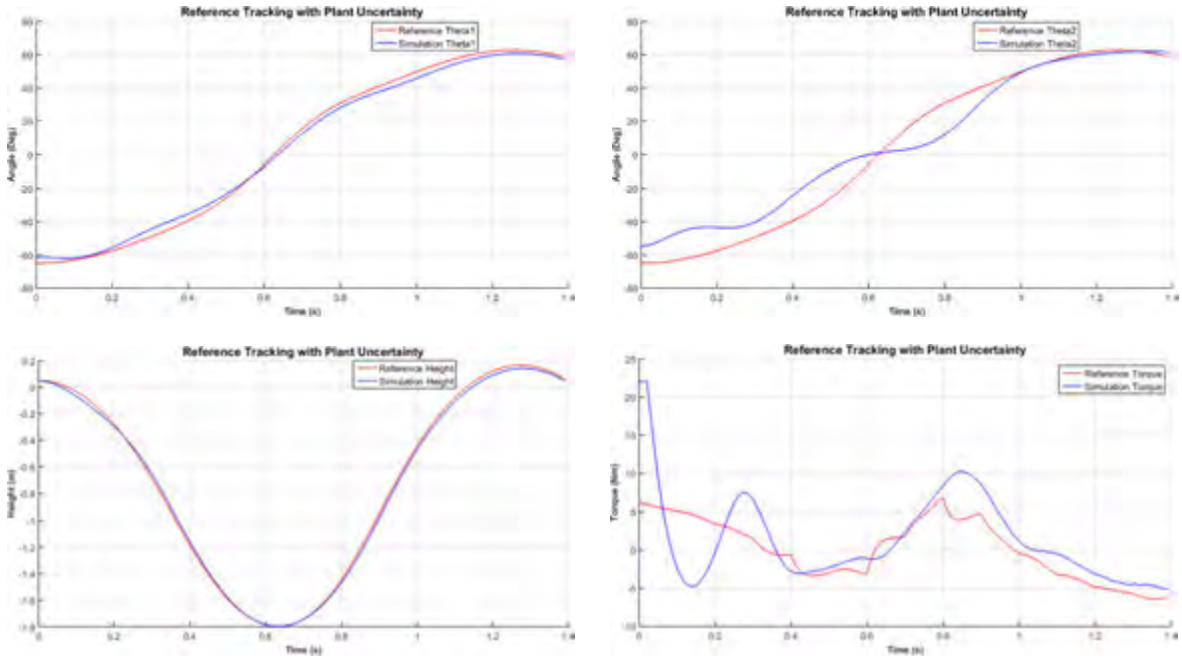

Figure 7.9: θ_1 worst-case scenario of vibration damper trajectory tracking results

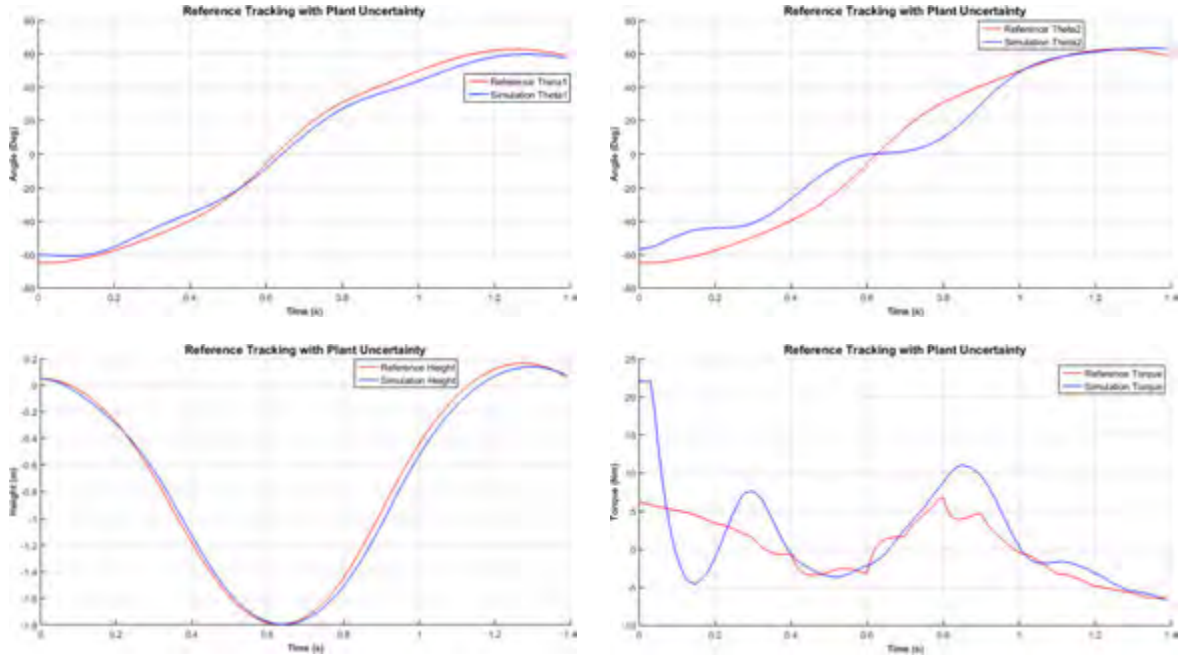

Figure 7.10: θ_2 worst-case scenario of vibration damper trajectory tracking results

From **Figure 7.9** and **Figure 7.10**, it can be seen that in the worst-case scenarios despite the tracking of the reference angle, θ_2, being poor for most of the swing, in the final part of the swing the controller accurately tracks the reference trajectory resulting in a successful swing. While successful, the controller actuation torques are far greater than the optimal torque resulting in energy inefficient swings.

7.4 Dither

The designed controller neglects the static friction of the joints, which will have an effect on the performance of the robot. Thus, the designed controller will not work as expected.

The static friction will be greatest in the lower joint, the joint connecting the two links, since this is where the motor is connected. To overcome the static friction of the joint, a sinusoidal dither torque was imposed on the required torque calculated in (7.12).

The dither torque is a sinusoidal torque at 10 Hz. As the torque is sinusoidal it only acts to overcome the static friction and has no effect on the controller's ability to track the reference trajectory at lower frequencies. A triangular wave could also have been used for the dither, as this would have provided more jerk. However, this would also cause a higher shock load on the motor gearbox, accelerating mechanical wear.

A frequency of 10 Hz is chosen as it is slow enough to actuate the motor, overcoming the static friction and fast enough to avoid affecting the controller behaviour. It should be noted that the dither signal causes vibrations, which result in mechanical wear of the actuation motor, and therefore it is desirable to minimise the amplitude of the signal.

The magnitude of the dither torque and its effect on θ_2, the angle between the two links, was analysed. A dither torque magnitude of 2, 2.5 and 3 Nm was tested as shown in **Table 7.2**. The test was conducted with the robot hanging vertically down, however it was extremely difficult to keep the links perfectly vertical due to the high static friction and therefore θ_2 does not oscillate around $0°$.

Based on **Table 7.2**, a dither torque of 2.5Nm was selected as the change in θ_2 is great enough to overcome the static friction reliably, since the static friction might vary as the link is rotated. With the addition of the dither torque, the final control structure is then as shown in **Figure 7.11**.

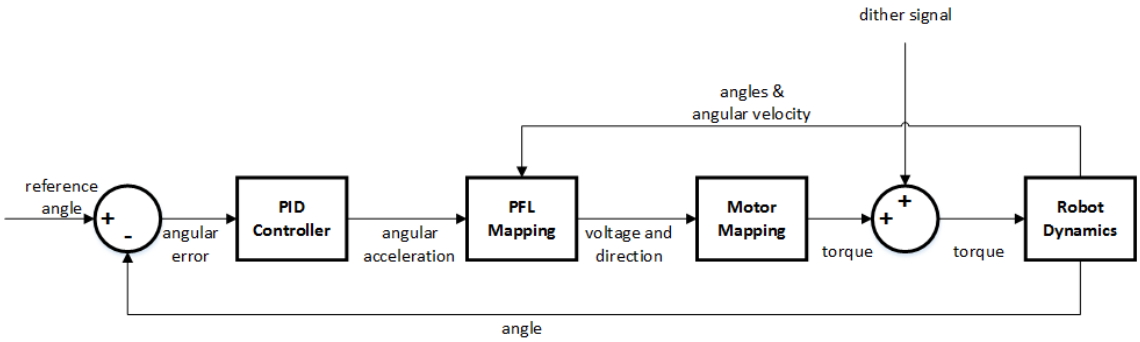

Figure 7.11: Final Controller Structure

Table 7.2: Effect of dither torque on θ_2

Dither Torque Magnitude (Nm)	Resulting effect on θ_2	Average amplitude of θ_2 oscillation(°)
2	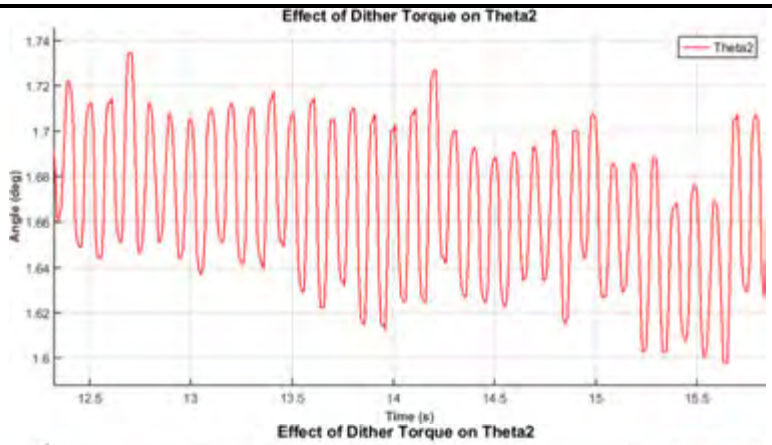	0.08
2.5	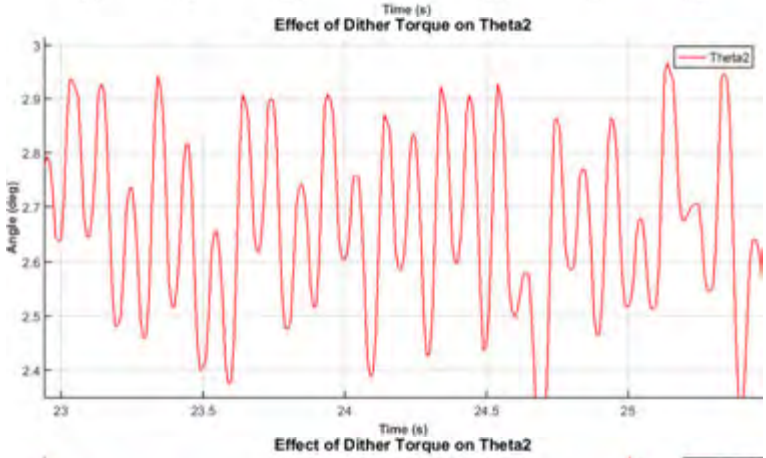	0.3
3	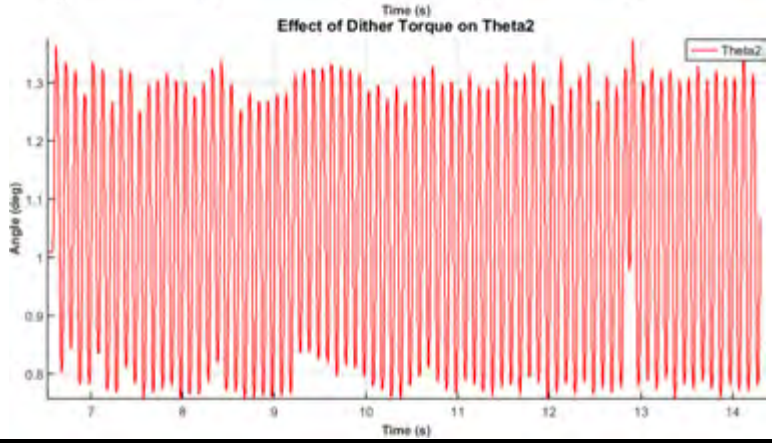	0.5

Chapter 8

Preliminary Testing

Before the final brachiation tests were conducted, the underlying sub-systems were tested to assess their performance and ensure that brachiation would be successful.

The sub-system tests included the testing of the gripper driving and loading capabilities, the IMU data quality, the accuracy of the EKF attitude estimation and finally position control of the robot, the results of the tests are discussed below.

8.1 Gripper testing

The gripper driving and loading capabilities were tested in order to validate the mechanical design of the gripper.

8.1.1 Driving testing

The gripper's ability to drive along the conductor is key to the robot's ability to perform inspection since driving allows the robot to traverse conductor spans faster and with a higher energy efficiency than continuously brachiating.

The test setup is shown in **Figure 8.1**. A steel pole, with the same diameter as the largest conductor the robot is expected to operate on, was used to simulate the power line.

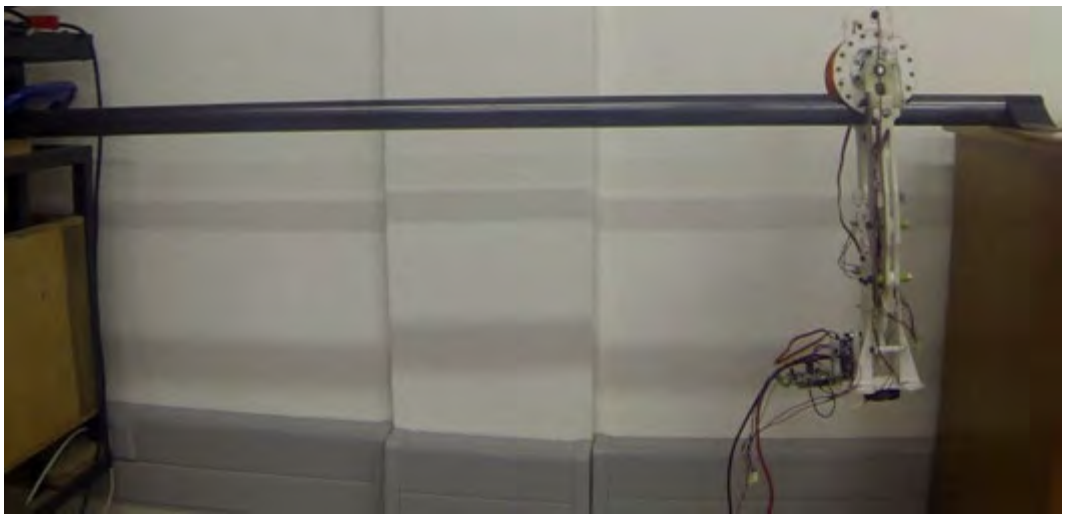

Figure 8.1: Driving test Setup

Initially, the gripper was tested on a horizontal line without any load to check whether it would be able to drive along the line. The initial and final positions of the gripper are shown in **Figure 8.2**.

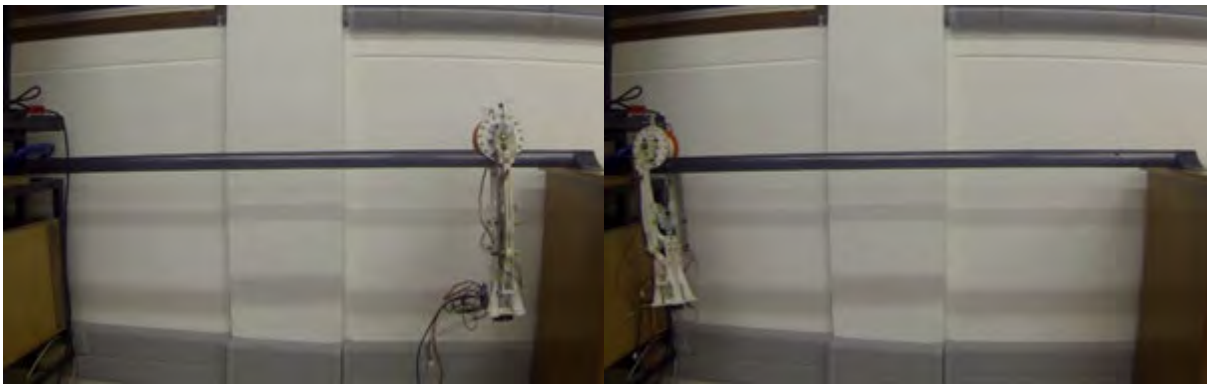

Figure 8.2: Initial and final positions of gripper during driving test

The test was successful: the gripper able to drive along the line with a speed of approximately 0.6 m/s, estimated from the video which can be found in Appendix D.

Next, the gripper was loaded with the mass of the robot which it would be supporting while driving. As discussed in Appendix C.2, it was assumed that the robot would be driven with its links in a position such that each gripper would support half the total weight of the robot. By equally distributing the weight of the robot each gripper has the same total tractive force, allowing both grippers to drive at equal speeds and preventing one gripper from slipping due to lack of traction.

The total mass of the robot is 7.4 kg, from **Table 3.3**, so each gripper would support a mass of 3.7 kg. The gripper has a mass of approximately 1 kg, therefore an additional mass of 3 kg was added to simulate the mass of the robot. The gripper with attached loads, is shown in **Figure 8.3**.

Figure 8.3: Gripper with simulated robot mass

The gripper was able to drive along the line with a speed of approximately 1 m/s, estimated from the video which can be found in Appendix D. This increased speed was due to the additional mass generating more traction on the drive wheels of the gripper.

After proving that the fully loaded gripper was capable of driving along a horizontal line, its ability to drive up an inclined line was tested. The gripper was tested on a line inclined at $10°$ from the horizontal and was able to drive along the line with a speed of approximately 0.12 m/s, estimated from the video which can be found in Appendix D.

Finally, the gripper was tested on a line inclined at $15°$ from the horizontal as shown in **Figure 8.4**.

Figure 8.4: Driving test showing line at $15°$ slope

The gripper was only able to drive halfway up the line with an approximate speed of 0.07 m/s, estimated from the video which can be found in Appendix D. The drive wheel intermittently slipping until, halfway up the line, it slipped and shredded the rubber coating that was applied to increase the traction between the half-pulley and the line. At this point the traction decreased further since the rubber coating had worn through and the smooth ABS of the pulley was now in contact with the line, thus leaving the gripper stranded halfway up the line.

A summary of the results is shown in **Table 8.1**.

Table 8.1: Summary of driving test results

Incline	Speed (m/s)
$0°$	1
$10°$	0.12
$15°$	0.07

Results discussion

The requirements for driving ability of the robot, outlined in Chapter 4.1.2, were that the robot be capable of

- Driving at 1 m/s along a horizontal conductor
- Driving up an inclined conductor with a maximum slope of $30°$

Therefore, the design of the gripper met the first requirement since it was able to drive along the horizontal line at 1 m/s.

The second requirement was however not met, since the gripper was only capable of driving up an incline of $15°$. The failure to meet the requirement can be attributed to an incorrect assumption of the static friction coefficient and poor coupling between the half-pulleys. The low speed suggests that there is also a lack of traction on the half-pulleys.

The coefficient of static friction, which determines the total tractive force that can be applied as explained in Appendix C.2, was incorrectly assumed. A coefficient of 0.6 was assumed between the rubber-coated half-pulleys and the line. However, in reality this coefficient was much lower. Since the robot was only able to drive up a $15°$ incline, the coefficient of static friction is approximately half the assumed value, thus 0.3. It should be noted that there would be more friction on a power line due to the lay (i.e. strands) and the performance of the gripper would have been improved by testing on a power line instead of a steel tube.

Further, while the rubber coating spray used on the half-pulley increased the traction of the pulleys, the coating has poor durability as it was easily torn when the drive wheel slipped. A more reliable coating method, such as lagging of the pulley in a conductive rubber is a better option for coating and this would need to be properly engineered in a production version of the robot.

Lastly, the coupling between the half-pulleys was achieved by using a half-cut squash ball pressed into the recess of the drive half-pulley. While this worked at low torque, at higher torque the coupling is poor and the torque is not equally transmitted across the half-pulleys. This is evident from the fact that only the drive half-pulley's coating was stripped. Thus, a better coupling method, or driving of both half-pulleys would be better for the final design of the robot.

8.1.2 Load testing

The gripper was designed to grip onto the conductor without rolling or sliding during brachiation. It must therefore be capable of withstanding the maximum dynamic reaction forces experienced during a brachiation swing. The dynamic reaction forces, discussed in Chapter 3.2, can be found in Appendix B.

The dynamic reaction force during the vibrational damper brachiation swing is shown in **Figure 8.5**.

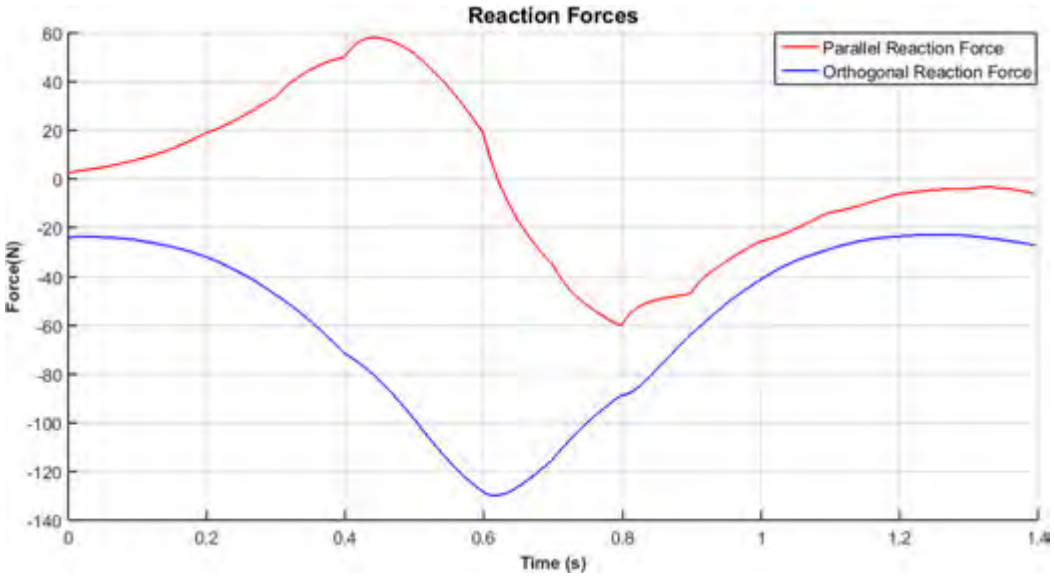

Figure 8.5: Dynamic reaction force during vibration damper brachiation calculated via double pendulum model with constraints

The dynamic reaction force has two components, a parallel component which acts to roll or slide the gripper and an orthogonal component which acts to pull the gripper off the line. The loading tests were restricted to testing the effect of the orthogonal component of the dynamic reaction force since the gripper detaching from the line is the worst-case scenario.

The test setup for the gripper load test is shown in **Figure 8.6**. A 3 kg mass along with a 1 kg spring scale for measuring the dynamic load was attached to the gripper. The dynamic force acting on the gripper during brachiation was replicated by pulling the gripper vertically downwards. The spring scale was then used to measure the magnitude of the exerted force.

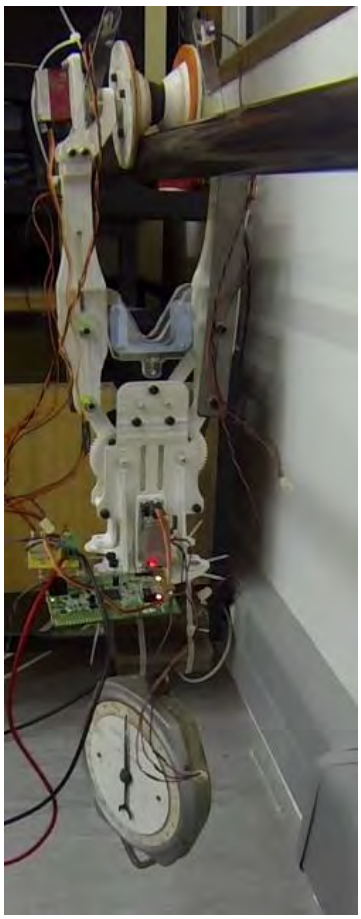

Figure 8.6: Gripper load test setup

The gripper was able to withstand a maximum orthogonal force of 180 N as shown in **Figure 8.7**. The gripper with attached weights, 3 kg mass and 1 kg spring scale, has a mass of 4 kg and the spring scale shows an exerted force of 13 kg, therefore totalling 18 kg of load. The gripper load test videos can be found in Appendix D.

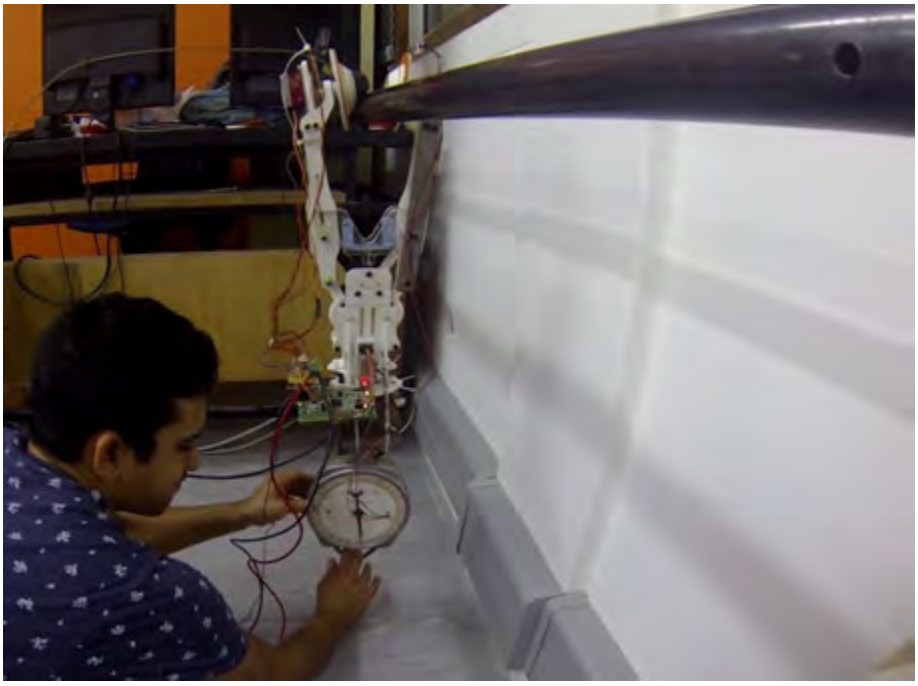

Figure 8.7: Gripper load test showing maximum gripper orthogonal force.

Results discussion

The gripper is the only connection between the robot and the conductor during brachiation and therefore its ability to withstand the dynamic reaction force is paramount. The maximum orthogonal component of the dynamic reaction force for different brachiation scenarios is summarised in **Table 8.2**.

Table 8.2: Maximum orthgonal reaction force in brachiation scenarios

Brachiation Scenario	Slope (°)	Maximum Orthogonal Reaction Force (N)
Vibration damper	0	130
Swing-up	0	265
Jumper-to-main conductor	45	275

In the load tests, the gripper was capable of withstanding a load of 180 N. This means that the gripper would be able to withstand the loading during a vibration damper brachiation swing. However, the maximum load experienced during swing up and a jumper-to-main conductor brachiation swing exceed the gripper's load capability and would detach the gripper from the line.

The gripper's maximum load capability was not limited by its strength but rather by the deflection of the structure as shown in **Figure 8.7**. This is evident from the fact that gripper did not break when 180 N was exceeded but rather, simply fell from the line.

The four-bar mechanism of the gripper was designed to close with increased load, locking the gripper onto the line, creating a fail-safe mechanism. However, since the gripper's components were 3D printed from ABS and PLA plastic, which has a Young's Modulus of approximately 2.3 GPa [50], they are relatively flexible and therefore suffer from large deflections under load.

As the robot in this project was a prototype, despite the gripper failing to meet the required maximum orthogonal load capability, the design of the gripper was verified. The final robot's gripper would be

made from aluminium and steel for critical parts. Aluminium 6082-T6 is approximately 2.6 times heavier than ABS but has a far higher yield strength, 240 MPa [61] compared to 44 MPa [50] for ABS and therefore the geometry of the components can be smaller, yielding a design with approximately equal weight. Further, it has a Young's Modulus of 70 GPa [61], which is approximately 30 times greater than ABS, thus the deflection of the gripper would be negligible.

8.2 iNemo vibrational noise

Before the performance of the EKF attitude estimation algorithm could be tested, the quality of the IMU measurements first had to be tested.

It was noticed that while the robot was on the line, and the gripper actuation servo was actively keeping the gripper closed, the mechanical vibrations of the gripper caused the IMU's to vibrate. Thus, the data from the IMU's were noisy making the attitude estimation unreliable.

To analyse the effect of the servo vibrations on the IMU data, the two IMU's were mounted orthogonally on the same robot link as shown in **Figure 8.8**.

Figure 8.8: IMU's mounted orthogonally on robot link

Two mounting schemes were compared to analyse the effect of the IMU mounting scheme in relation to the servo vibrations. The IMU's were first mounted rigidly on the link and then mounted on soft polyurethane rubber to dampen the vibrations. The two mounting schemes can be seen in **Figure 8.9**. A comparison of the IMU data quality for the two mounting schemes is shown in **Figure 8.10**.

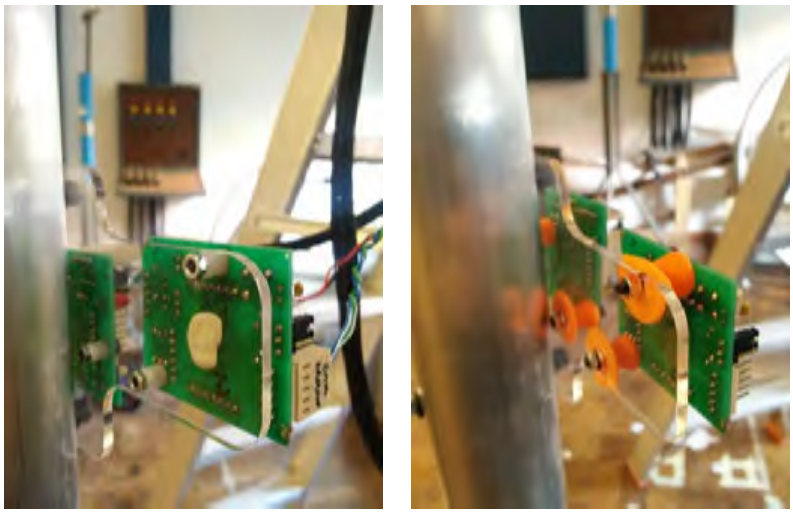

Figure 8.9: IMU mounting scheme. Left, rigid mounting of IMU to link. Right, IMU's mounted on soft polyurethane rubber.

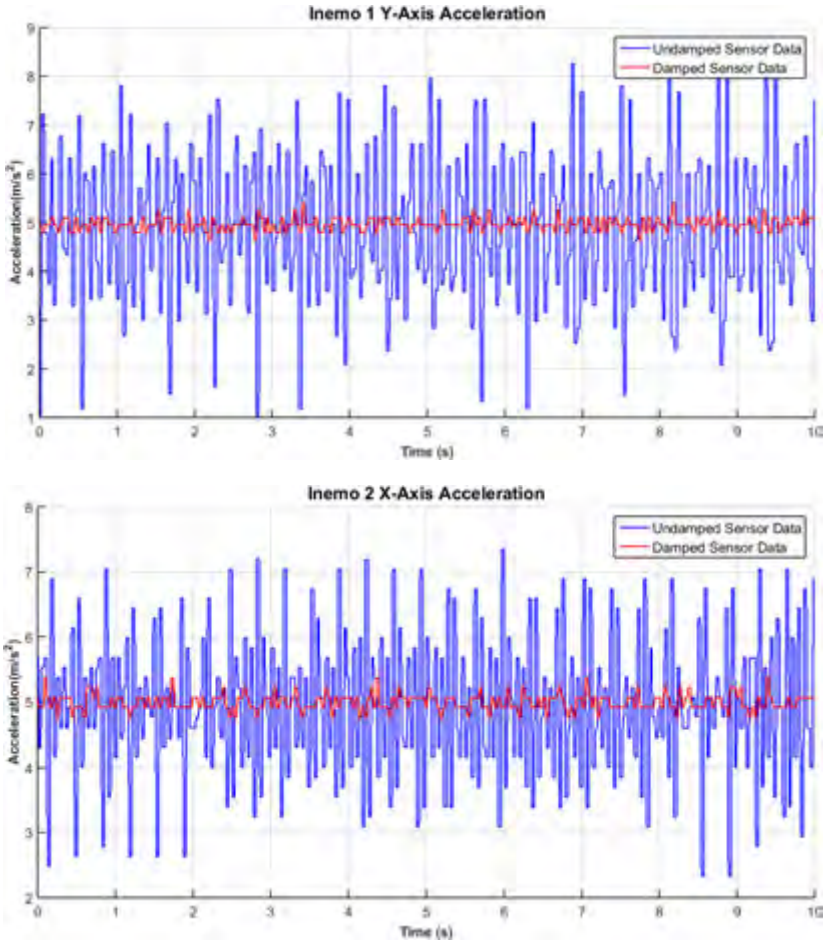

Figure 8.10: IMU data before and after vibration damping. The robot is statically positioned such that $\theta_1 = 4.4°$ and $\theta_2 = 138°$, and the two IMU's are mounted orthogonally.

It was first thought that the noisy data of the undamped IMU's, seen in **Figure 8.10**, was due to electrical noise. Thus, decoupling capacitors, to filter both high and low frequency noise, were added. However, the noise remained, indicating that it was not due to electrical interference.

The movement of the IMU due to the mechanical vibrations of the servo motor was then analysed. Using the fast Fourier transform, a noise signal with an approximate frequency of 56.5 rad/s was identified. From the undamped IMU data, the RMS acceleration amplitude was determined to be 1.6 $\mathrm{m/s^2}$. Assuming sinusoidal motion of the IMU, the acceleration of the IMU can be calculated as

$$a = d{\omega_f}^2 \sin \omega t \tag{8.1}$$

where, a is the acceleration amplitude, d is the displacement, ω_f is the frequency and t is the time. Thus the movement of the IMU is

$$d = \frac{a}{{\omega_f}^2} = \frac{1.6}{(56.5)^2} = 0.5 \text{ mm} \tag{8.2}$$

These small oscillations of the IMU, caused by the servo vibrations, would be unnoticeable but result in noisy and unreliable data. Thus, the IMU's required mechanical damping to eliminate the effect of the servo vibrations.

From **Figure 8.10**, it can be seen that the effect of the servo vibrations i.e. the noise of the IMU's, was reduced by mounting the IMUs on polyurethane rubber. Additionally, the rubber only dampens high frequency vibrations but does not affect the data quality of the lower frequency movements, such as the actual swinging of the robot link.

8.3 EKF attitude estimation

The EKF attitude estimation algorithm was tested to ensure its performance and to verify the tuning of the variances for optimal tracking.

The EKF was tested using the same method as in the friction estimation test of Chapter 6.2. The test was performed by starting the robot from some arbitrary position on the conductor. The gripper was then opened and the robot allowed to swing freely until it came to rest.

The EKF's estimate of the angles θ_1 and θ_2 was compared to the reference angles measured using the potentiometer and motor encoder. The results of the EKF test are shown in **Figure 8.11**.

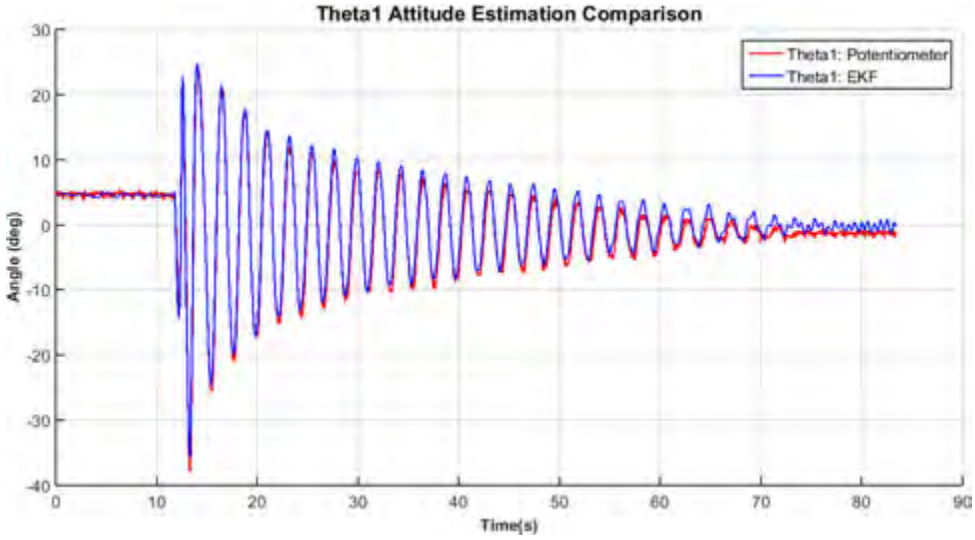

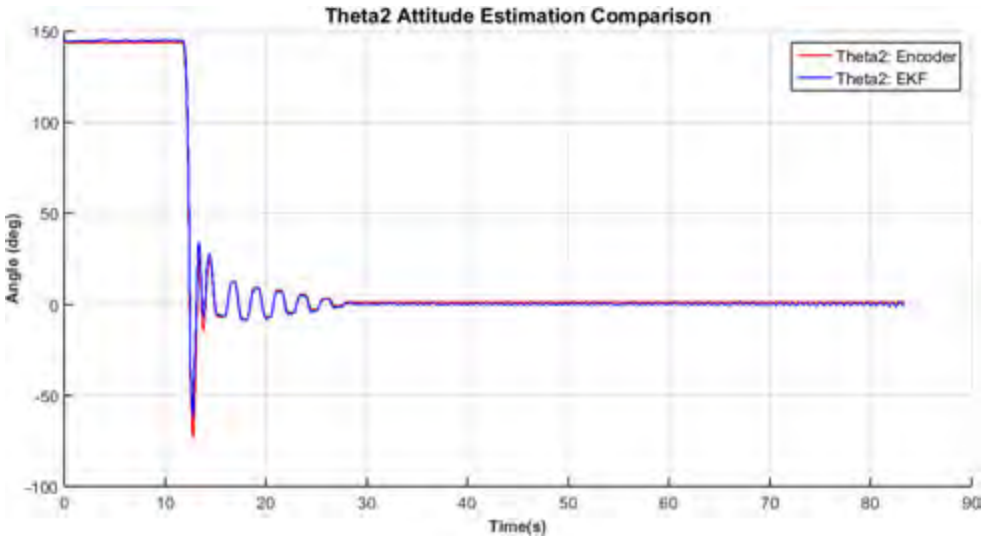

Figure 8.11: EKF attitude estimation

Results discussion

The accuracy of the EKF algorithm in estimating the robot's state affects the control of the robot as incorrect state estimation will lead to incorrect control actions being applied and thus failure to brachiate successfully.

From **Figure 8.11**, the EKF was able to track the reference angles accurately, albeit with some discrepancies. The oscillations of the EKF's estimate of θ_1 slightly overshoot the potentiometer's estimate, this can be attributed to slipping of the coupling between the potentiometer and link 1 of the robot. Also, the EKF's estimate of θ_1 tends to oscillate with much higher amplitude at the end of swing, 70 – 80 s, this is most likely due to the robot still oscillating, the damping in the potentiometer reducing the effect on its estimate. Finally, the EKF's estimate of θ_2 slightly undershoots at the beginning of the swing, this is most likely due to the robot swinging slightly out-of-plane and since the EKF assumes strictly planar motion, its estimate is slightly inaccurate.

The EKF algorithm presented in this dissertation is a basic version of the EKF algorithm which would be implemented on the final robot. The final EKF algorithm would account for gyroscope and accelerometer drift as well as modelling the robot in 3-dimensions, which would account for any out-of-plane motion experienced during a swing. Therefore, while the EKF algorithm presented in this dissertation is basic, it shows the ability to accurately estimate the robot's state.

8.4 Position control

The final preliminary test was a position control test. The position control test is the first real test of the robot's controller. Further, the position control test provides insight into the performance of the trajectory tracking since trajectory tracking is essentially position control with time-varying set points. Videos of the position control test can be found in Appendix D.

The test setup for the position control test is shown in **Figure 8.12**. The robot was started with both its link as near to vertical as possible. A position command in the form of a θ_2 set point step is then given.

Figure 8.12: Initial and final positions for position control test

The results for the position control tests are shown in **Figure 8.13**. Three different set points $10°$, $20°$ and $40°$ were tested. As discussed in Chapter 7.4, the initial value of θ_2 is non-zero since the friction in the joint made it difficult to position the link perfectly vertical. Despite θ_2 being non-zero the results are still valid since the initial angle is arbitrary, the emphasis being on the robot's position control capabilities. From **Figure 8.13**, it can be seen that the controller was able to accurately command the position of the robot's link to within an acceptable region of the set point.

The controller has an approximate rise time of 120 ms with a maximum overshoot of approximately 10 %, in the case of the 40° set point. The oscillations of θ_2 are from the effect of the dither signal, which is always active. The steady state error for each set point is shown in **Table 8.3**.

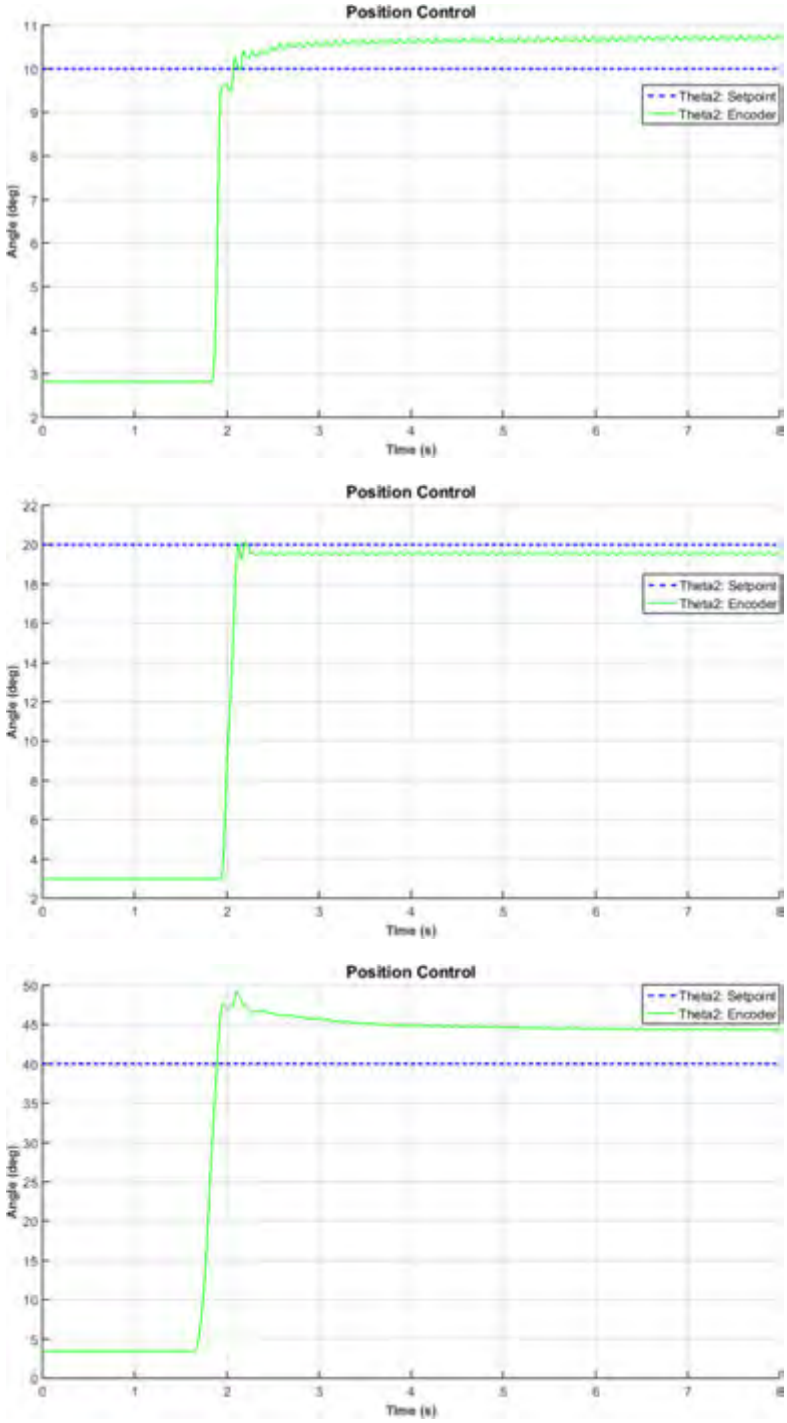

Figure 8.13: Position control results for $10°$, $20°$ and $40°$ steps

Table 8.3: Steady-state error for different position set points

Set Point (°)	Steady-state Error (°)	Time Constant (ms)
10	0.6	70
20	0.4	110
40	4.6	180

Results discussion

The results of the position control test proved that accurate position control is possible and that the trajectory tracking while brachiating would be successful.

The controller exhibits fast response, which is crucial for the trajectory tracking. The response time and steady-state error could be improved by increasing the low frequency gain of the system, but this would also increase the overshoot and system oscillations which is undesirable.

The behaviour of the robot varies with different position set points revealing that the PFL mapping was unable to linearise the system perfectly and nonlinearities still exist. The PFL mapping is state dependent and therefore any error in the state measurements will result in a failure to linearize the system. Moreover, modelling errors or un-modelled dynamics such as the oscillation of the line could possibly contribute to the linearization failure. Despite this, the controller's performance is still deemed satisfactory.

Further, the controller is capable of accurate position control at relatively low set points due to the dither signal overcoming the static friction, thereby improving its performance.

Chapter 9

Brachiation Testing

The final and most important test was a vibration damper brachiation manoeuvre. The ability of the robot to brachiate is paramount to its industrial viability.

Test setup

The initial position of the robot was defined by the optimal initial conditions from the trajectory generation and is shown in **Figure 9.1**. This position allows the robot to maximise its potential energy which can then be traded for kinetic energy in the swing, ending in a position with a lower potential energy.

The maximum height to which the COM can be raised was limited by the size of the circuitry on link 1, as in this position, the circuitry was in contact with the line.

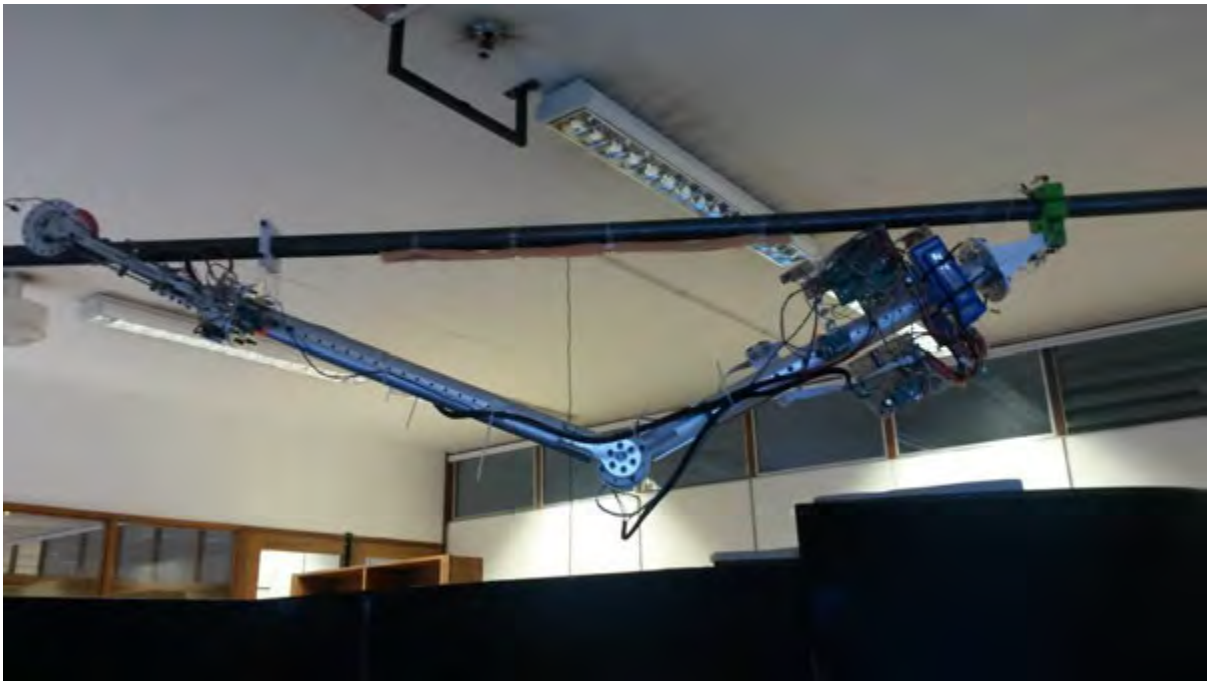

Figure 9.1: Initial position of robot for brachiation test

The robot was held in this initial position by a clamp as shown in **Figure 9.2**. Although the link actuation motor could be used to constrain the robot in this position, it was simpler to use a clamp as any problems with the link actuation motor's control could damage the robot's gripper, ending the test prematurely.

Figure 9.2: Clamp constraining robot in initial position

A layer of foam was added to the line to cushion any impact between the gripper and the line at the end of the swing.

Robot operation

The high level operation of the robot during the brachiation manoeuvre is shown in **Figure 9.3**. The robot is powered up and then initialises the various sub-systems, calculates its current state and initialises its angles. After this, the robot waits until an activation switch is flipped to signal the start of the brachiation manoeuvre.

A delay is imposed to allow the operator to be clear of the robot. The gripper is then opened allowing the robot to begin brachiation. However, there is a variable delay between the time the gripper opening command is sent and the time the robot starts falling from the line due to friction between the half-pulleys and the line, and the constraint clamp.

In order to determine when the robot has actually released the line an algorithm to determine the relative change in height of the robot was implemented. When the height of the robot has changed by a set amount, the robot is determined to be in free fall. This step is necessary in order to prevent the link actuation motor from actuating while the gripper is still on the line as this would damage the gripper.

At this point a trajectory fast forwarding algorithm is implemented since the reference trajectory begins with the robot on the line whereas the actual position of the robot is now off the line. Therefore the reference trajectory is advanced in relation to the robot's actual position. This was done by calculating the actual height of the robot's end-effector and comparing it to the end-effector height in the reference trajectory.

The trajectory tracking then starts, the robot brachiating until it detects the presence of the line at which time the gripper is closed and the manoeuvre ends.

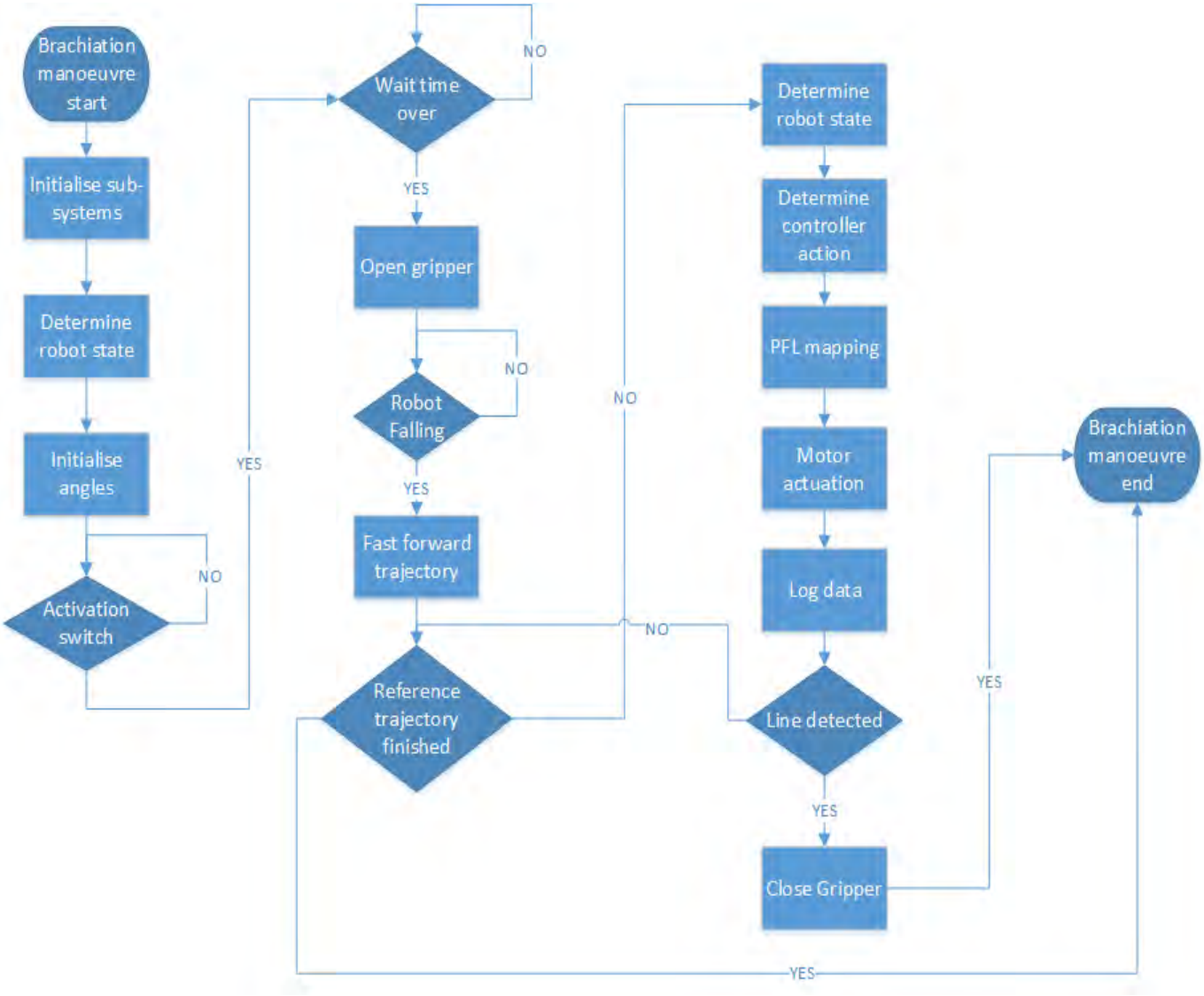

Figure 9.3: High-level software flow diagram of brachiation manoeuvre

Results

The robot was able to brachiate successfully as illustrated in **Figure 9.4**. Videos of the robot's brachiation swings can be found in Appendix D.

However, not all of the brachiation attempts were successful. It was noticed that the gripper closed too slowly at the end of the swing, meaning that in some attempts, the robot failed to catch onto the line.

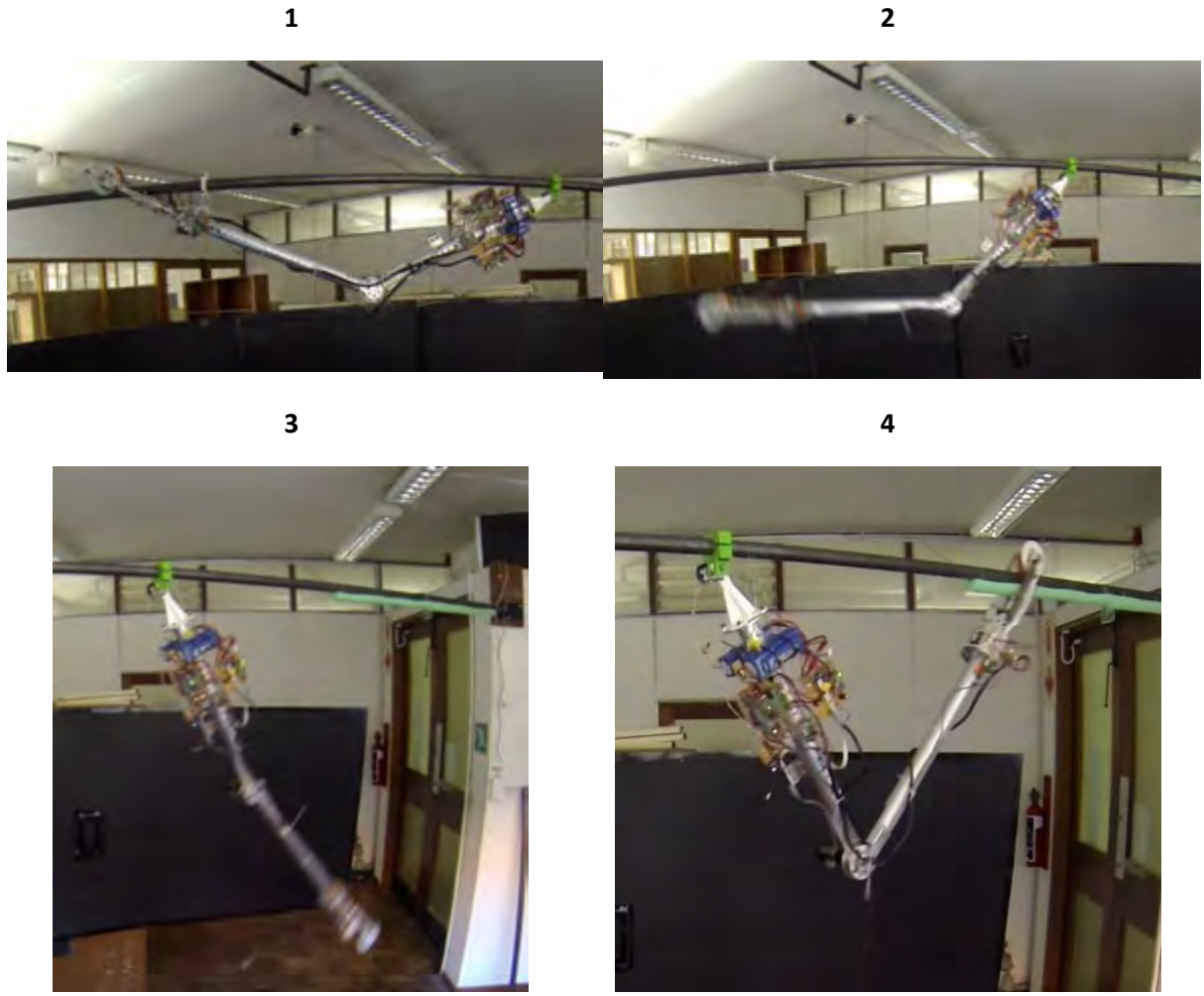

Figure 9.4: Brachiation sequence for negotiating vibration damper on power line

The results of a successful brachiation swing are shown in **Figure 9.5**. From **Figure 9.5**, it can be seen that the robot was able to track the reference trajectory successfully albeit not with the same accuracy as the simulations. At approximately 1.25 s, the robot's gripper collides with the foam placed under the line and the gripper catches onto the line. After this point the robot's height remains constant but the angles change slightly since the robot momentarily slides along the line with the gripper squeezing the line until it finally comes to rest.

Further, it was noticed that the robot brachiated slightly out-of-plane due to the robot's link not being perfectly straight and the deflection of the replacement gripper.

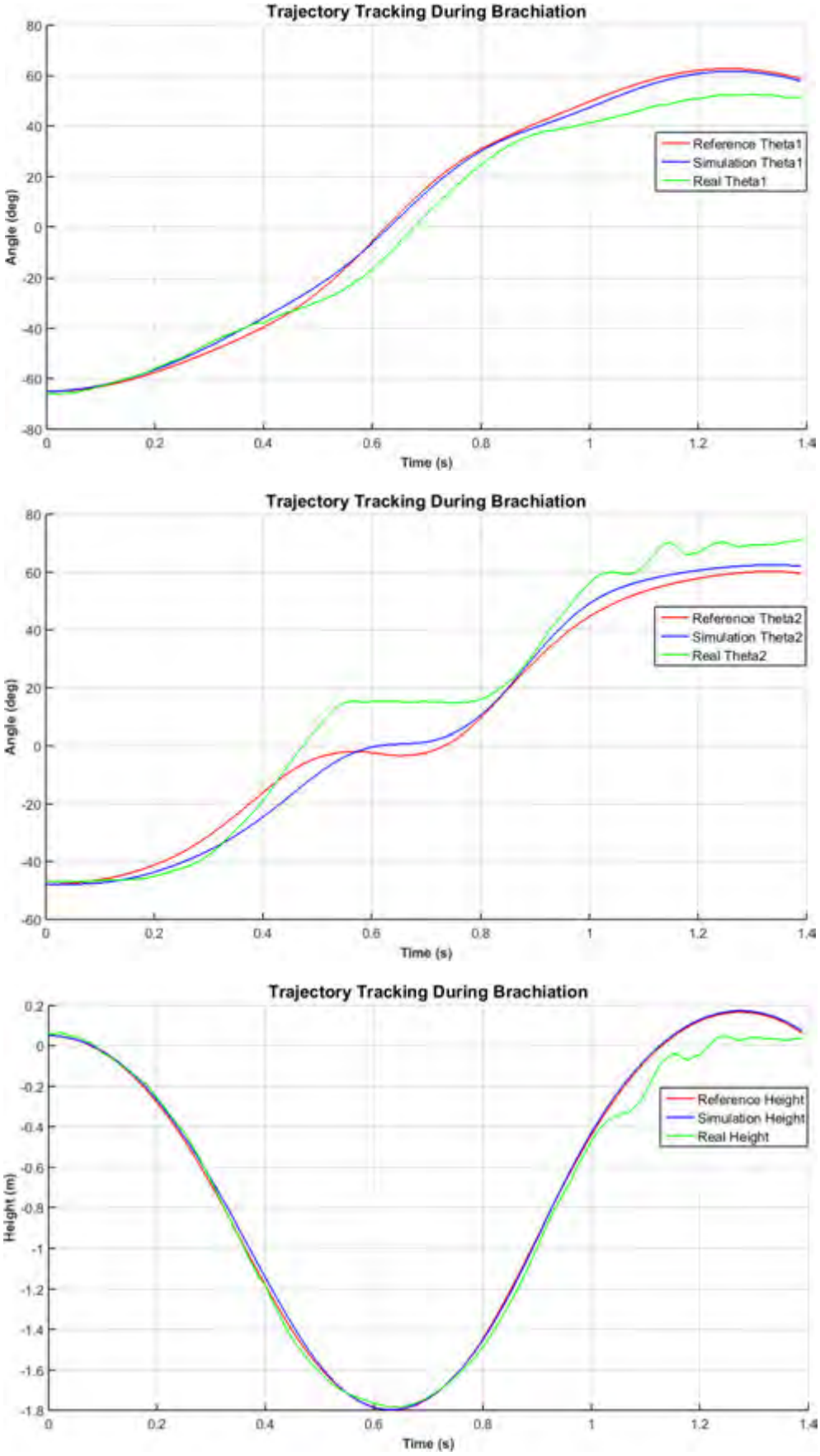

Figure 9.5: Vibration damper brachiation test results

Results discussion

The results show that the robot is capable of performing brachiation and would be able to successfully negotiate around a vibration damper and other similar obstacles such as spacer dampers and suspension clamps.

The discrepancy between the simulation's trajectory tracking and the real robots' can be associated with the effect of a number of factors, namely:

- Incorrect friction coefficient. Even though the friction coefficients were estimated as accurately as possible in the friction estimation test of Chapter 6.2, the real and simulated system still varied slightly.
- Error in attitude estimation. Sensor noise results in small errors in the attitude estimation.
- The initial position of the robot is slightly different to the optimal and simulation's initial position due to difficulty of constraining the robot in the precise position. The robot's initial position was constrained to be within 1° of the optimal position.
- Advancing the trajectory incorrectly. Since the trajectory is advanced based on measurements, if these measurements are slightly off or if the robot moves during this calculation the trajectory will be advanced incorrectly.
- Non-planar motion of robot. The simulation and reference trajectory assumed that the robot brachiates strictly in-plane but the actual brachiation swing was non-planar. In a product version, the stiffness of the gripper's components would be increased and be of a higher tolerance, limiting deflection and non-planar motion.
- Plant uncertainty. If the estimated robot parameters are incorrect, the dynamics of the plant will change. Further, the PFL will not be able to perfectly linearize the system since it depends on perfectly known (i.e. certain) parameters.

Despite these factors, the robot was still able to brachiate successfully, proving its robustness.

The factor which most affected the ability of the robot to brachiate was the closing speed of the gripper. The failure of the gripper to close fast enough was the main reason that many brachiation attempts failed. The grippers' closing speed was designed in Chapter 4.1.2, but this assumed that the gripper would fall vertically, whereas the gripper actually falls while at some angle reducing the clearance and hence the time available to close the gripper. This problem can be fixed (i) by changing the gripper design to allow a faster closing speed, (ii) by spring loading the gripper or (iii) by pre-actuating the gripper using the measurement of the robot's height from the state estimator.

Finally, overshoot was designed into the trajectory to ensure that there is actuation available to slow the gripper down at the end of the swing but also to allow some margin in case the friction (wind loading, etc.) is more than expected. This overshoot results in the robot's gripper colliding with the line at the end of the swing. While this collision is minor and no major damage resulted from the collision, implementing the non-collocated PFL, discussed in Chapter 7.1, would allow the gripper to control its distance to the line precisely. Thus the robot would be able to avoid the collision and this would also give the gripper a better chance to close over the line since the robot would be moving slower as it approached the line.

Chapter 10

Conclusions and Future Work

This dissertation has presented the development of a prototype industrial brachiation robot for the inspection of high-voltage power lines. The robot is mechanically simple and capable of performing brachiation to negotiate obstacles, which is an improvement over current line inspection platforms which are mechanically complex and employ slow, energy inefficient static schemes for obstacle negotiation.

The prototype was developed using a multi-disciplinary research approach, which incorporated elements of mathematical modelling, numerical optimisation, mechanical and electrical design theory as well as feedback controller design and implementation on a physical robot.

In order to simulate the robot, mathematical models were derived using the Euler-Lagrange modelling technique in Chapter 2. A detailed model which incorporated constraints allowed for the analysis of the dynamic reaction forces which were used in the mechanical design. A nonlinear optimisation technique used to generate energy optimal trajectories for negotiating obstacles on the line was presented in Chapter 3. The optimisation technique, while simple, proved to be capable of generating feasible trajectories which respected the physical constraints of the robot.

In Chapter 4 and 5 the mechanical and electrical design of the robot was presented. Fundamental mechanical design principles were followed in order to develop simple and robust mechanisms capable of achieving the desired performance. The electronic and control system design focused on the development of key areas of the robot's operation such as attitude estimation, data logging and power line sensing.

The physical robot was manufactured and assembled and a 3-stage system identification discussed in Chapter 6 was performed, in order to characterise the system and capture the plant uncertainty. The design of the controller was presented in Chapter 7, where a partial feedback linearization approach coupled with a PID controller was proposed for controlling the robot. The simulations of the controller showed its ability to brachiate successfully in the presence of plant uncertainty.

To ensure the success of the robot preliminary tests were performed in Chapter 8. These tests included the testing of the gripper's driving and load capabilities, EKF attitude estimation and position control which served as the basis for the trajectory tracking performed in the brachiation test.

Finally, the brachiation of the robot was tested in Chapter 9. The results of the test showed that the robot is capable of brachiating even in the presence of plant uncertainty.

10.1 Future work

The robot in this dissertation is a prototype and therefore still requires further development to create an industrially useful robot. The main areas for development are discussed below.

Trajectory generation

The optimal trajectory serves as a reference for the robot during brachiation manoeuvres and therefore has a major impact on the robot's success.

The optimal trajectories were generated using a single-shooting nonlinear optimisation method as discussed in Chapter 3. However, the use of multiple shooting methods and direct collocation may result in trajectories which are more energy optimal. By developing lower energy trajectories, a lower power link mechanism actuator can be used, reducing the weight of the robot.

Additionally, the implementation of online trajectory generation could vastly improve the robot's industrial viability since it would be capable of dealing with unexpected scenarios.

Mechanical design

The mechanical design of the robot is the area which requires the most development.

The gripper's load capability could be improved by manufacturing the gripper components from metal instead of using 3D printing. The use of metal will increase the stiffness of the gripper which was determined to be the limiting factor of its load capability. Further, the gripper's driving ability could be improved by implementing a better coupling mechanism for the half-pulleys or driving both half-pulleys with motors.

The implementation of a mechanism to move the robot's payload would decrease the torque requirements for brachiation as seen in Chapter 3. This mechanism could be implemented by placing the robot's payload on a leadscrew, allowing the robot to re-position the payload before each swing. Thus, a lower power actuator could be used for brachiation.

In terms of link actuation, the implementation of an elastic actuation method would enable the use of lower power actuators thus reducing the weight of the robot allowing it to carry heavier payloads or operate for longer.

Control design

The control of the robot could be improved by implementing the non-collocated PFL mapping. This would allow the robot to control the height of its free gripper thus preventing the collisions between the gripper and the line.

Speed control of the gripper half-pulley motor could be implemented to prevent wheel slip while driving up an incline. As the wheel slips, a speed controller could adjust the speed allowing the wheel to regain traction instead of constantly slipping as was seen in the gripper tests of Chapter 8.

Electrical design

The printing of a circuit board or the relocation of the circuitry would allow the robot to raise its COM further, as the size of the circuitry and its placement were the limiting factor for the robot's initial position as discussed in Chapter 9.

The performance of the link actuation motor could be improved by using a motor controller which doesn't have as many safety limits, thus extracting more performance from the motor, albeit with increased risk of motor failure.

Appendix A

Dynamic Models

A.1 Double Pendulum

The double pendulum is modelled using the Euler-Lagrange technique. The generalised coordinates for the double pendulum modelling are shown in **Figure A.1**, where the state vector, q, is chosen as

$$q = (\theta_1, \theta_2)^T \tag{A.1}$$

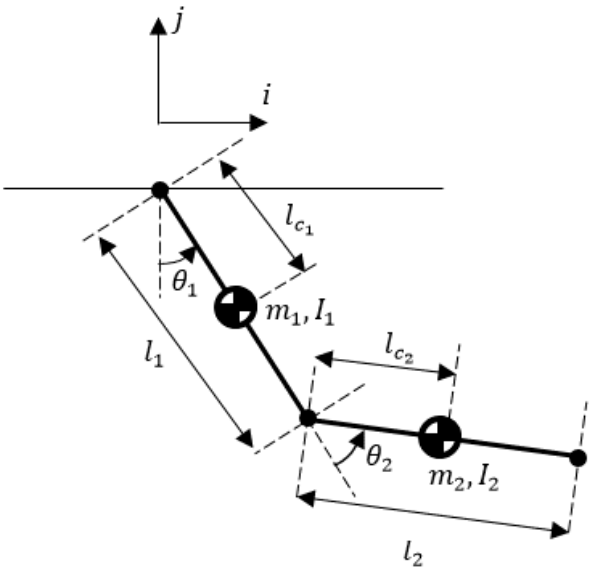

Figure A.1: Generalised coordinates of double pendulum robot configuration

The coordinates of the COM of each rigid beam i_1, j_1, i_2 and j_2 can then be expressed as

$$i_1 = l_{c_1}\sin\theta_1 \tag{A.2}$$

$$j_1 = -l_{c_1}\cos\theta_1 \tag{A.3}$$

$$i_2 = i_1 + l_{c_2}\sin(\theta_1 + \theta_2) \tag{A.4}$$

$$j_2 = j_1 - l_{c_2}\cos(\theta_1 + \theta_2) \tag{A.5}$$

The dynamics can be expressed in the standard manipulator form as

$$\begin{bmatrix} m_{11} & m_{12} \\ m_{21} & m_{22} \end{bmatrix}\begin{bmatrix} \ddot{\theta}_1 \\ \ddot{\theta}_2 \end{bmatrix} + \begin{bmatrix} c_{11} & c_{12} \\ c_{21} & c_{22} \end{bmatrix}\begin{bmatrix} \dot{\theta}_1 \\ \dot{\theta}_2 \end{bmatrix} + \begin{bmatrix} G_1 \\ G_2 \end{bmatrix} = \begin{bmatrix} B_1 \\ B_2 \end{bmatrix}\tau + \begin{bmatrix} F_1 \\ F_2 \end{bmatrix} \tag{A.6}$$

$$m_{11} = m_2 l_1^2 + 2m_2 \cos\theta_2 l_1 l_{c_2} + m_1 l_{c_1}^2 + m_2 l_{c_2}^2 + I_1 + I_2$$

$$m_{12} = m_2 l_{c_2}^2 + l_1 l_{c_2} m_2 \cos\theta_2 + I_2$$

$$m_{21} = m_{11}$$

$$m_{22} = m_2 l_{c_2}^2 + I_2$$

$$c_{11} = -\dot{\theta}_2 l_1 l_{c_2} m_2 \sin\theta_2$$

$$c_{12} = -l_1 l_{c_2} m_2 \sin\theta_2 (\dot{\theta}_1 + \dot{\theta}_2)$$

$$c_{21} = -\dot{\theta}_1 l_1 l_{c_2} m_2 \sin\theta_2$$

$$c_{22} = 0$$

$$G_1 = m_2 g\left(l_{c_2}\sin(\theta_1 + \theta_2) + l_1 \sin\theta_1\right) + g l_{c_1} m_1 \sin\theta_1$$

$$G_2 = m_2 g l_{c_2}\sin(\theta_1 + \theta_2)$$

Since the robot only has an actuator at the elbow, the actuation matrix B evaluates to

$$B = \begin{bmatrix} 0 \\ 1 \end{bmatrix} \tag{A.7}$$

A.2 Double Pendulum with constraints

The double pendulum model with constraints is shown in **Figure A.2**. The constraints are imposed on the system in the form of redundant variables. The state vector, q, is chosen as

$$q = (x, y, \theta_1, \theta_2)^T \tag{A.8}$$

where x and y are the redundant variables used to impose the constraints.

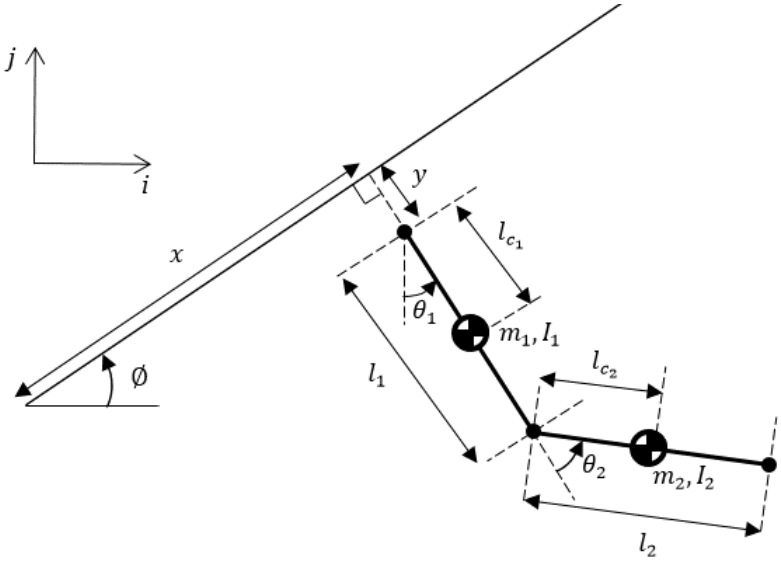

Figure A.2: Generalised coordinates of double pendulum robot configuration with constraints

The coordinates of the COM of each rigid beam i_1, j_1, i_2 and j_2 can be expressed as:

$$i_1 = x\cos\emptyset + y\sin\emptyset + l_{c_1}\sin\theta_1 \tag{A.9}$$

$$j_1 = x\sin\emptyset - y\cos\emptyset - l_{c_1}\cos\theta_1 \tag{A.10}$$

$$i_2 = i_1 + l_{c_2}\sin(\theta_1 + \theta_2) \tag{A.11}$$

$$j_2 = j_1 - l_{c_2}\cos(\theta_1 + \theta_2) \tag{A.12}$$

The dynamics can then be expressed in the standard manipulator form as

$$\begin{bmatrix} m_{11} & m_{12} & m_{13} & m_{14} \\ m_{21} & m_{22} & m_{23} & m_{24} \\ m_{31} & m_{32} & m_{33} & m_{34} \\ m_{41} & m_{42} & m_{43} & m_{44} \end{bmatrix} \begin{bmatrix} \ddot{x} \\ \ddot{y} \\ \ddot{\theta}_1 \\ \ddot{\theta}_2 \end{bmatrix} + \begin{bmatrix} c_{11} & c_{12} & c_{13} & c_{14} \\ c_{21} & c_{22} & c_{23} & c_{24} \\ c_{31} & c_{32} & c_{33} & c_{34} \\ c_{41} & c_{42} & c_{43} & c_{44} \end{bmatrix} \begin{bmatrix} \dot{x} \\ \dot{y} \\ \dot{\theta}_1 \\ \dot{\theta}_2 \end{bmatrix} + \begin{bmatrix} G_1 \\ G_2 \\ G_3 \\ G_4 \end{bmatrix} = \begin{bmatrix} B_1 \\ B_2 \\ B_3 \\ B_4 \end{bmatrix} \tau + \begin{bmatrix} F_1 \\ F_2 \\ F_3 \\ F_4 \end{bmatrix} + \begin{bmatrix} A_{11} & A_{12} & A_{13} & A_{14} \\ A_{21} & A_{22} & A_{23} & A_{24} \end{bmatrix} \lambda \tag{A.13}$$

$$m_{11} = m_1 + m_2$$

$$m_{12} = 0$$

$$m_{13} = l_{c_2} m_2 \cos\beta + l_1 m_2 \cos\alpha + l_{c_1} m_1 \cos\alpha$$

$$m_{14} = l_{c_2} m_2 \cos\beta$$

$$m_{21} = 0$$

$$m_{22} = m_1 + m_2$$

$$m_{23} = l_{c_2} m_2 \sin\beta + l_1 m_2 \sin\alpha + l_{c_1} m_1 \sin\alpha$$

$$m_{24} = l_{c_2} m_2 \sin\beta$$

$$m_{31} = m_{13}$$

$$m_{32} = m_{23}$$

$$m_{33} = m_2 l_1^2 + 2 m_2 \cos\theta_2 l_{c_2} l_1 + m_1 l_{c_1}^2 + m_2 l_{c_2}^2 + I_1 + I_2$$

$$m_{34} = m_2 l_{c_2}^2 + l_1 m_2 \cos\theta_2 l_{c_2} + I_2$$

$$m_{41} = l_{c_2} m_2 \cos\beta$$

$$m_{42} = l_{c_2} m_2 \sin\beta$$

$$m_{43} = m_{34}$$

$$m_{44} = m_2 l_{c_2}^2 + I_2$$

$$c_{11} = c_{12} = 0$$

$$c_{13} = \dot{\theta}_1 \left(l_{c_2} m_2 \sin\beta + l_1 m_2 \sin\alpha + l_{c_1} m_1 \sin\alpha \right) + \dot{\theta}_2 l_{c_2} m_2 \sin\beta$$

$$c_{14} = l_{c_2} m_2 \sin\beta (\dot{\theta}_1 + \dot{\theta}_2)$$

$$c_{21} = c_{22} = 0$$

$$c_{23} = -\dot{\theta}_1 \left(l_{c_2} m_2 \cos\beta + l_1 m_2 \cos\alpha + l_{c_1} m_1 \cos\alpha \right) - \dot{\theta}_2 l_{c_2} m_2 \cos\beta$$

$$c_{24} = -l_{c_2} m_2 \cos\beta (\dot{\theta}_1 + \dot{\theta}_2)$$

$$c_{31} = c_{32} = 0$$

$$c_{33} = -\dot{\theta}_2 l_1 l_{c_2} m_2 \sin\theta_2$$

$$c_{34} = -l_1 l_{c_2} m_2 \sin\theta_2 (\dot{\theta}_1 + \dot{\theta}_2)$$

$$c_{41} = c_{42} = c_{44} = 0$$

$$c_{43} = \dot{\theta}_1 l_1 l_{c_2} m_2 \sin\theta_2$$

$$G_1 = g \sin\emptyset (m_1 + m_2)$$

$$G_2 = -g \cos\emptyset (m_1 + m_2)$$

$$G_3 = g m_2 \left(l_{c_2} \sin(\theta_1 + \theta_2) + l_1 \sin\theta_1 \right) + g l_{c_1} m_1 \sin\theta_1$$

$$G_4 = g m_2 \sin(\theta_1 + \theta_2)$$

The actuation matrix B evaluates to

$$B = \begin{bmatrix} 0 \\ 0 \\ 0 \\ 1 \end{bmatrix} \tag{A.14}$$

and the constraint Jacobian A, is defined as

$$A = \begin{bmatrix} 1 & 0 & 0 & 0 \\ 0 & 1 & 0 & 0 \end{bmatrix} \tag{A.15}$$

A.3 Triple Pendulum

The triple pendulum model with actuators at the elbow(link 2) and wrist (link 3) is shown in **Figure A.3**. The generalised coordinates of the system are the state vector, q, is chosen as

$$q = (\theta_1, \theta_2, \theta_3)^T \tag{A.16}$$

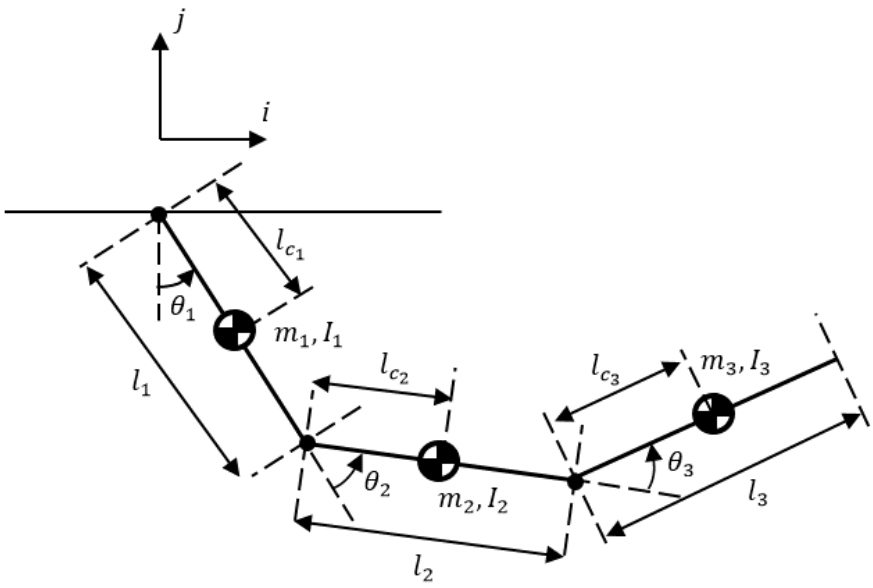

Figure A.3: Generalised coordinates of triple pendulum robot configuration

The coordinates of the COM of each rigid beam i_1, j_1, i_2, j_2, i_3 and j_3 can be expressed as:

$$i_1 = l_{c_1} \sin\theta_1 \tag{A.17}$$

$$j_1 = -l_{c_1} \cos\theta_1 \tag{A.18}$$

$$i_2 = i_1 + l_{c_2} \sin(\theta_1 + \theta_2) \tag{A.19}$$

$$j_2 = j_1 - l_{c_2}\cos(\theta_1 + \theta_2) \tag{A.20}$$

$$i_3 = i_2 + l_{c_3}\cos\left(\theta_3 + \theta_1 + \theta_2 - \frac{\pi}{2}\right) \tag{A.21}$$

$$j_3 = j_2 - l_{c_3}\sin\left(\theta_3 + \theta_1 + \theta_2 - \frac{\pi}{2}\right) \tag{A.22}$$

The dynamics of the triple pendulum can be written as

$$\begin{bmatrix} m_{11} & m_{12} & m_{13} \\ m_{21} & m_{22} & m_{23} \\ m_{31} & m_{32} & m_{33} \end{bmatrix} \begin{bmatrix} \ddot{\theta}_1 \\ \ddot{\theta}_2 \\ \ddot{\theta}_3 \end{bmatrix} + \begin{bmatrix} c_{11} & c_{12} & c_{13} \\ c_{21} & c_{22} & c_{23} \\ c_{31} & c_{32} & c_{33} \end{bmatrix} \begin{bmatrix} \dot{\theta}_1 \\ \dot{\theta}_2 \\ \dot{\theta}_3 \end{bmatrix} + \begin{bmatrix} G_1 \\ G_2 \\ G_3 \end{bmatrix} = \begin{bmatrix} B_1 \\ B_2 \\ B_3 \end{bmatrix} \tau + \begin{bmatrix} F_1 \\ F_2 \\ F_3 \end{bmatrix} \tag{A.23}$$

$$\begin{aligned} m_{11} = {} & m_2 l_1^2 + m_3 l_2^2 + m_1 l_{c_1}^2 + m_2 l_{c_2}^2 + m_3 l_{c_3}^2 + 2 l_1 l_{c_3} m_3 \cos\beta + 2 l_1 l_2 m_3 \cos\theta_2 \\ & + 2 l_1 l_{c_2} m_2 \cos\theta_2 + 2 l_2 l_{c_3} m_3 \cos\theta_3 + I_1 + I_2 + I_3 \end{aligned}$$

$$\begin{aligned} m_{12} = {} & m_3 l_2^2 + 2 m_3 \cos\theta_3 l_2 l_{c_3} + l_1 m_3 \cos\theta_2 l_2 + m_2 l_{c_2}^2 + m_2 l_1 \cos\theta_2 l_{c_2} + m_3 l_{c_3}^2 \\ & + l_1 m_3 \cos\beta l_{c_3} + I_2 + I_3 \end{aligned}$$

$$m_{13} = l_{c_3}^2 m_3 + l_1 l_{c_3} m_3 \cos\beta + l_2 l_{c_3} m_3 \cos\theta_3 + I_3$$

$$\begin{aligned} m_{21} = {} & m_3 l_2^2 + 2 m_3 \cos\theta_3 l_2 l_{c_3} + l_1 m_3 \cos\theta_2 l_2 + m_2 l_{c_2}^2 + l_1 m_2 \cos\theta_2 l_{c_2} + m_3 l_{c_3}^2 \\ & + l_1 l_{c_3} m_3 \cos\beta + I_2 + I_3 \end{aligned}$$

$$m_{22} = m_3 l_2^2 + 2 m_3 \cos\theta_3 l_2 l_{c_3} + m_2 l_{c_2}^2 + m_3 l_{c_3}^2 + I_2 + I_3$$

$$m_{23} = m_3 l_{c_3}^2 + m_3 l_2 \cos\theta_3 l_{c_3} + I_3$$

$$m_{31} = m_3 l_{c_3}^2 + l_1 l_{c_3} m_3 \cos\beta + l_2 l_{c_3} m_3 \cos\theta_3 + I_3$$

$$m_{32} = m_3 l_{c_3}^2 + l_2 l_{c_3} m_3 \cos\theta_3 + I_3$$

$$m_{33} = m_3 l_{c_3}^2 + I_3$$

$$\begin{aligned} c_{11} = {} & -\dot{\theta}_3 \left(l_1 l_{c_3} m_3 \sin\beta + l_2 l_{c_3} m_3 \sin\theta_3 \right) - \dot{\theta}_2 \left(l_1 l_{c_3} m_3 \sin\beta + l_1 l_2 m_3 \sin\theta_2 \right. \\ & \left. + l_1 l_{c_2} m_2 \sin\theta_2 \right) \end{aligned}$$

$$\begin{aligned} c_{12} = {} & -\dot{\theta}_1 l_1 \left(l_2 m_3 \sin\theta_2 + l_{c_2} m_2 \sin\theta_2 + l_{c_3} m_3 \sin\beta \right) \\ & - \dot{\theta}_2 l_1 \left(l_2 m_3 \sin\theta_2 + l_{c_2} m_2 \sin\theta_2 + l_{c_3} m_3 \sin\beta \right) - \dot{\theta}_3 l_{c_3} m_3 (l_1 \sin\beta \\ & + l_2 \sin\theta_3) \end{aligned}$$

$$c_{13} = -l_{c_3} m_3 (l_1 \sin\beta + l_2 \sin\theta_3)(\dot{\theta}_1 + \dot{\theta}_2 + \dot{\theta}_3)$$

$$c_{21} = \dot{\theta}_1 \left(l_1 l_{c_3} m_3 \sin\beta + l_1 l_2 m_3 \sin\theta_2 + l_1 l_{c_2} m_2 \sin\theta_2 \right) - \dot{\theta}_3 l_2 l_{c_3} m_3 \sin\theta_3$$

$$c_{22} = -\dot{\theta}_3 l_2 l_{c_3} m_3 \sin\theta_3$$

$$c_{23} = -l_2 l_{c_3} m_3 \sin\theta_3 (\dot{\theta}_1 + \dot{\theta}_2 + \dot{\theta}_3)$$

$$c_{31} = \dot{\theta}_1 \left(l_1 l_{c_3} m_3 \sin\beta + l_2 l_{c_3} m_3 \sin\theta_3 \right) + \dot{\theta}_2 l_2 l_{c_3} m_3 \sin\theta_3$$

$$c_{32} = l_2 l_{c_3} m_3 \sin\dot{\beta}$$

$$c_{33} = 0$$

$$G_1 = g(l_1 m_2 \sin\theta_1 + l_1 m_3 \sin\theta_1 + l_{c_1} m_1 \sin\theta_1 + l_{c_3} m_3 \sin(\theta_1 + \theta_2 + \theta_3) + l_2 m_3 \sin\beta + l_{c_2} m_2 \sin\beta)$$

$$G_2 = g(l_{c_3} m_3 \sin(\theta_1 + \theta_2 + \theta_3) + l_2 m_3 \sin\beta + l_{c_2} m_2 \sin\beta)$$

$$G_3 = g l_{c_3} m_3 \sin(\theta_1 + \theta_2 + \theta_3)$$

with the actuation matrix B as

$$B = \begin{bmatrix} 0 \\ 1 \\ 1 \end{bmatrix} \quad \text{(A.24)}$$

Appendix B

Optimal Trajectories

The results of the optimal trajectory generation performed in Chapter 3 are presented here.

Vibration damper brachiation

The results for the vibration damper brachiation manoeuvre are shown in **Figure B.1**.

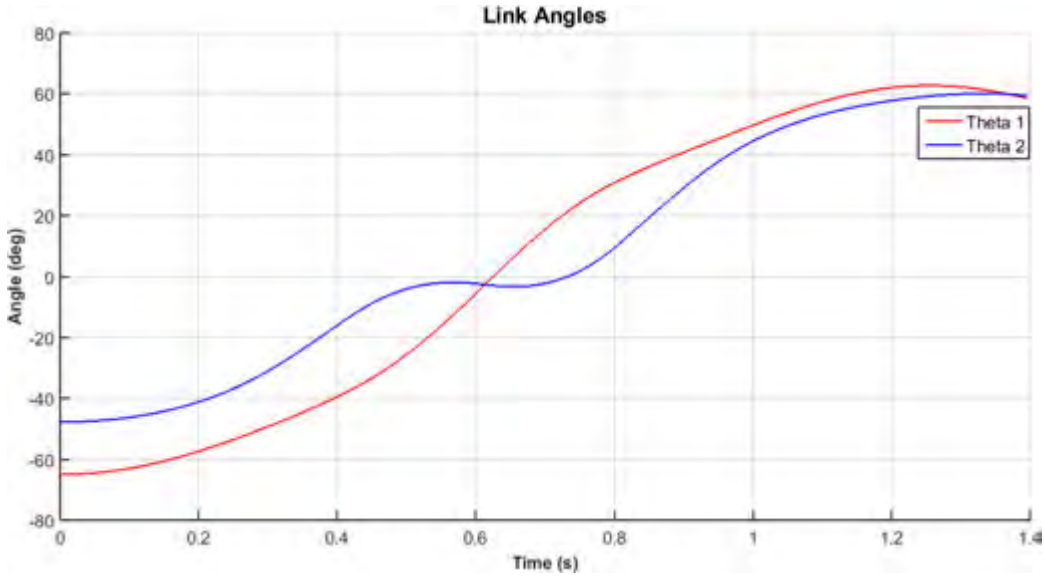

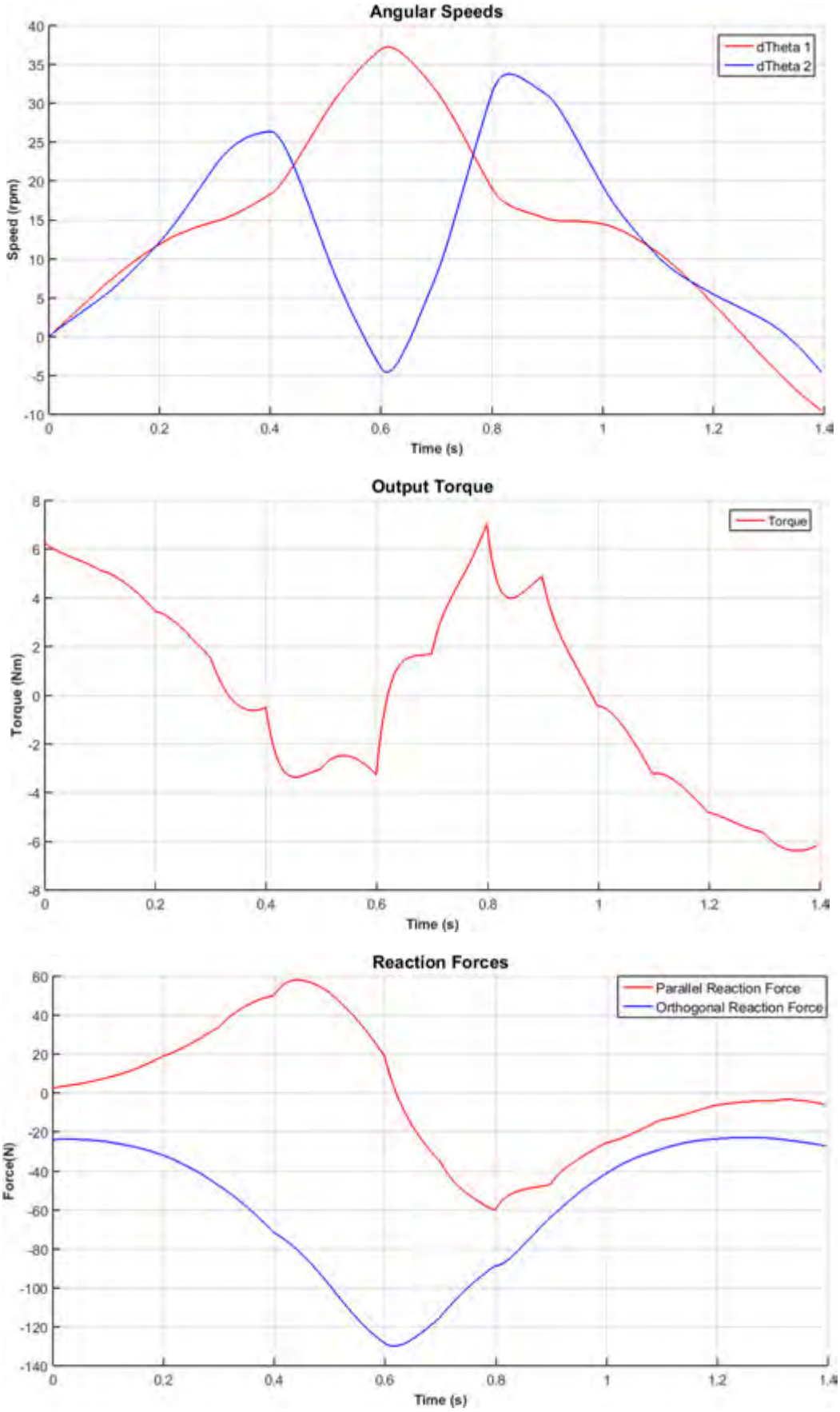

Figure B.1: Vibration damper brachiation results

Swing-up brachiation

The results for the swing-up manoeuvre are shown in **Figure B.2**.

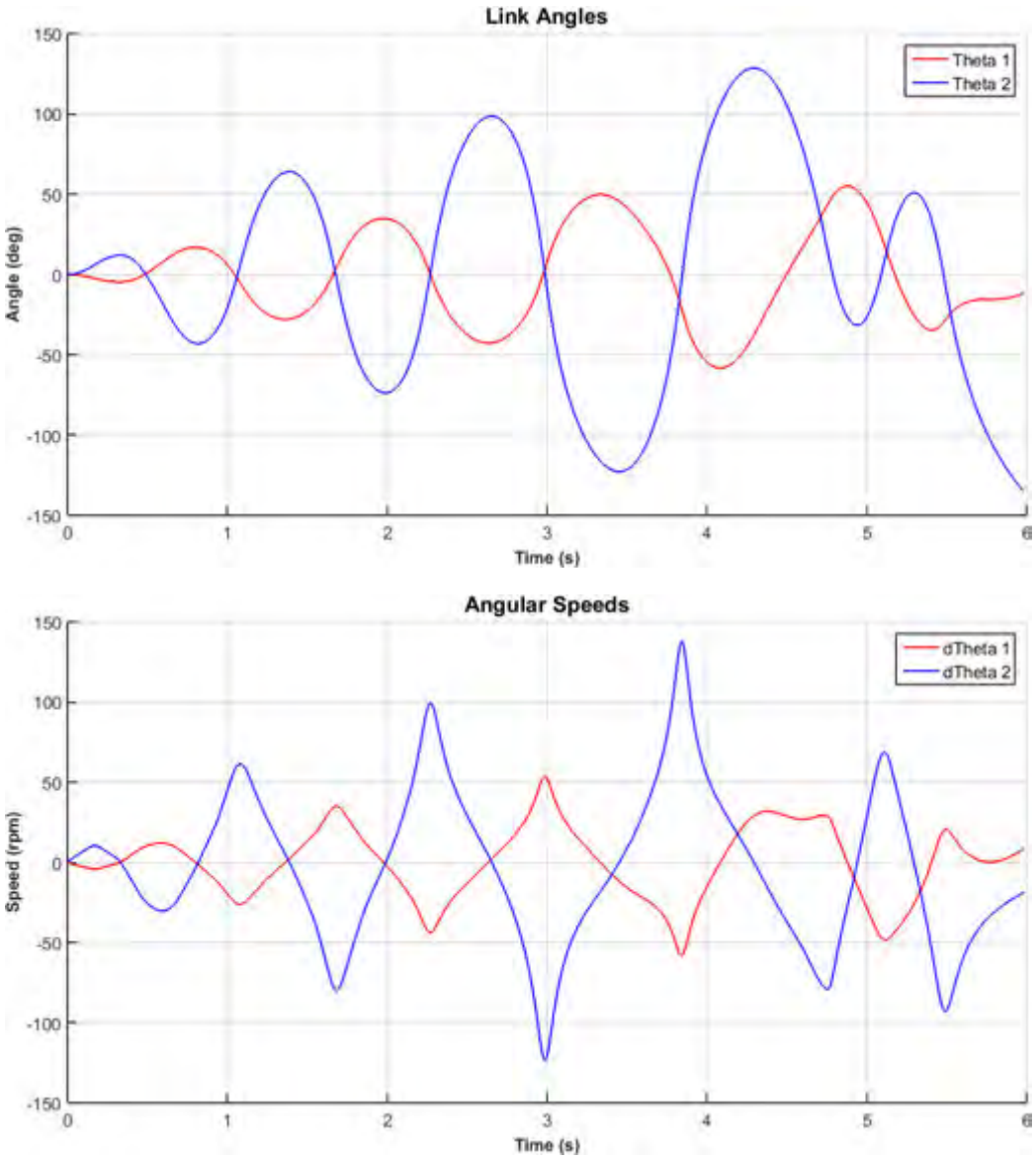

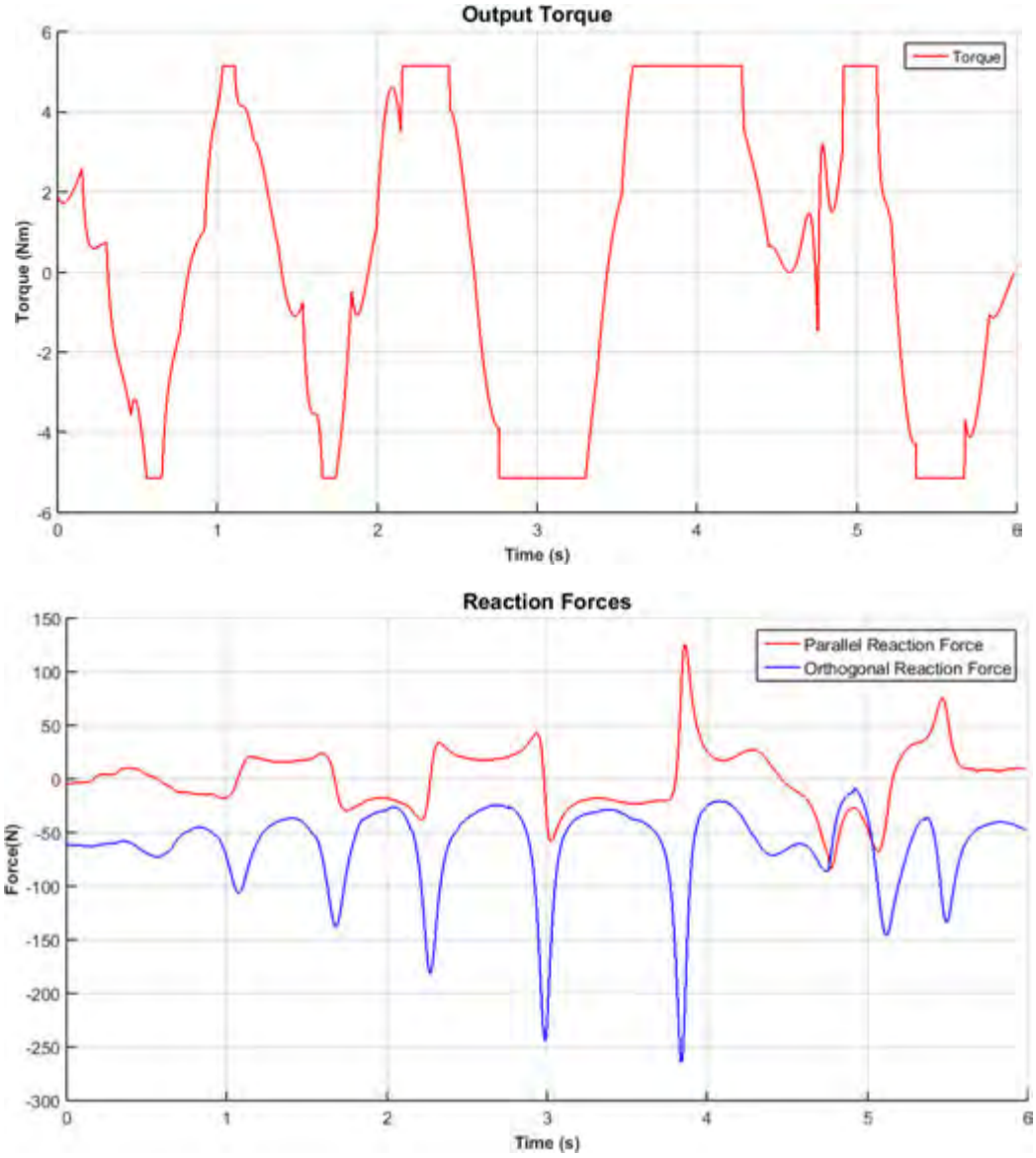

Figure B.2: Swing up brachiation results

Jumper-to-main conductor brachiation

The results for the first phase of the jumper-to-main conductor brachiation are shown in **Figure B.3**.

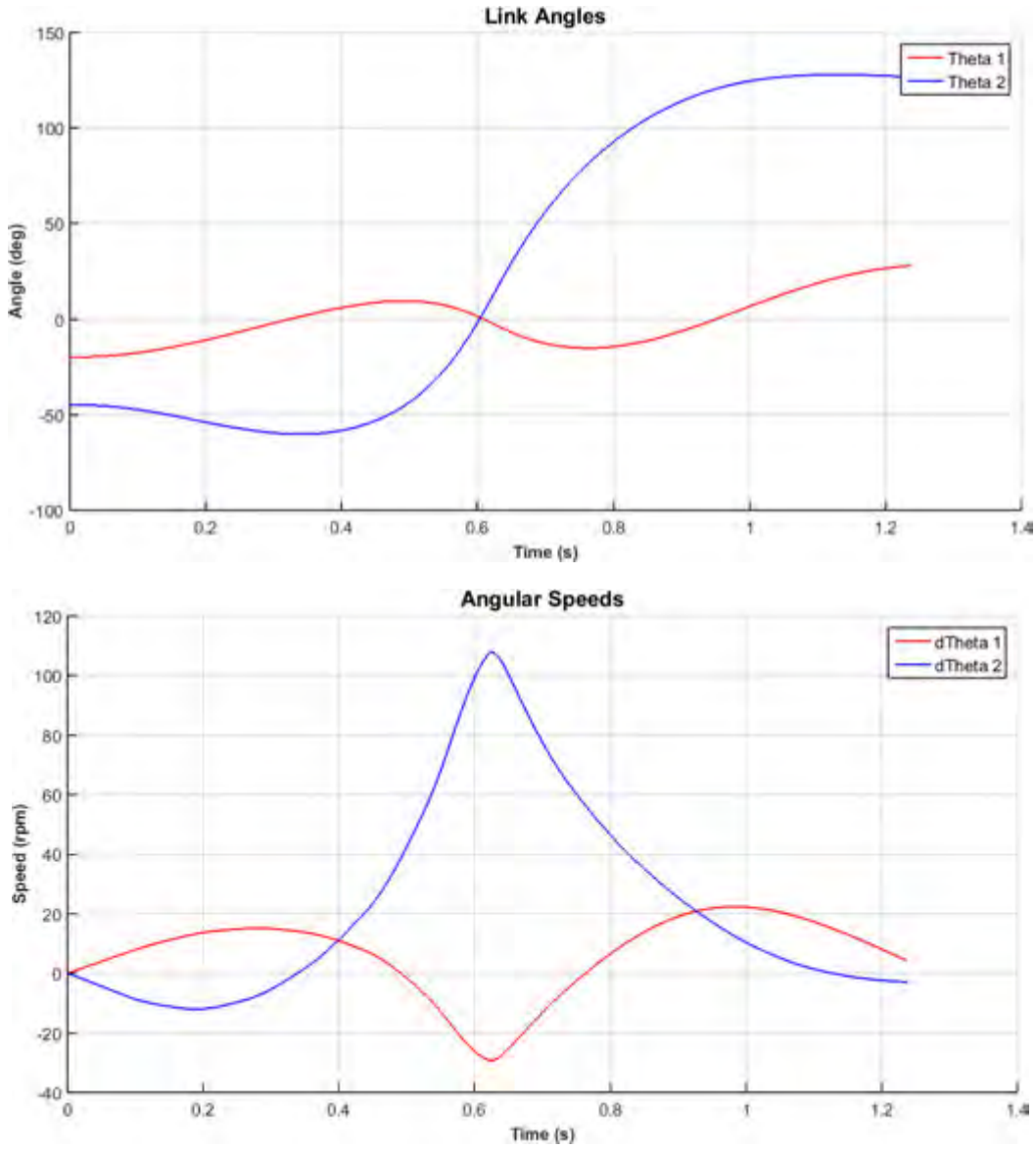

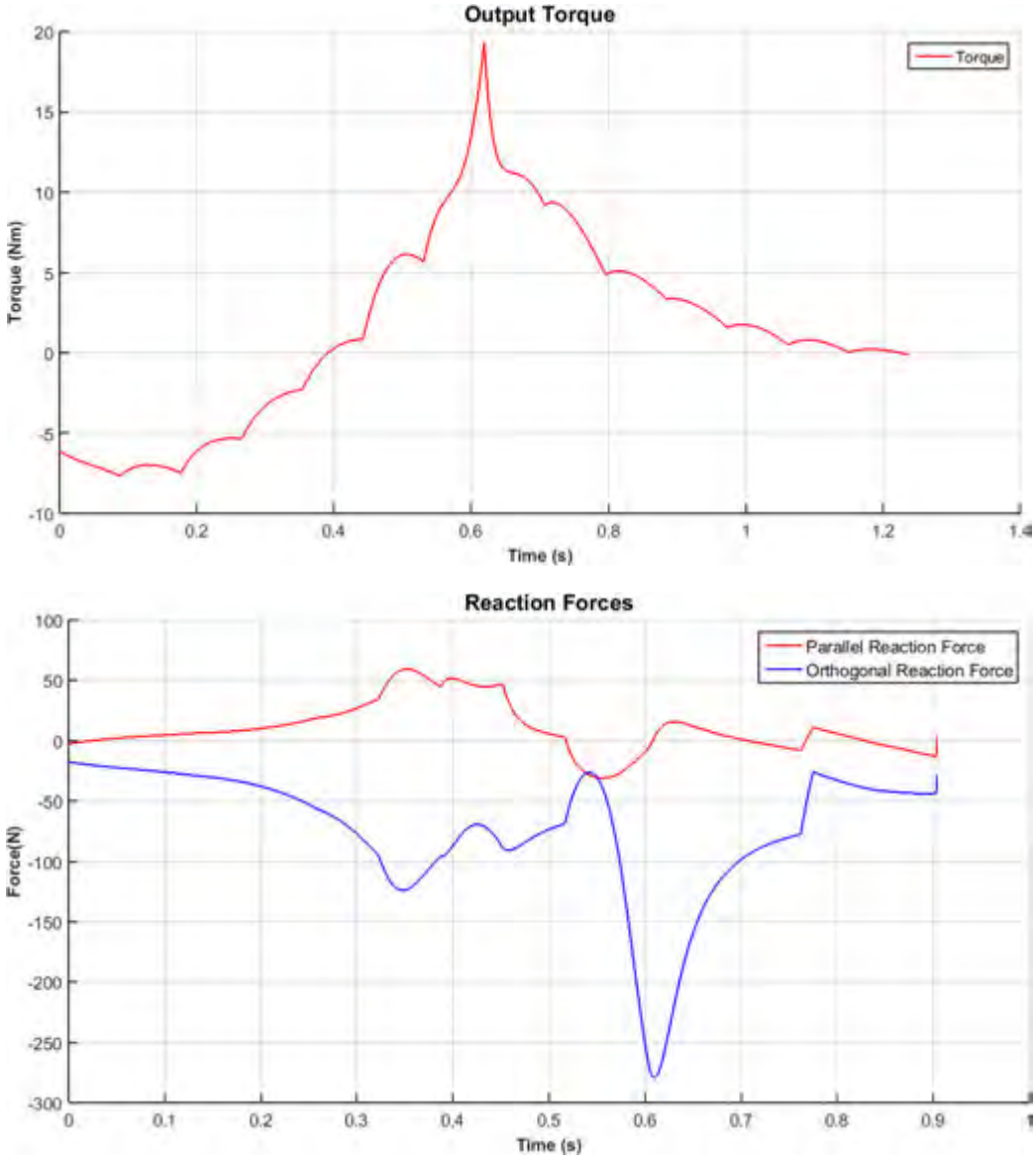

Figure B.3: Jumper-to-main conductor phase 1 brachiation results

The results for the second phase of the jumper-to-main conductor brachiation swing are shown in **Figure B.4**.

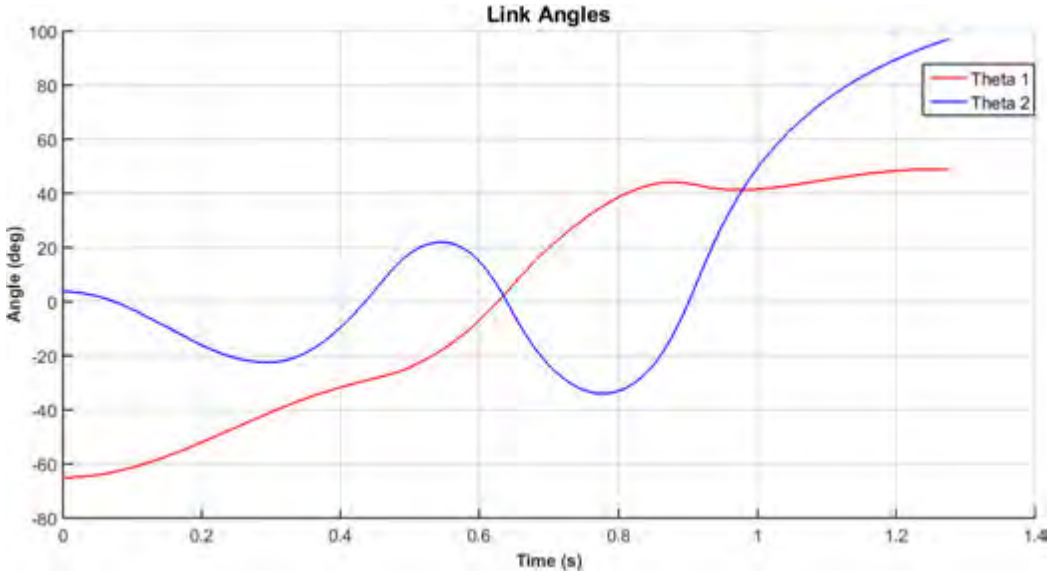
Link Angles
Theta 1
Theta 2
Angle (deg)
Time (s)

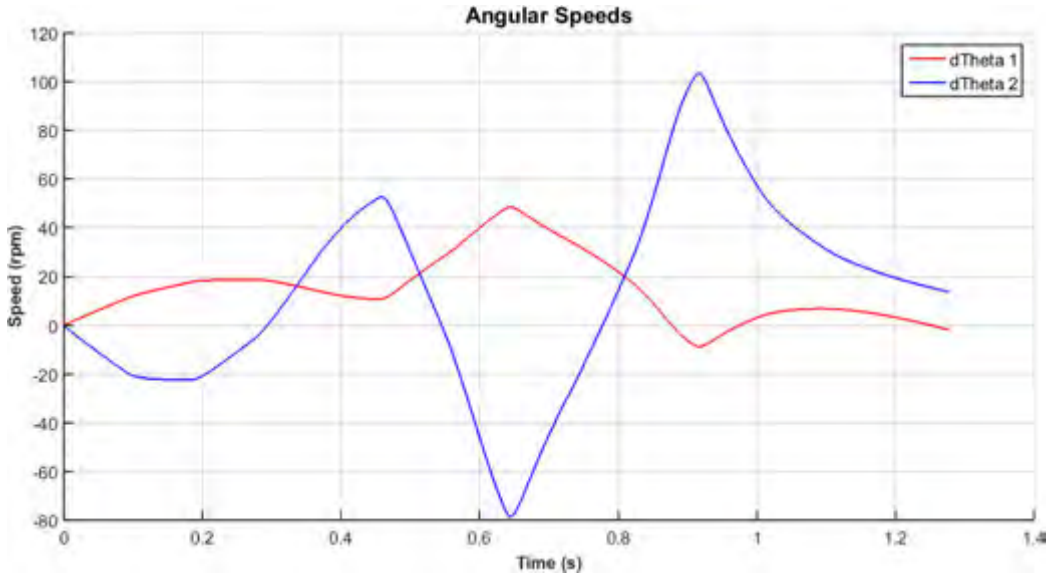
Angular Speeds
dTheta 1
dTheta 2
Speed (rpm)
Time (s)

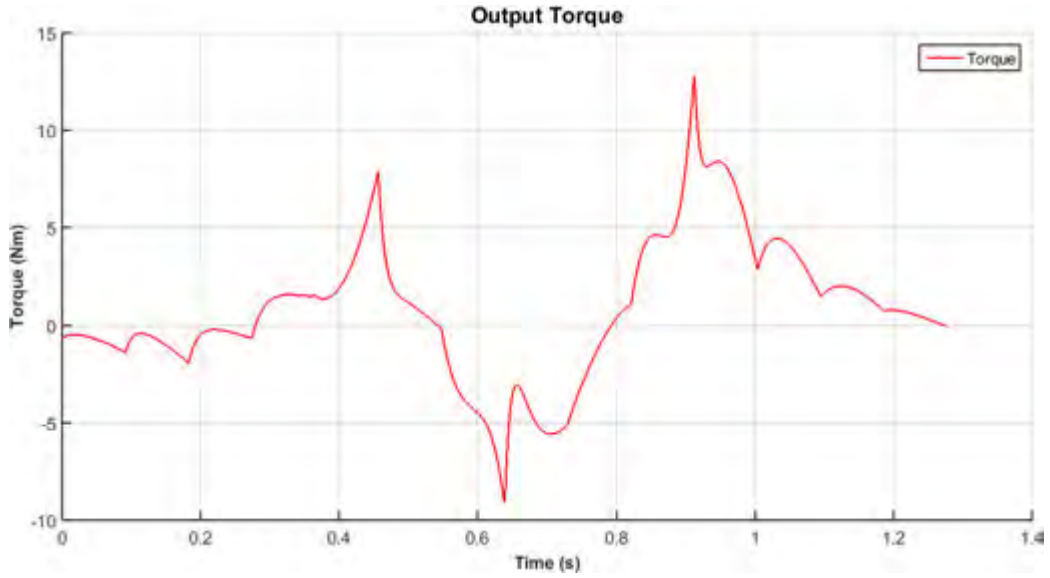
Output Torque
Torque
Torque (Nm)
Time (s)

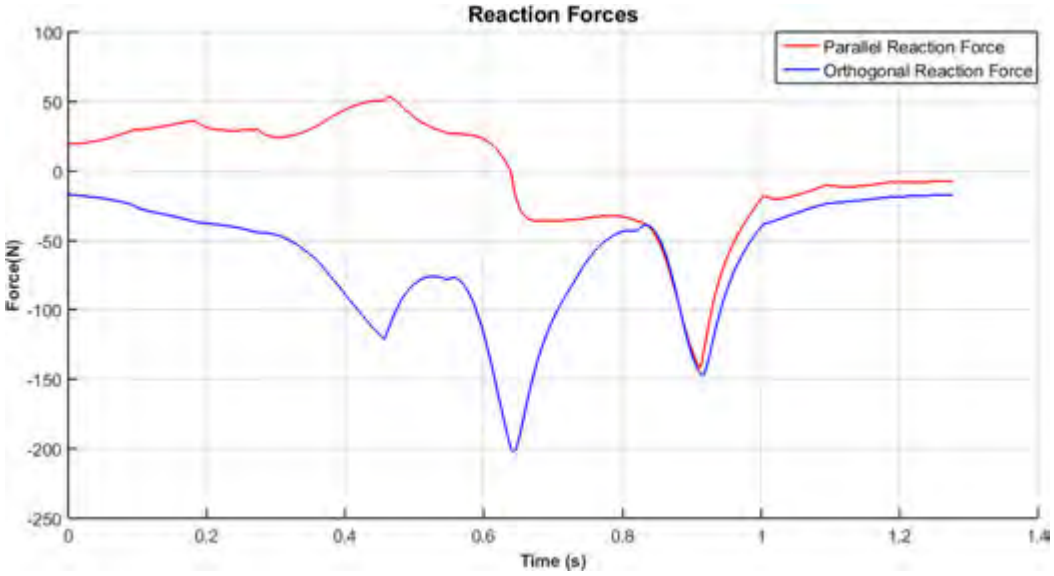

Figure B.4: Jumper-to-main conductor phase 2 brachiation results

Appendix C

Design Calculations

C.1 Gear tooth strength analysis

Analysing the gear tooth bending stress during gripper actuation allows one to determine whether the specified gear will be strong enough to withstand the bending stress.

The gear tooth bending stress was calculated using the Lewis Bending Stress equation

$$Bending\ stress, = \frac{F_t}{m_{gear} b Y} \tag{C.1}$$

where, m_{gear} is the gear module, b is the width of the gear, Y is the Lewis form factor and F_t is the tangential force, calculated as

$$F_t = \frac{2\tau}{m_{gear} N} \tag{C.2}$$

where, τ is the torque during gripper actuation and N is the number of gear teeth.

In order to avoid failure, the gear tooth bending stress must be less than the allowable bending stress. The allowable bending stress can be taken as

$$Allowable\ bending\ stress, \sigma_a = \frac{Ultimate\ tensile\ stress}{3} \tag{C.3}$$

from [73].

The specifications of the gear are summarised in **Table C.1**.

Table C.1: Gear specifications

Specification	Value	Units
Module, m_{gear}	1	-
Number of teeth, N	50	-
Face width, b	6	mm
Lewis form factor, Y [73]	0.4	-
Ultimate tensile stress, σ_a [74]	69	MPa

The gear tooth bending stress for the gripper actuation is shown in **Figure C.1**.

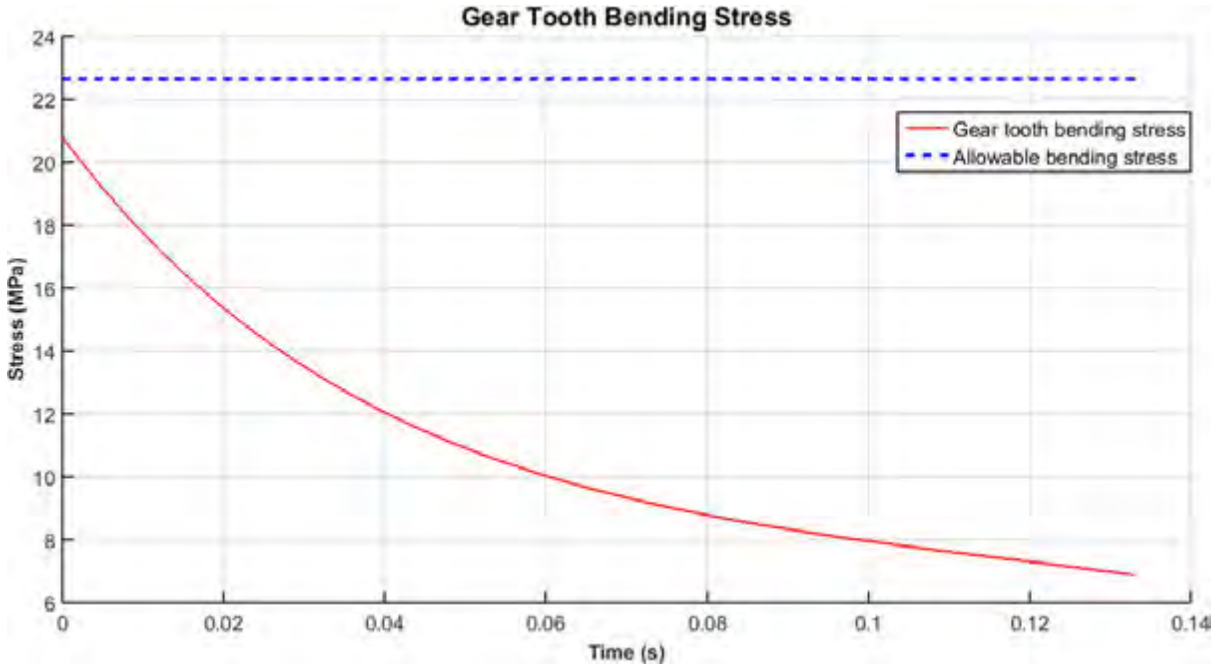

Figure C.1: Gear tooth bending stress during gripper actuation

From **Figure C.1,** it can be seen that the specified gears are strong enough to withstand the loading conditions during gripper actuation.

C.2 Drive motor requirement calculations

The speed and torque requirements for the drive motor are calculated by modelling the half-pulley as a wheel with external forces as shown below in **Figure C.2**.

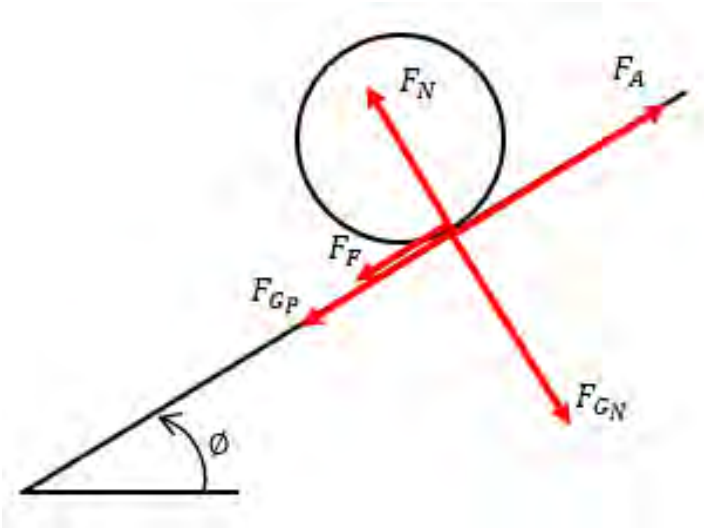

Figure C.2: Half-pulley modelling to determine required motor specifications

Where, F_{G_N} and F_{G_P} are the normal and parallel components of the gravitational force, F_N is the normal reaction force, F_F is the frictional force, F_A is the applied force and Ø is the slope angle.

The applied force, F_A can then solved as

$$F_A = F_{G_P} + F_F + F_{acc} \tag{C.4}$$

where, F_{acc} is the force required to accelerate the robot. In full, F_A is then

$$F_A = mgsin\emptyset + \mu_r mgcos\emptyset + ma_{req} \tag{C.5}$$

where, m is the mass supported by the drive wheel, μ_r is the coefficient of rolling resistance and a_{req} is the required acceleration.

It is assumed that the robot is driven in a configuration such that each pair of half-pulleys equally supports the weight of the robot.

Further, since the half-pulleys of each pair are coupled, the torque applied is a function of the weight supported by both half-pulleys.

The half-pulleys are coated with rubber using Plasti Dip spray to increase traction and prevent slipping when applying maximum torque to drive up and inclined conductor. The static coefficient of friction between rubber and metal is estimated to be 1 [75], but the coefficient of rubber is largely dependent on the fact that rubber moulds to the shape of the surface it is in contact with under increased load [36], increasing its coefficient of friction. The rubber coating applied to the pulleys is thin and therefore not capable of deforming to the extent which moulded rubber can, therefore a coefficient of 0.6 is assumed. By knowing the static coefficient of friction, the maximum tractive force can be calculated as

$$F_T = \mu_s mgcos\emptyset \tag{C.6}$$

This determines the maximum force which can be applied without causing the wheel to slip and is the limiting condition when traversing an inclined slope.

The rolling friction is difficult to estimate since there is no specific data on rolling friction coefficients between metal and rubber. However, a rolling friction coefficient of 0.01 [75] is given for a car tyre with the road, this value can be used as a worst case estimate even if it is slightly incorrect.

The specifications of the robot relating to the drive motor requirements are summarised below in **Table C.2**.

Table C.2: Robot specifications relating to drive motor requirements

Specification	Value	Units
Robot Mass	7.4	kg
Mass supported by each pulley pair	3.7	kg
Effective wheel diameter	61	mm
Coefficient of static friction	0.6	-
Coefficient of rolling friction	0.01	-

The speed and torque requirements for driving along a horizontal conductor and a $30°$ inclined conductor is shown below in **Table C.3** and **Table C.4**.

Table C.3: Drive motor requirements for a horizontal conductor

$0°$ Slope		
Specification	**Value**	**Units**
Parallel component of gravitational force, F_{G_P}	0	N
Rolling friction force, F_F	0.363	N
Desired speed	1	m/s
Time to accelerate to desired speed	2	s
F_{acc}	1.85	N
Required applied force, F_A	2.213	N
Maximum traction force, F_T	21.778	N
Required wheel torque	0.068	Nm
Required wheel speed	313.09	Rpm

Table C.4: Drive motor requirements for a $30°$ inclined conductor

$30°$ Slope		
Specification	**Value**	**Units**
Parallel component of gravitational force, F_{G_P}	15.717	N
Rolling friction force, F_F	0.314	N
Desired speed	0.5	m/s
Time to accelerate to desired speed	2	s
F_{acc}	0.925	N
Required applied force, F_A	16.95	N
Maximum traction force, F_T	18.86	N
Required wheel torque	0.575	Nm
Required wheel speed	156.55	Rpm

From the above tables, the required driving motor specifications can be summarised as shown in **Table C.5**.

Table C.5: Drive motor requirements

Scenario	**Specification**	**Value**	**Units**
$0°$ conductor	Required torque per half-pulley pair	0.07	Nm
	Required wheel speed	313.1	Rpm
$30°$ conductor	Required torque per half-pulley pair	0.52	Nm
	Required wheel speed	156.6	Rpm

C.3 Finite element analysis

The finite element analysis of the gripper's components allowed for optimisation of the component's strength-to-weight and deflection-to-weight ratio.

The dynamic reaction force during brachiation causes reaction forces at the gripper half-pulleys, as shown in **Figure C.3**. The orthogonal component of the dynamic reaction force causes reactions in the X and Z-plane, F_x and F_z respectively. While the parallel component of the dynamic reaction force causes a reaction in the Y-plane, F_y.

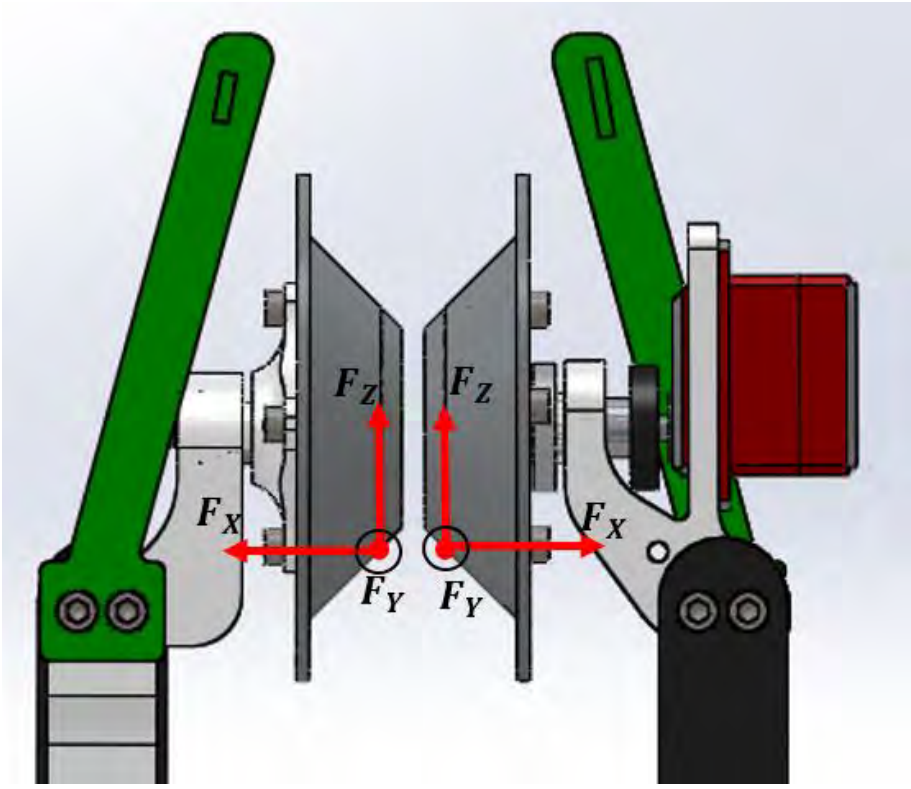

Figure C.3: FEA loading

These reactions were then propagated through the gripper assembly. Each component was analysed using a Statics approach to determine the forces acting on it. Finally, the forces were modelled in the Solidworks FEA simulation to analyse the strength and deflection of each component.

The free-body diagrams used to determine the forces acting on the components are only available in hand-written form. These can be found, along with calculations for each component, at

Design Calculations

(https://drive.google.com/open?id=0B--dECac5HrWaXE5c1VubDRqNVk)

in the "Appendix C – Design Calculations" folder.

Appendix D

Robot Videos

The videos of the robot tests can be found at

Robot Videos

(https://drive.google.com/open?id=0B--dECac5HrWaXE5c1VubDRqNVk)

in the “Appendix D – Robot Videos” folder.

Appendix E

Ethics Form

EBE Faculty: Assessment of Ethics in Research Projects (Rev2)

Any person planning to undertake research in the Faculty of Engineering and the Built Environment at the University of Cape Town is required to complete this form before collecting or analysing data. When completed it should be submitted to the supervisor (where applicable) and from there to the Head of Department. If any of the questions below have been answered YES, and the applicant is NOT a fourth year student, the Head should forward this form for approval by the Faculty EIR committee: submit to Ms Zulpha Geyer (Zulpha.Geyer@uct.ac.za; Chem Eng Building. Ph 021 650 4791).
NB: A copy of this signed form must be included with the thesis/dissertation/report when it is submitted for examination

This form must only be completed once the most recent revision EBE EIR Handbook has been read.

Name of Principal Researcher/Student: Javaad Patel Department: EBE Electrical Engineering

Preferred email address of the applicant: ptljav001@myuct.ac.za

If a Student: Degree: MSc. Electrical Engineering Supervisor: Prof. Edward Boje

If a Research Contract indicate source of funding/sponsorship:

Research Project Title: Design, Modelling and Control of a Brachiating Power Line Inspection robot

Overview of ethics issues in your research project:

Question 1: Is there a possibility that your research could cause harm to a third party (i.e. a person not involved in your project)?	YES	(NO)
Question 2: Is your research making use of human subjects as sources of data? If your answer is YES, please complete Addendum 2.	YES	(NO)
Question 3: Does your research involve the participation of or provision of services to communities? If your answer is YES, please complete Addendum 3.	YES	(NO)
Question 4: If your research is sponsored, is there any potential for conflicts of interest? If your answer is YES, please complete Addendum 4.	YES	(NO)

If you have answered YES to any of the above questions, please append a copy of your research proposal, as well as any interview schedules or questionnaires (Addendum 1) and please complete further addenda as appropriate. Ensure that you refer to the EIR Handbook to assist you in completing the documentation requirements for this form.

I hereby undertake to carry out my research in such a way that

- there is no apparent legal objection to the nature or the method of research; and
- the research will not compromise staff or students or the other responsibilities of the University;
- the stated objective will be achieved, and the findings will have a high degree of validity;
- limitations and alternative interpretations will be considered;
- the findings could be subject to peer review and publicly available; and
- I will comply with the conventions of copyright and avoid any practice that would constitute plagiarism.

Signed by:

	Full name and signature	Date
Principal Researcher/Student:	Javaad Mohamed Patel	31/03/2016

This application is approved by:

Supervisor (if applicable):	E BOJE	31/3/16
HOD (or delegated nominee): *Final authority for all assessments with NO to all questions and for all undergraduate research.*		
Chair : Faculty EIR Committee For applicants other than undergraduate students who have answered YES to any of the above questions.		

Bibliography

[1] EverSource, 2016. [Online]. Available: https://www.eversource.com/Content/images/default-source/promos---section/guy-on-powerline.jpg?sfvrsn=2. [Accessed 26 February 2016].

[2] Pgdhelicopters, “Power line inspections by helicopter - thermal Imaging, corona discharge, visual inspections by PDG Helicopters,” 2016. [Online]. Available: http://www.pdghelicopters.com/power-line-division.html. [Accessed 26 February 2016].

[3] Sandiegofreepress, 2016, [Online]. Available: http://sandiegofreepress.org/wp-content/uploads/2012/08/sdfp-power-lines.jpg. [Accessed 26 February 2016].

[4] Bbc, 2016. [Online]. Available: http://news.bbcimg.co.uk/media/images/57360000/jpg/_57360917_iceaccretionatmoneymeena.jpg. [Accessed 26 February 2016].

[5] Gridconn, 2016. [Online]. Available: http://gridconn.com.au/products/. [Accessed 26 February 2016].

[6] Pfisterer, 2016. [Online]. Available: http://www.pfisterer.com/cocs-kategorien-produkte.php?cockat=16. [Accessed 26 February 2016].

[7] Transmission-line, “Tranmission Lines Design and Electrical Engineering Hub,” 2016. [Online]. Available: http://www.transmission-line.net/2011/02/vibration-dampers-on-transmission-lines.html. [Accessed 26 February 2016].

[8] Tdworld, “TVA pushes more power down the corridor,” 2016. [Online]. Available: http://tdworld.com/transmission/tva-pushes-more-power-down-corridor. [Accessed 26 February 2016].

[9] Hubbellpowersystems, “Products for electric utilities, telecommunications and construction industries,” 2016. [Online]. Available: http://www.hubbellpowersystems.com/connectors/trans/deadends/compression-aluminum/two-die/eye-acsr.asp. [Accessed 26 February 2016].

[10] P. Ordaz, E. S.Espinoza and F. Muñoz, “Research on Swing up Control Based on Energy for the Pendubot System,” *Dynamic Systems, Measurements, and Control,* vol. 136, no. 4, 2014.

[11] T. Geissmann, “The Gibbons (Hylobtidae): An Introduction,” [Online]. Available: http://www.gibbons.de/main/introduction/chapter_english05.html. [Accessed 26 February 2016].

[12] Rraj, “A study of the Brachiation type of mobile robot,” 2016. [Online]. Available: http://rraj.rsj-web.org/en_atcl/429. [Accessed 26 February 2016].

[13] N. Morozovsky and T. Bewley, “SkySweeper: A Low DOF, Dynamic High Wire Robot,” *IEEE/RSJ International Conference on Intelligent Robots and Systems (IROS),* 2013.

[14] Phys, “News and articles on science and technology,” 2016. [Online]. Available: http://cdn.phys.org/newman/gfx/news/hires/2013/1-skysweeperro.jpg. [Accessed 26 February 2016].

[15] UC San Diego - Jacobs School of Engineering, “Pulse Winter 2013/2014,” 2016. [Online]. Available: http://jacobsschool.ucsd.edu/pulse/winter2014/images/page7_skysweeper.jpg. [Accessed 26 February 2016].

[16] University of Illinois - College of Engineering, “The Pendubot in the controls lab,” [Online]. Available: http://coecsl.ece.illinois.edu/pages/pendubot.html. [Accessed 26 February 2016].

[17] M. W. Spong, “Partial Feedback Linearization of Underactuated Mechanical Systems,” *IEEE/RSJ/GI International Conference on Intelligent Robots and Systems,* vol. 1, pp. 314-321.

[18] J. Nakanishi, T. Fukuda and D. E. Koditschek, “A Brachiating Robot Controller,” *IEEE Transactions on Robotics and Automation,* vol. 16, 2000.

[19] V. d. Oliveira and W.Lages, “MPC Applied to Motion Control of an Underactuated Brachiation Robot,” *IEEE Conference on Emerging Technology and Factory Automation,* 2006.

[20] V. d. Oliveira and W.Lages, “Real-time predictive control of a brachiation robot,” *IEEE Conference on Emerging Technologies & Factory Automation,* 2009.

[21] T. Fukuda, F. Saito and F. Arai, “A Study on the Brachiation Type of Mobile Robot,” *IEEE/RSJ International Workshop on Intelligent Robots and Systems,* 1991.

[22] N. Pouliot and S. Montambault, “Geometric design of the LineScout, a teleoperated robot for power line inspection and maintenance,” *IEEE International Conference on Robotics and Automation,* 2008.

[23] J. Toth, N. Pouliot and S. Montambault, “Field Experiences Using LineScout Technology on Large BC Tranmission Crossings,” *1st International Conference on Applied Robotics for the Power Industry,* 2010.

[24] J. Zhao, R. Guo, L. Cao and F.Zhang, “Improvement of LineROVer: A mobile robot for de-icing of transmission lines,” *1st International Conference on Applied Robotics for the Power Industry (CARPI),* 2010.

[25] Hydro-Québec, “Technological innovation | Hydro-Québec,” [Online]. Available: http://www.hydroquebec.com/innovation/en/innovations.html. [Accessed 26 February 2016].

[26] P. Debenest and M. Guarnieri, “Expliner - From Prototype Towards a Practical Robot for Inspection of High-Voltage Lines,” *1st International Conference on Applied Robotics for the Power Industry,* 2010.

[27] P. Debenest, M. Guarnieri, K. Takita, E. F. Fukushima, S. Hirose, K. Tamura, A. Kimura, H. Kubokawa, N. Iwama and F. Shiga, “Expliner – Robot for Inspection of Transmission Lines,” *IEEE International Conference on Robotics and Automation,* 2008.

[28] Hibot, “Expliner - Robot for power line inspection,” 2016. [Online]. Available: http://www.hibot.co.jp/en/products/robots_1/expliner-robot-for-power-line-inspection_12. [Accessed 26 February 2016].

[29] T. Lorimer and E. Boje, “A Simple Robot Manipulator able to Negotiate Power Line Hardware,” *2nd International Conference on Applied Robotics for the Power Industry (CARPI),* 2012.

[30] T. Rowell and E. Boje, “Obstacle Avoidance for a Power Line Inspection Robot,” *International Conference on Applied Robotics for the Power Industry (CARPI),* pp. 114-119, 2012.

[31] University of Kwa-Zulu Natal, “UKZN power line robot wows crowds at chicago expo,” [Online]. Available: http://caes.ukzn.ac.za/News/14-06-10/UKZN_power_line_robot_wows_crowds_at_Chicago_expo. [Accessed 26 February 2016].

[32] T. Hassan, “Brachiation Robot for the Inspection of Aerial Power Lines,” 2013.

[33] D. T Greenwood, Advanced Dyanmics, Cambridge: Cambridge University Press, 2003.

[34] R. M Murray, Z.Li and S. S Sastry, A Mathematical Introduction to Robotic Manipulation, CRC Press, 1994.

[35] M.Zefran and F.Bullo, Lagrangian dynamics, Robotics and Automation Handbook, 2005.

[36] B. Persson, “On the theory of rubber friction,” *Surface Science,* 1997.

[37] A. Cornelissen, “The implementation of Coulomb friction in joints in MADYMO,” 1994.

[38] Eindhoven University of technology, “ADE (G1156) Spring 2006 Handout 3: Lipschitz condition and Lipschitz continuity,” 2006. [Online]. Available: http://www.win.tue.nl/~rvhassel/Onderwijs/Old-Onderwijs/2WA23-2011/HO-03.pdf. [Accessed 26 February 2016].

[39] C. P. Tang, “Lagrangian Dynamic Formulation of a Four-Bar Mechanism with,” 2006.

[40] J. Betts, Practical Methods for Optimal Control and Estimation Using Nonlinear Programming, 2nd ed., Society for Industrial & Applied Mathematics, 2009.

[41] M. P.Kelly, “Transcription Methods for Trajectory Optimization,” 2015.

[42] T. Aoyama, K. Sekiyama, Y. Hasegawa and T. Fukuda, “Passive Dynamic Autonomous Control for the Multi-Locomotion Robot,” 2011.

[43] J. Patel and E. Boje, “Brachiating Power Line Inspection Robot,” *3rd International Conference on Applied Robotics for the Power Industry,* 2014.

[44] “Maxon motor,” [Online]. Available: http://www.maxonmotor.com/medias/sys_master/root/8797322313758/EC-4pole-30-bl-200W-HP-2WE-Detail.jpg. [Accessed 7 March 2016].

[45] “Maxon motor,” [Online]. Available: http://www.maxonmotor.com/medias/sys_master/root/8797711368222/GP-42-C-42-Detail.jpg. [Accessed 7 March 2016].

[46] S. Drives, “ESCON Module 50/5—the miniaturized OEM plug-in Module of maxon motor control's Servo Controller Series - Stork Drives,” 2013. [Online]. Available: http://storkdrives.com/2013/04/escon-module-505-the-miniaturized-oem-plug-in-module-of-maxon-motor-controls-servo-controller-series/. [Accessed 7 March 2016].

[47] School of Computer Science & Engineering. [Online]. Available: http://www.cse.unsw.edu.au/~en1811/09s2/assigns/ass2/4bardefs.png. [Accessed 8 March 2016].

[48] C. Loughnane, “FOUR BAR LINKAGE 3 POSITION SYNTHESIS (4MIN VIDEO),” [Online]. Available: http://www.pdnotebook.com/2010/11/four-bar-linkage-synthesis-3-position/. [Accessed 8 March 2016].

[49] Society of robots, “Actuators - How to modify a servo,” [Online]. Available: http://www.societyofrobots.com/actuators_modifyservo.shtml. [Accessed 11 March 2016].

[50] BotFeeder, “ABS vs PLA,” [Online]. Available: https://www.botfeeder.ca/abs-vs-pla/. [Accessed 11 March 2016].

[51] 3ders, “A few ways to strengthen 3D printed parts,” [Online]. Available: http://www.3ders.org/articles/20141010-a-few-ways-to-strengthen-3d-printed-parts.html. [Accessed 11 March 2016].

[52] 3dprintingforbeginners, “How I Learned To Stop 3D Printing Everything In One Piece,” [Online]. Available: http://3dprintingforbeginners.com/stop-3d-printing-everything-in-one-piece/. [Accessed 11 March 2016].

[53] Aussie 3D Printers. [Online]. Available: http://www.aussie3dprinters.com.au/3d-printers/2015/7/4/ultimaker-2. [Accessed 11 March 2016].

[54] G. A. Pratt and M. M. Williamson, “Series elastic actuators,” *IEEE/RSJ International Conference on Intelligent Robots and Systems. Human Robot Interaction and Cooperative Robots,* 1995.

[55] K. Kong, J. Bae and M. Tomizuka, “Control of Rotary Series Elastic Actuator for Ideal Force-Mode Actuation in Human–Robot Interaction Applications,” *IEEE/ASME TRANSACTIONS ON MECHATRONICS IEEE/ASME Transactions on Mechatronics,* vol. 14, no. 1, 2009.

[56] N. Paine, S. Oh and L. Sentis, “Design and Control Considerations for High-Performance Series Elastic Actuators,” *IEEE/ASME Transactions on Mechatronics,* vol. 19, no. 3, 2014.

[57] M. Plooij, M. v. Nunspeet, M. Wisse and H. Vallery, “Design and Evaluation of the Bi-directional Clutched Parallel Elastic Actuator (BIC-PEA),” *IEEE International Conference onRobotics and Automation (ICRA),* 2015.

[58] J. Nakanishi, T. Fukuda and D. E. Koditschek, “Experimental Implementation of a "Target Dynamics" Controller on a Two-link Brachiating,” *IEEE International Conference on Robotics and Automation,* vol. 1, pp. 787-792, 1998.

[59] A. Meghdari, S. M. H. Lavasani, M. Norouzi and M. S. R. Mousavi, “Minimum control effort trajectory planning and tracking of the CEDRA brachiation robot,” *Robotica,* vol. 31, no. 07, pp. 1119-1129, 2013.

[60] T. Lorimer, “The design and construction of a robotic platform for power line inspection,” 2011.

[61] Aalco, “Aluminium Alloy - Commercial Alloy - 6082 - T6~T651 Plate,” [Online]. Available: http://www.aalco.co.uk/datasheets/Aluminium-Alloy-6082-T6T651-Plate_148.ashx. [Accessed 11 March 2016].

[62] R.C.Juvinall and K.M.Marshek, Fundamentals of machine component design, 2012.

[63] C. Fisher, “State Estimation of a Cheetah Spine and Tail Using an Inertial Sensor Network,” 2015.

[64] Banana robotics, “IR Infrared LED 5mm (4 pack),” [Online]. Available: https://www.bananarobotics.com/shop/Infrared-LED-5mm-(4-pack). [Accessed 13 March 2016].

[65] Brico geek, “Sensor óptico QRD1114,” [Online]. Available: http://tienda.bricogeek.com/sensores/217-sensor-optico-qrd1114.html. [Accessed 13 March 2016].

[66] SparkFun, “SparkFun OpenLog - DEV-09530 - SparkFun Electronics,” [Online]. Available: https://www.sparkfun.com/products/9530. [Accessed 13 March 2016].

[67] Gravitech, “XBee PRO ZB ZigBee Mesh Module 2.4GHz 63mW with Wire Antenna,” [Online]. Available: http://www.gravitech.us/xbprozbmo250.html. [Accessed 13 March 2016].

[68] Mans, “Acer Aspire 5733 Laptop download instruction manual pdf,” [Online]. Available: http://mans.io/item/Acer/Aspire-5733. [Accessed 13 March 2016].

[69] Mantech, “28-050-50E-5W - POT S/T LIN W/W 43mm 50E 5W,” [Online]. Available: http://www.mantech.co.za/ProductInfo.aspx?Item=14M5458. [Accessed 13 March 2016].

[70] St, “STM32F4DISCOVERY Discovery kit with STM32F407VG MCU - STMicroelectronics,” [Online]. Available: http://www.st.com/web/catalog/tools/FM116/SC959/SS1532/PF252419?sc=internet/evalboard/product/252419.jsp. [Accessed 13 March 2016].

[71] R. G. Brown and P. Y. Hwang, Introduction to random signals and applied kalman filtering, 2012.

[72] A. Shkolnik and R. Tedrake, “High-dimensional underactuated motion planning via task space control,” *IEEE/RSJ International Conference on Intelligent Robots and Systems,,* 2008.

[73] Engineersedge, “Gear Tooth Strength Calculation and Equation,” [Online]. Available: http://www.engineersedge.com/gears/gear-tooth-strength.htm. [Accessed 23 March 2016].

[74] Matweb, “DuPont Performance Polymers Delrin® 900P NC010 Acetal (POM) Homopolymer,” [Online]. Available: http://www.matweb.com/search/datasheet_print.aspx?matguid=d1f38e51d0a542819a0691cc863647e3. [Accessed 23 March 2016].

[75] Tribology-abc, “Coefficient of friction, Rolling resistance, Air resistance, Aerodynamics,” [Online]. Available: http://www.tribology-abc.com/abc/cof.htm. [Accessed 10 March 2016].